ATLAS CONF Note

ATLAS-CONF-2023-065

22nd September 2023

Inclusive and differential cross section measurements of $t\bar{t}Z$ production in pp collisions at $\sqrt{s} = 13$ TeV with the ATLAS detector, including EFT and spin correlations interpretations

The ATLAS Collaboration

Measurements of both the inclusive and differential production cross sections of a top-quark-antiquark pair in association with a Z boson ($t\bar{t}Z$) are presented. Final states with two, three and four isolated leptons (electrons or muons) are targeted. The measurements use the data recorded by the ATLAS detector in pp collisions at $\sqrt{s} = 13$ TeV at the Large Hadron Collider during the years 2015-2018, corresponding to an integrated luminosity of 140 fb^{-1}. The inclusive cross section is measured to be $\sigma_{t\bar{t}Z} = 0.86 \pm 0.04$ (stat.) $\pm$ 0.04 (syst.) pb and found to be in agreement with the most advanced Standard Model predictions. The differential measurements are presented as a function of a number of observables that probe the kinematics of the $t\bar{t}Z$ system. Both absolute and normalised differential cross section measurements are performed at particle- and parton-level for specific fiducial volumes, and are compared with theoretical predictions at NLO+NNLL. The results are interpreted in the framework of the Standard Model Effective Field Theory and used to set limits on a large number of dimension-6 operators involving the top quark. The first measurement of spin correlations in $t\bar{t}Z$ is presented: the results are in agreement with the Standard Model expectations, and the null hypothesis of no spin correlations is disfavoured with a significance of 1.8 standard deviations.

ATLAS-CONF-2023-065
02 October 2023

1 Introduction

The production of top-quark-antiquark pairs ($t\bar{t}$) in association with Z bosons is, according to the Standard Model, a rare process at the LHC and a source of various multilepton final states. Given its high mass of approximately 173 GeV [1] and the therefore large Yukawa coupling to the Higgs boson, the top quark plays a special role for electroweak (EW) physics. The coupling of the top quark to the Z boson is not yet well constrained and its value can be significantly altered by beyond the Standard Model physics processes [2–7]. Precise measurements of the inclusive and differential cross sections of the associated production of the top-quark pair and the Z boson, denoted as $t\bar{t}Z$, are thus of particular interest. The $t\bar{t}Z$ process is furthermore an irreducible background to other rare top analyses, such as four-top production [8, 9], as well as several searches for BSM phenomena, for example supersymmetric models [10–13]. Also measurements of important SM processes, such as $t\bar{t}$ production in association with a Higgs boson [14–16] or single top-quark production in association with a Z boson [17, 18] are affected by the $t\bar{t}Z$ background.

The most accurate theoretical prediction of the cross section exists at full next-to-leading-order (NLO) level [19], including EW corrections. Recently they have been supplemented with the resummation of soft gluon corrections carried out at next-to-next-to-leading-logarithmic (NNLL) accuracy and matched to the existing NLO results (NLO+NNLL), as reported in Ref. [20]. The predicted value at $\sqrt{s} = 13$ TeV is:

$$\sigma_{t\bar{t}Z} = 0.863\,^{+0.073}_{-0.085}\,(\text{scale}) \pm 0.028\,(\text{PDF} \oplus \alpha_{\text{s}})\,\text{pb}.$$

Differential predictions of the $t\bar{t}Z$ cross section at NLO+NNLL accuracy were calculated in Ref. [21] and include calculations of the rapidity of the top quark, the transverse momenta p_{T} of the top (anti-top) and the Z boson, as well as the invariant masses of the $t\bar{t}$ and $t\bar{t}Z$ systems.

A first differential cross-section measurement for $t\bar{t}Z$ production at the LHC was performed by the CMS collaboration using the combined 2016 and 2017 dataset, corresponding to 77.5 fb^{-1}. The cross section was measured as a function of two variables in final states with three or four leptons [22]. Both absolute and normalised differential cross sections were presented and compared to theoretical predictions at NLO+NNLL. In addition, an inclusive cross-section measurement was performed yielding $\sigma_{t\bar{t}Z} = 0.95 \pm 0.05\,(\text{stat.}) \pm 0.06\,(\text{syst.})$ pb.

In Ref. [23], the ATLAS Collaboration provided the first measurements of the $t\bar{t}Z$ differential cross section using the full dataset from Run 2 of the LHC. The inclusive cross section was also extracted in the three- and four-lepton channels and measured to be $\sigma_{t\bar{t}Z} = 0.99 \pm 0.05\,(\text{stat.}) \pm 0.08\,(\text{syst.})$ pb. The results from both the ATLAS and CMS Collaborations are compatible with the upper end of the Standard Model prediction [20], and with each other.

This paper presents an extended and refined measurement of the $t\bar{t}Z$ cross section in the multilepton final states using the full dataset collected by the ATLAS experiment during Run 2 with the LHC. An additional final state is considered, targeting the all-hadronic decay of the $t\bar{t}$ system. The precision of the cross section is enhanced by making use of improved calibrations of physics objects and total integrated luminosity, together with reduced experimental uncertainties, while the description of theoretical and modelling uncertainties benefits from recent measurements of key background processes and more accurate Monte Carlo event generators and fixed-order phenomenological calculations. The production cross section of the $t\bar{t}Z$ process is extracted by performing a profile-likelihood fit simultaneously in the targeted analysis regions with the signal normalisation as the parameter of interest. A similar profile-likelihood approach is employed to unfold the data to particle- and parton-level, measuring absolute and normalised differential cross

sections. The improved treatment of background effects, more detailed models of systematic uncertainties and unfolding several detector-level selections simultaneously to the same fiducial volume allow for a more precise and robust result than the one presented in Ref. [23]. The extracted inclusive $t\bar{t}Z$ cross section and selected normalised differential kinematic distributions at particle- and parton-level are then used to constrain the dimension-6 Effective Field Theory (EFT) operators relevant to the t-Z interaction in the context of the SM Effective Field Theory (SMEFT) [24, 25]. A further interpretation of the experimental results is given in terms of coefficients of the spin density matrix, never before measured for the $t\bar{t}Z$ process [26].

2 ATLAS detector

The ATLAS detector [27] at the LHC covers nearly the entire solid angle around the collision point.[1] It consists of an inner tracking detector surrounded by a thin superconducting solenoid, electromagnetic and hadron calorimeters, and a muon spectrometer incorporating three large superconducting air-core toroidal magnets.

The inner-detector system (ID) is immersed in a 2 T axial magnetic field and provides charged-particle tracking in the range $|\eta| < 2.5$. The high-granularity silicon pixel detector covers the vertex region and typically provides four measurements per track, the first hit normally being in the insertable B-layer (IBL) installed before Run 2 [28, 29]. It is followed by the silicon microstrip tracker (SCT), which usually provides eight measurements per track. These silicon detectors are complemented by the transition radiation tracker (TRT), which enables radially extended track reconstruction up to $|\eta| = 2.0$. The TRT also provides electron identification information based on the fraction of hits (typically 30 in total) above a higher energy-deposit threshold corresponding to transition radiation.

The calorimeter system covers the pseudorapidity range $|\eta| < 4.9$. Within the region $|\eta| < 3.2$, electromagnetic calorimetry is provided by barrel and endcap high-granularity lead/liquid-argon (LAr) calorimeters, with an additional thin LAr presampler covering $|\eta| < 1.8$ to correct for energy loss in material upstream of the calorimeters. Hadron calorimetry is provided by the steel/scintillator-tile calorimeter, segmented into three barrel structures within $|\eta| < 1.7$, and two copper/LAr hadron endcap calorimeters. The solid angle coverage is completed with forward copper/LAr and tungsten/LAr calorimeter modules optimised for electromagnetic and hadronic energy measurements respectively.

The muon spectrometer (MS) comprises separate trigger and high-precision tracking chambers measuring the deflection of muons in a magnetic field generated by the superconducting air-core toroidal magnets. The field integral of the toroids ranges between 2.0 and 6.0 Tm across most of the detector. Three layers of precision chambers, each consisting of layers of monitored drift tubes (MDT), cover the region $|\eta| < 2.7$, complemented by cathode-strip chambers (CSC) in the forward region, where the background is highest. The muon trigger system covers the range $|\eta| < 2.4$ with resistive-plate chambers (RPC) in the barrel, and thin-gap chambers (TGC) in the endcap regions.

[1] ATLAS uses a right-handed coordinate system with its origin at the nominal interaction point (IP) in the centre of the detector and the z-axis along the beam pipe. The x-axis points from the IP to the centre of the LHC ring, and the y-axis points upwards. Cylindrical coordinates (r, ϕ) are used in the transverse plane, ϕ being the azimuthal angle around the z-axis. The pseudorapidity is defined in terms of the polar angle θ as $\eta = -\ln\tan(\theta/2)$. Angular distance is measured in units of $\Delta R \equiv \sqrt{(\Delta\eta)^2 + (\Delta\phi)^2}$.

Interesting events are selected by the first-level trigger system implemented in custom hardware, followed by selections made by algorithms implemented in software in the high-level trigger [30]. The first-level trigger accepts events from the 40 MHz bunch crossings at a rate below 100 kHz, which the high-level trigger further reduces in order to record events to disk at about 1 kHz.

An extensive software suite [31] is used in data simulation, in the reconstruction and analysis of real and simulated data, in detector operations, and in the trigger and data acquisition systems of the experiment.

3 Data and simulated event samples

For this analysis the full Run 2 dataset collected in pp collisions during the years 2015-2018 and corresponding to an integrated luminosity of 140 fb^{-1} [32] is used. Only events recorded when LHC beams were stable and all ATLAS detectors were operational are selected. The uncertainty on the combined 2015-2018 integrated luminosity is 0.83% [32], obtained using the LUCID-2 detector [33] for the primary luminosity measurements, complemented by measurements using the inner detector and calorimeters. The average number of interactions per bunch crossing ranges from 0.5 to around 80 and has mean of 33.7.

The data were collected using a combination of single-electron and single-muon triggers, with requirements on the identification, isolation, and p_{T} of the leptons to maintain high efficiency across the full momentum range while controlling the trigger rates [30, 34, 35]. For electrons the trigger thresholds were p_{T} = 26, 60 and 140 GeV, whereas for muons, the thresholds were p_{T} = 26 and 50 GeV[2]. Isolation requirements were applied to the triggers with the lower p_{T} thresholds [36–38] (26 GeV for electrons and muons).

Simulated Monte Carlo (MC) samples are used to model the signal and the prompt SM background. The effect of multiple interactions in the same and neighbouring bunch crossings (pile-up) was modelled by overlaying the simulated hard-scattering event with inelastic proton–proton (pp) events generated with Pythia 8.186 [39] using the NNPDF2.3lo set of parton distribution functions (PDF) [40] and the A3 set of tuned parameters [41]. Separate MC production campaigns are used to model the different pile-up distributions observed in data for the years 2015/16, 2017 and 2018. The simulated samples are reweighted to reproduce the observed distribution of the average number of collisions per bunch crossing in each data-taking period.

The simulation of detector effects is performed with either a full ATLAS detector simulation [42] based on the Geant4 [43] framework or a fast simulation (AtlFast II) using a parameterisation of the performance of the electromagnetic and hadronic calorimeters and Geant4 for the other detector components [44]. The majority of processes use the full simulation, while the latter setup is used only for rare background processes and alternative modelling samples for various processes.

The associated production of a top-quark-antiquark pair with a leptonically decaying Z boson is modelled using the MadGraph5_aMC@NLO 2.8.1 [45] generator which provides matrix elements at NLO in the strong coupling constant α_{s} with the `NNPDF3.0NLO` [46] parton distribution function (PDF) set. The $\gamma^* \to \ell^+\ell^-$ contribution and the Z/γ^* interference are taken into account, down to 5 GeV in the invariant dilepton mass. The functional form of the renormalisation and factorisation scales (μ_{r}, μ_{f}) is set to the default scale $0.5 \times \sum_i \sqrt{m_i^2 + p_{T,i}^2}$, where the sum runs over all the particles generated from the matrix element calculation. Top quarks are decayed at leading order (LO) using MadSpin [47, 48] to preserve all spin correlations. The top-quark mass is set to 172.5 GeV in all MC samples. The events are interfaced with

[2] Lower p_{T} thresholds of 24 GeV and 120 GeV for electrons and 20 GeV for muons were applied for 2015 data.

PYTHIA 8.244 [49] for the simulation of the parton shower, fragmentation, hadronisation, and underlying event, using the A14 set of tuned parameters [50] and the NNPDF2.3LO PDF set. The decays of bottom and charm hadrons are simulated using the EVTGEN 1.7.0 program [51].

To evaluate theoretical uncertainties of the signal prediction, several alternative $t\bar{t}Z$ MC samples are considered. These include a sample generated with the same MADGRAPH5_AMC@NLO version as the nominal sample, but interfaced to HERWIG 7.2.1 [52, 53] for the simulation of the parton shower (using the default angular-ordered shower model). Two additional samples with the same settings as the nominal $t\bar{t}Z$ sample, but with an up and down variation of the Var3c parameter in the A14 tune, are used to evaluate uncertainties associated to the modelling of the initial-state radiation (ISR), following a similar approach as the one described in Ref. [54]. The Var3c A14 tune variation corresponds to the variation of α_s for ISR in the A14 tune.

Alternative samples generated with SHERPA are compared to the unfolded differential distributions. A $t\bar{t} + \ell\ell$ sample is produced with the SHERPA 2.2.1 [55] generator at NLO accuracy, and referred to as the "inclusive" setup. Another sample uses a newer version of the same generator, SHERPA 2.2.11, together with the MEPS@NLO matching algorithm [56–58], and performs the multi-leg merging of up to three additional partons at LO, with a merging scale of 30 GeV. In both cases, a dynamic renormalisation scale defined similarly to that of the nominal $t\bar{t}Z$ samples is used. These samples also include off-shell effects down to 5 GeV in the invariant mass of the lepton pair. The default SHERPA parton shower is used along with the NNPDF3.0NNLO PDF set.

Events featuring the production of a $t\bar{t}$ pair in association with a SM Higgs boson with a mass of 125 GeV ($t\bar{t}H$) are generated using NLO matrix elements in MADGRAPH5_AMC@NLO 2.6.0 with the NNPDF3.0NLO PDF set. The samples are showered with PYTHIA 8.230 using the A14 tune.

For top-quark-antiquark pair production with a W boson ($t\bar{t}W$), the SHERPA 2.2.10 generator and default parton shower are used at NLO accuracy in QCD, with multi-leg merging of up to one additional parton at NLO and up to two additional partons at LO (MEPS@NLO setup with a merging scale of 30 GeV). Additionally, a LO QCD sample also generated with SHERPA 2.2.10 but for the $t\bar{t}Wj$ final state is used to model additional electroweak corrections to $t\bar{t}W$ production. In both $t\bar{t}W$ samples, the NNPDF3.0NNLO PDF set is used.

The production of single top quarks in association with a Z boson (tZq) is modelled using the MADGRAPH5_AMC@NLO 2.9.5 generator at NLO, and that of single top quarks in association with a W and a Z boson (tWZ) using MADGRAPH5_AMC@NLO 2.2.2 at NLO, both with the NNPDF3.0NLO PDF set. The tZq events are interfaced with PYTHIA 8.245 and the tWZ events with PYTHIA 8.212, using the A14 tune and the NNPDF2.3LO PDF set. The tZq sample is simulated in the four-flavour scheme (therefore including an additional b-quark in the final state) and normalised to a cross section obtained in the five-flavour scheme. It additionally includes off-shell effects down to 5 GeV in the invariant mass of the lepton pair.

Modelling uncertainties on the tZq process are obtained similarly as in the case of $t\bar{t}Z$: the Var3c parameter of the A14 tune is varied up and down, and a separate sample is considered for the variation of the choice of parton shower, by interfacing events generated in MADGRAPH5_AMC@NLO 2.9.5 to the HERWIG 7.2.1 parton shower. At NLO in QCD, the Feynman diagrams of the tWZ process include contributions such as $gg \to tWZb$, which may also feature a second intermediate top resonance and thus interfere with the signal $t\bar{t}Z$ process. The nominal tWZ sample follows the "diagram removal 1" (DR1) scheme described in Ref. [59] and ignores any Feynman diagrams containing two resonant top quarks. An alternative sample is generated within the DR2 scheme, which additionally considers the interference terms (at the level of

squared amplitudes) between single- and double-resonant top quark pair production. This alternative sample is used to set a modelling uncertainty on the tWZ process, as described in Section 7.3.

The background production of $t\bar{t}$ events is modelled using the POWHEG BOX 2 generator [60] at NLO with the NNPDF3.0NLO PDF set and the damping factor h_{damp}[3] set to 1.5 times the top mass. The events are interfaced with PYTHIA 8.230 using the A14 tune and the NNPDF2.3LO PDF set. The top quark decays are further modelled at LO, while decays of bottom and charm hadrons are simulated using the EVTGEN 1.2.0 program.

Several alternative samples are used to evaluate theoretical uncertainties of the $t\bar{t}$ events. These include a separate sample using the generator version as above where the h_{damp} parameter is varied to 3.0 times the top mass, a sample varying the choice of parton shower interfacing HERWIG 7.0.4 to the events generated in POWHEG, and a sample with a different matrix element generator using MADGRAPH5_AMC@NLO 2.3.3 interfaced with PYTHIA 8.230.

Diboson processes featuring the production of three charged leptons and one neutrino or four charged leptons (denoted as WZ+jets or ZZ+jets, respectively) are simulated using the SHERPA 2.2.2 generator. In this setup, multiple matrix elements are matched and merged with the SHERPA parton shower based on the Catani-Seymour dipole factorisation scheme [61, 62] using the MEPS@NLO prescription [56–58, 63]. The virtual QCD correction for matrix elements at NLO accuracy are provided by the OPENLOOPS library [64, 65]. Samples are generated using the NNPDF3.0NNLO PDF set, along with the dedicated set of tuned parton shower parameters developed by the SHERPA authors. WZ/ZZ+jets events with no or one additional parton are simulated at NLO whereas events with two or three partons are simulated at LO precision.

The production of W and Z bosons with multiple jets (V+jets) is simulated with the SHERPA 2.2.1 generator using NLO-accurate matrix elements for up to two jets, and LO-accurate ones for up to four jets, calculated with the Comix [61] and OPENLOOPS [64–66] libraries. They are matched with the SHERPA parton shower using the MEPS@NLO prescription. The NNPDF3.0NNLO set of PDFs is used and the samples are normalised to next-to-next-to-leading order (NNLO) predictions [67].

Events from both diboson and V+jets processes are separated into light-, b- and c-flavour components, depending on whether a b- or c-hadron is found in the MC event record of any of the selected jets.

MC samples featuring Higgs production in association with a W or Z boson are generated with PYTHIA 8.186 using the A14 tune and the NNPDF2.3LO PDF set. Triple top-quark production ($tt\bar{t}$) and the production of a $t\bar{t}$ pair with two W bosons ($t\bar{t}WW$) are simulated at LO using MADGRAPH 2.2.2 interfaced to PYTHIA 8.186 with the A14 tune and the NNPDF2.3LO PDF set. Four top-quark production ($t\bar{t}t\bar{t}$) is simulated at NLO using the MADGRAPH5_AMC@NLO 2.3.3 generator interfaced to PYTHIA 8.230 with the A14 tune and the NNPDF3.1NLO PDF set; an alternative sample uses the HERWIG 7.04 parton shower instead. Processes with three heavy gauge bosons (WWW, WWZ, WZZ and ZZZ) with up to six leptons in the final states are simulated with SHERPA 2.2.2 and the NNPDF3.0NLO PDF set. Final states with no additional partons are calculated at NLO, whereas final states with one, two and three additional partons are calculated at LO.

The versions of the generator, parton shower and PDF used for each of the nominal MC samples as well as the reference cross section used to normalise the samples are given in Table 1.

For the SMEFT interpretation, additional MC samples are produced at LO in QCD for the $t\bar{t}Z$ and tZq processes, using the MADGRAPH 2.9.3 generator and PYTHIA 8.245 parton shower (with the default

[3] The h_{damp} parameter is a resummation damping factor and one of the parameters that controls the matching of POWHEG matrix elements to the parton shower and thus effectively regulates the high-p_{T} radiation against which the $t\bar{t}$ system recoils.

Table 1: Versions of the generator, parton shower and PDF used for the nominal MC samples and reference cross sections used in the analysis. Whenever a reference is not indicated, the cross section is taken directly from the MC setup described in the text.

Process	Generator	Parton Shower	PDF	Reference Cross Section (fb)
$t\bar{t}Z$	MadGraph5_aMC@NLO 2.8.1	Pythia 8.244	NNPDF3.0NLO	876.4 [19, 54]
$t\bar{t}H$	MadGraph5_aMC@NLO 2.6.0	Pythia 8.230	NNPDF3.0NLO	507.4 [19]
$t\bar{t}W/t\bar{t}Wj$	Sherpa 2.2.10	Sherpa 2.2.10	NNPDF3.0NNLO	722.4 [68]
tZq	MadGraph5_aMC@NLO 2.9.5	Pythia 8.245	NNPDF3.0NLO	38.72
tWZ	MadGraph5_aMC@NLO 2.2.2	Pythia 8.212	NNPDF2.3LO	16.08
$t\bar{t}$	Powheg Box 2	Pythia 8.230	NNPDF3.0NLO	87,710 [69]
WZ+jet/ZZ+jets	Sherpa 2.2.2	Sherpa 2.2.2	NNPDF3.0NNLO	7,334
V+jets	Sherpa 2.2.1	Sherpa 2.2.1	NNPDF3.0NNLO	6,255×10^3 [67]
$t\bar{t}t\bar{t}$	MadGraph5_aMC@NLO 2.3.3	Pythia 8.230	NNPDF3.1NLO	11.97 [70]
$tt\bar{t}$	MadGraph 2.2.2	Pythia 8.186	NNPDF2.3LO	1.64
VH	Pythia 8.186	Pythia 8.186	NNPDF2.3LO	2,250 [71–77]
VVV	Sherpa 2.2.2	Sherpa 2.2.2	NNPDF3.0NLO	13.74

A14 tune settings). They rely on the SMEFTsim 3.0 [25] UFO model [78] implemented in MadGraph with FeynRules [79], in the M_W electroweak input scheme [80] with the top flavour restrictions (in the five-flavour scheme). The nominal events are generated according to the SM, and the MadGraph reweighting module is used to compute a large number of alternative event weights corresponding to the inclusion of dimension-6 EFT vertices and propagators in the production Feynman diagrams. These internal weights can then be used to extract the dependence of various observables (including the cross section) on more than 30 different EFT operators related to $t\bar{t}$ production, the t-Z vertex and the off-shell $t\bar{t}\ell\ell$ vertex, as described in Section 11. Since the running of the EFT couplings is not possible in MadGraph, the renormalisation and factorisation scales are kept fixed at $\mu = \sum_i m_i$ (where i runs over the massive final state resonances). The EFT samples are further simulated (with AtlFast II) and reconstructed in order to assess their impact on the unfolding (efficiency and acceptance corrections).

4 Object identification and event reconstruction

Electron candidates are reconstructed from clusters of energy deposits in the electromagnetic calorimeter that are matched to a track in the ID. They are required to satisfy $p_{\mathrm{T}} > 7$ GeV, $|\eta| < 2.47$ and a Medium likelihood-based identification requirement [81, 82]. Electron candidates are excluded if their calorimeter clusters lie within the transition region between the barrel and the endcap of the electromagnetic calorimeter, $1.37 < |\eta| < 1.52$, to reduce the contribution from fake electrons. The track associated with the electron must pass the requirements $|z_0 \sin(\theta)| < 0.5$ mm and $|d_0|/\sigma(d_0) < 5$, where z_0 describes the longitudinal impact parameter relative to the reconstructed primary vertex,[4] d_0 is the transverse impact parameter relative to the beam axis, and $\sigma(d_0)$ is the uncertainty on d_0. Furthermore, a requirement on the electron

[4] The primary vertex is defined as the vertex with the highest scalar sum of the squared transverse momenta of associated tracks with $p_{\mathrm{T}} > 500$ MeV, with at least two such tracks.

isolation, corresponding to the PLVLoose isolation working point (WP) [14] is applied to signal electrons; baseline electrons have no isolation requirement.

Muon candidates are reconstructed from MS tracks matched to ID tracks in the pseudorapidity range of $|\eta| < 2.5$. They must satisfy $p_{\mathrm{T}} > 7\,\mathrm{GeV}$ along with the Medium identification requirements defined in Ref. [83, 84]. This criterion defines requirements on the number of hits in the different ID and MS subsystems and on the significance of the charge-to-momentum ratio q/p. In addition, the track associated with the muon candidate must have $|z_0 \sin(\theta)| < 0.5\,\mathrm{mm}$ and $|d_0|/\sigma(d_0) < 3$. As is the case for electrons, the baseline muons have no isolation requirements, whereas the muons selected for the analysis need to pass the PLVLoose isolation WP. The lepton trigger, reconstruction and selection efficiencies from simulation receive small corrections derived from measurements of $Z \to \ell\ell$ events in the data [34, 35, 82, 84].

Jets are reconstructed using the anti-k_t jet algorithm [85] as implemented in the FastJet package [86] with the distance parameter R set to 0.4 and topological clusters [87] as input. The jets are calibrated through the application of a jet energy scale derived from 13 TeV data and simulation [88]. The jets are kept only if they have $p_{\mathrm{T}} > 25$ GeV and are inside a pseudorapidity range of $|\eta| < 2.5$. The JetVertexTagger (JVT) [89] algorithm is employed in order to mitigate pile-up effects, applying the Tight WP.

The identification of b-jets is done with the DL1r b-tagging algorithm [90, 91]. A WP corresponding to an 85% efficiency is used for most pre-selections in the analysis. Exclusive bins in the b-tagging discriminant corresponding to different b-jet identification efficiencies are also used, as pseudo-continuous b-tagging (PCBT). This allows for the possible use of different calibrated b-tagging WPs in defining selections targeting specific signal or background processes, referred to as regions.

The missing transverse momentum is defined as the negative vector sum of the transverse momenta of all selected and calibrated physics objects. Low-momentum tracks from the primary vertex that are not associated with any of the reconstructed physics objects described previously are also included as a 'soft term' in the calculation [92]. The magnitude of the missing transverse momentum vector is denoted as $E_{\mathrm{T}}^{\mathrm{miss}}$.

Ambiguities can arise from the independent reconstruction of electron, muon and jet candidates in the detector. A sequential procedure (overlap removal) is applied to resolve these ambiguities and, thus, avoids a double counting of physics objects.[5] It is applied as follows. If an electron candidate and a muon candidate share a track, the electron candidate is removed. The closest jet candidate within a distance of $\Delta R_{y,\phi} = \sqrt{(\Delta y)^2 + (\Delta\phi)^2} = 0.2$, where y is the rapidity, from a remaining electron candidate is removed. If the electron-jet distance is between 0.2 and 0.4, the electron candidate is removed. If the $\Delta R_{y,\phi}$ between any remaining jet and a muon candidate is less than 0.4, the muon candidate is removed if the jet has more than two associated tracks, otherwise the jet is discarded.

In the differential measurements of the $t\bar{t}Z$ cross-section, two definitions of particles in the generator-level record of the simulation are considered: parton-level and particle-level. While the former leads to a very inclusive phase-space for ease of comparison with fixed-order matrix element calculations, the latter is used to build a fiducial volume much closer to that of the detector-level analysis.

Parton-level objects are obtained from the MC generation history of the $t\bar{t}Z$ system. The top (anti-top) quarks and Z bosons are selected as the last instances in this truth record, after radiation but immediately before their $t \to Wb$ or $Z \to \ell\ell$ decay, respectively. The leptons originating from W and Z bosons are selected as the first instances, immediately following the decay of the parent boson.

[5] The lepton candidates considered for the overlap removed are electrons selected with the 'Loose' identification and muons selected with the Medium identification requirement, but before placing isolation requirements on the leptons.

Particle level refers to a collection of objects which are considered stable in the MC simulation ($\tau \geq 30\,\text{ps}$) but without any simulation of the interaction of these particles with the detector components or any additional pp interaction. Unlike parton-level objects, also the hadronisation of the quarks is featured. Particle-level leptons are selected as leptons originating from the decay of a W or Z boson. The four-momentum of electrons or muons is summed with the four-momenta of all radiated photons within a cone of size $\Delta R = 0.1$ around its direction, excluding photons from hadron decays. The parents of the electrons or muons are required not to be a hadron or quark (u,d,s,c,b). The particle-level jets are reconstructed with the anti-k_t algorithm with a radius parameter of $R = 0.4$ based on all stable particles, but excluding the selected electrons, muons, photons used in the definition of the selected leptons and neutrinos originating from the Z boson or top quarks. If b-hadrons with $p_{\text{T}} > 5$ GeV are found in the MC decay chain, they are clustered in the stable-particle jets with their energies set to zero. Particle-level jets containing one or more of these b-hadrons are considered to originate from a b-quark (ghost-matching) [90, 93]. The particle-level missing transverse energy is defined as the vector sum of the transverse momenta of all neutrinos found in the simulation history of the event, excluding those originating from hadron decays.

5 Analysis strategy

The signal regions (SRs) used in this analysis are intended to offer the highest possible purity of $t\bar{t}Z$ events, as well as sufficient yields in order to perform a differential measurement of the $t\bar{t}Z$ cross section. The analysis is performed in three orthogonal channels, distinguished by lepton multiplicity. A multivariate (MVA) approach is employed in each channel to better discriminate the signal and background processes. An improvement on the previous measurement [23], the MVA analysis has the largest impact on the dilepton (2ℓ) and trilepton (3ℓ) channels that have large background contributions, whereas the tetralepton (4ℓ) channel already exhibits an excellent signal purity at the preselection level. The MVA input variables consist mostly of kinematic variables for individual objects such as jets and leptons, b-tagging information for jets and kinematics of the reconstructed top quarks and Z boson. The exact list of the variables can be found in Tables 22, 23 and 24.

The neural networks in the three channels are trained using the `Keras` [94] backend of `Tensorflow` [95]. In all cases, the Adam optimiser is used for training. In the 3ℓ channel, the categorical cross-entropy loss is minimised. The networks in the 2ℓ and 4ℓ channels employ binary cross-entropy as the loss function. These networks cater to binary classification scenarios, albeit with varying objectives. To ensure optimal performance, the hyperparameters of all networks are tuned using a grid search, which systematically varies the number of layers, activation functions, and regularization techniques such as batch normalization and dropout. Additionally, K-folding techniques [96] are employed to enable comprehensive training and evaluation of the entire set of MC simulations. This approach ensures that the networks are trained and tested on statistically independent subsets of the MC simulation.

5.1 Dilepton signal regions

The dilepton channel targets $t\bar{t}Z$ events where the $t\bar{t}$ system decays hadronically while an opposite-sign same-flavour (OSSF) pair of leptons originates from the Z boson. Events are required to have exactly one pair of OSSF leptons. The invariant mass of the lepton pair is required to be within 10 GeV of the Z boson mass [97], with the two leptons required to have transverse momentum of at least 30 GeV and 15 GeV respectively.

The 2ℓ channel generally suffers from a low signal-to-background ratio, with the $t\bar{t}$ and Z+jets processes (both characterised by the presence of two prompt[6] leptons) constituting major backgrounds. Three signal regions are defined, based on jet and b-tagged jet (at 77% b-tagging efficiency) multiplicities (N_{jets} and $N_{b-\text{tagged jets@77\%}}$ respectively). The splitting is motivated by the different background compositions and the fact that for the events with only 5 jets it is not possible to fully reconstruct the $t\bar{t}$ system. In SR-2ℓ-5j2b, exactly 5 jets are required, of which at least two must be b-tagged; SR-2ℓ-6j2b SR provides its jet-inclusive complement (at least 6 jets). SR-2ℓ-6j1b, inclusive in jet multiplicity (at least 6 jets) but requiring exactly one b-tagged jet, targets events with the appropriate jet multiplicity for tree-level $t\bar{t}Z$ events but with one non-identified b-tagged jet. All dileptonic preselections and SR selections are summarised in Table 2.

To improve the separation between the $t\bar{t}$ and Z+jets background processes and the $t\bar{t}Z$ signal, one deep neural network (DNN) is trained for each signal region on events passing the corresponding selection. The categorisation of events into signal regions based on jet and b-tagged-jet multiplicities allows for the DNNs to be tuned on different background compositions and signal-to-background ratios, enhancing the overall performance. This is particularly needed here, given the much larger background contributions than in the other two analysis channels. All DNNs are constructed as binary classification networks (with $t\bar{t}Z$ as signal and all other processes as background) and the distributions of the DNN outputs are used directly in the inclusive measurement and are not employed in the definition of the signal regions. Details of the variables used in the training of the DNN are given in Table 22 in the Appendix.

Table 2: Definition of the dilepton signal regions.

Variable	**Preselection**		
N_ℓ $(\ell = e, \mu)$	$= 2$		
	$= 1$ OSSF lepton pair with $\lvert m_{\ell\ell} - m_Z \rvert < 10$ GeV		
p_{T} (ℓ_1, ℓ_2)	$> 30,\ 15$ GeV		
	SR-2ℓ-5j2b	**SR-2ℓ-6j1b**	**SR-2ℓ-6j2b**
N_{jets} $(p_{\text{T}} > 25$ GeV)	$= 5$	≥ 6	≥ 6
$N_{b-\text{tagged jets@77\%}}$	≥ 2	$= 1$	≥ 2

5.2 Trilepton signal regions

A trilepton preselection is defined by requiring exactly 3 signal leptons, and their transverse momenta must be higher than 27, 20 and 15 GeV. Amongst these three leptons, the OSSF pair with invariant mass closest to the Z boson mass is considered to originate from the Z decay, and its invariant mass ($m_{\ell\ell}$) has to be compatible with the mass of the Z boson within 10 GeV. Further, all OSSF lepton combinations are required to have $m_{\text{OSSF}} > 10$ GeV to remove contributions arising from low-mass resonances, which are not included in the simulation. At least three jets are required, of which at least one has to be b-tagged (with 85% tagging efficiency). All trileptonic preselections and SR selections are summarised in Table 3.

A 3-class DNN is trained to identify $t\bar{t}Z$, tZq and diboson events amongst those kept after the 3ℓ preselection is applied. Table 23 in the Appendix details the variables used in the DNN. The trilepton phase-space

[6] The term 'prompt' refers to leptons which are directly produced by the hard-scatter process or by the decays of heavy resonances such as W, Z or Higgs bosons.

after preselection is partitioned into three signal regions labelled SR-3ℓ-ttZ, SR-3ℓ-tZq and SR-3ℓ-WZ, according to the largest output of the 3 decision nodes. These selections are summarised in Table 3. While the tZq and $WZ + b$ contributions are largest in SR-3ℓ-tZq and SR-3ℓ-WZ, respectively, these regions still contain a non-negligible amount of $t\bar{t}Z$ signal events. The three SRs are mutually exclusive by construction and together fill the entire phase-space after preselection. A tighter b-tagging requirement (at least one b-tagged jet at 60% efficiency) is then additionally applied in SR-3ℓ-WZ to efficiently suppress the contributions from the $WZ + l$ and $WZ + c$ backgrounds, retaining only the $WZ + b$ component since it is an important background also in the other two SRs.

Table 3: Definition of the trilepton signal regions.

Variable	**Preselection**		
N_ℓ $(\ell = e, \mu)$	$= 3$		
	≥ 1 OSSF lepton pair with $\lvert m_{\ell\ell} - m_Z \rvert < 10$ GeV		
	for all OSSF combinations: $m_{\text{OSSF}} > 10$ GeV		
p_{T} (ℓ_1, ℓ_2, ℓ_3)	$> 27,\ 20,\ 15$ GeV		
N_{jets} $(p_{\text{T}} > 25$ GeV)	≥ 3		
$N_{b-\text{tagged jets}}$	≥ 1@85%		
	SR-3ℓ-ttZ	**SR-3ℓ-tZq**	**SR-3ℓ-WZ**
DNN-tZq output	< 0.40	≥ 0.40	—
DNN-WZ output	< 0.22	< 0.22	≥ 0.22
$N_{b-\text{tagged jets}}$	—	—	≥ 1@60%

5.3 Tetralepton signal regions

The tetralepton channel is defined by the requirement of exactly four leptons, of which at least one must have transverse momentum greater than 27 GeV and two must form an OSSF pair with invariant mass within 20 GeV of the Z boson mass. The sum of the lepton charges is required to be zero. Low-mass dilepton resonances are removed by requiring that the invariant mass of all OSSF pairs is greater than 10 GeV. The OSSF pair with invariant mass closest to that of the Z boson is taken to be the Z candidate; selected events can then be further categorised according to the flavour of the non-Z lepton pair, into a same-flavour (SF) or different-flavour (DF) signal region. As a result, the ZZ+jets background populates mostly the SF region. Additionally, at least two jets, of which at least one b-tagged jet (with 85% tagging efficiency), are required. All tetraleptonic preselections and SR selections are summarised in Table 4.

To achieve a better signal sensitivity, a DNN is trained in both signal regions to discriminate between the $t\bar{t}Z$ signal and background processes, with the input variables listed in Table 24 of the Appendix. Events featuring two pairs of same-flavour leptons are particularly sensitive to contributions from the ZZ+jets background process; they can be removed from the SR by applying a selection requirement on the DNN output. The SR definitions are summarised in Table 4.

Table 4: Definition of the tetralepton signal regions.

Variable	**Preselection**	
N_ℓ $(\ell = e, \mu)$	$= 4$	
	≥ 1 OSSF lepton pair with $\lvert m_{\ell\ell} - m_Z \rvert < 20$ GeV	
	for all OSSF combinations: $m_{\text{OSSF}} > 10$ GeV	
p_{T} $(\ell_1, \ell_2, \ell_3, \ell_4)$	$> 27,\ 7,\ 7,\ 7$ GeV	
The sum of lepton charges	$= 0$	
N_{jets} $(p_{\text{T}} > 25$ GeV)	≥ 2	
$N_{b-\text{tagged jets}}$	≥ 1@85%	
	SR-4ℓ-SF	**SR-4ℓ-DF**
$\ell\ell^{\text{non-Z}}$	e^+e^- or $\mu^+\mu^-$	$e^\pm\mu^\mp$
DNN output	≥ 0.4	—

5.4 Particle- & parton-level selections

The particle- and parton-level selections for the 3ℓ and 4ℓ channels used for the differential measurements are summarised in Table 5. The particle-level fiducial regions are constructed to follow closely the detector-level regions, using the particle-level object definitions described in Section 4 with at least one OSSF lepton pair within ±10 GeV of the m_Z value as quoted in the PDG. The parton-level fiducial volumes are defined by the top-quark decays; semi-leptonic (e, μ+jets only) in the 3ℓ channel, and dileptonic ($e^+e^-, e^\pm\mu^\mp, \mu^+\mu^-$ only) in the 4ℓ channel. The Z boson is required to decay dileptonically via $Z \to e^+e^-, \mu^+\mu^-$. Events featuring tau leptons which originate directly from either the Z boson or the W bosons from the $t\bar{t}$ system are removed from the parton-level fiducial volume and are not considered in the unfolding, regardless of their subsequent decay. The differential variables are reconstructed from the top quarks after final state radiation, immediately prior to their decays. The invariant mass of the two leptons from the Z decay is required to be within ±15 GeV of the m_Z value as quoted in the PDG; increasing this mass window at parton-level diminishes the impact of reconstruction and acceptance efficiencies on the unfolding procedure.

5.5 Top quark reconstruction

Several different approaches for the kinematic reconstruction of either the $t\bar{t}$ system or the single (anti-)top quarks are employed and explained in the following, tailored to the characteristics of the various $t\bar{t}Z$ decay channels considered in this analysis. A brief summary for each channel is given in the following.

5.5.1 2ℓOS reconstruction

In the 2ℓOS channel, two methods are employed for the reconstruction of the $t\bar{t}$ system. The outputs of both of these algorithms are used for the construction of variables that are subsequently used for the training of neural networks since they provide complementary information that can be used to separate between the signal and background processes.

Table 5: Definition of the fiducial volumes at particle- and parton-level. Leptons refer exclusively to electrons and muons: they are dressed with additional photons at particle-level, but not at parton-level.

Particle-level selection	
3ℓ channel	4ℓ channel
Exactly 3 leptons, with $p_{\mathrm{T}}(\ell_1, \ell_2, \ell_3) > 27, 20, 15$ GeV	Exactly four leptons, with $p_{\mathrm{T}}(\ell_1, \ell_2, \ell_3, \ell_4) > 27, 7, 7, 7$ GeV
The sum of charges is ± 1	The sum of charges is = 0
At least 3 jets, with $p_{\mathrm{T}} > 25$ GeV	At least 2 jets, with $p_{\mathrm{T}} > 25$ GeV
At least 1 b-jet (jet ghost-matched to a b-hadron)	
At least one OSSF lepton pair, with $\lvert m_{\ell\ell} - m_Z \rvert < 10$ GeV	
Parton-level selection	
3ℓ channel	4ℓ channel
$t\bar{t} \to e^{\pm}/\mu^{\pm}$ + jets	$t\bar{t} \to e^{\pm}\mu^{\mp}/e^{\pm}e^{\mp}/\mu^{\pm}\mu^{\mp}$
$Z \to e^{\pm}e^{\mp}/\mu^{\pm}\mu^{\mp}$	
$\lvert m_{\ell\ell} - m_Z \rvert < 15$ GeV	

The first method, referred to as *multi-hypothesis hadronic top/W reconstruction method*, targets the fully hadronically decaying $t\bar{t}$ system associated to the signal process taking into account several hypotheses for the number of available and missing top-quark final state particles. At tree-level six jets from the fully-hadronic decay of the $t\bar{t}$ system are part of the 2ℓOS $t\bar{t}Z$ signature, however due to the jet energy resolution and coverage of the detector, some jets associated to a final state quark may not be reconstructed. Five different scenarios[7] are considered for the reconstruction procedure, depending on the number of hadronically decaying W bosons and top quarks possible to reconstruct, each giving an output weight. For each hypothesis, all jets-to-quarks assignments are tested and the probability of the hypothesis and combination is calculated based on known distributions of two (three) jets invariant mass originating from W boson (top quark). The final weight for each hypothesis is the probability of the most likely jet permutation and the permutation is considered correct for a given hypothesis.

An alternative approach attempts reconstruction of the all-hadronic $t\bar{t}$ system through the use of SPANet (Symmetry Preserving Attention Network), an attention-based neural network originally designed for the reconstruction of all-hadronic $t\bar{t}$ events [98]. The network was trained for the dilepton $t\bar{t}Z$ topology using both the nominal and alternative $t\bar{t}Z$ samples, required to pass the 2ℓOS selection from Table 2 and at least 6 jets (at least one b-tagged). One or both top quarks have to be correctly matched, where correct jet assignments are constructed by matching detector level objects to parton level. Inputs are the kinematic and b-tagging information of all jets present in the event, as well as the correct jet assignments. The network predicts the jet assignments for the top and antitop quarks. It assigns jets to the top quarks correctly in $\approx$56% events, if the jets from the top-quarks are present. The transverse momentum of the reconstructed all-hadronic $t\bar{t}$ system, $p_{\mathrm{T}}^{t\bar{t}}$, is then used as an input to the MVA discriminant in the 2LOS channel.

[7] Considered scenarios: jets from one W boson are present, jets from two W bosons are present, jets from one top-quark are present, jets one top-quark and one W boson are present and jets both top-quarks are present.

5.5.2 3ℓ reconstruction

The full reconstruction of the $t\bar{t}$ system for 3ℓ events is performed by first reconstructing the leptonic-side top quark[8] and subsequently reconstructing the hadronic-side top quark. For the leptonic-side the E_T^{miss} is attributed to the neutrino from the associated W boson decay. The neutrino momentum in the z direction ($p_{\nu z}$) can be determined from the quadratic equation constrained by the SM W boson mass, leading to up to two distinct solutions, which are both considered. In the few cases where no real solution exists, the neutrino p_{T} is adjusted such that the quadratic determinant becomes zero and a single solution for $p_{\nu z}$ exists. Each W boson candidate is then paired to the nearest (in ΔR) b-tagged jet. The most likely top quark candidate is determined from the $p(m_{bl\nu})$ probability density distribution obtained from MC $t\bar{t}Z$ simulations.

The hadronic-side reconstruction builds top quark candidates from jet pairs compatible with a W boson, and a b-tagged jet. As the b-tagged jet has already been determined at this point by the leptonic-side, the remaining of the two jets with the highest b-tagging score is assigned to the hadronic-side top quark. From all the other jets, the two most compatible to have originated from a W boson are determined via interpolation of m_{jj} with the reference distributions used in the multi-hypothesis reconstruction method.

The exact same top reconstruction algorithms are applied at particle-level, using the two highest p_{T} jets that have been ghost-matched to b-hadrons to define the b-candidates.

5.5.3 4ℓ reconstruction

In this channel a full kinematic reconstruction of the $t\bar{t}Z$ system is performed employing the Two Neutrino Scanning Method (2νSM), improving over the previous analysis [23] where it was reconstructed in the transverse plane only. Values of the azimuthal angle and pseudorapidity of either neutrino are tested by systematically scanning the η-ϕ-space and, with the set of the respective values at each point in η-ϕ-space of the two neutrinos, the $t\bar{t}$ signature is constructed with the information from the two leptons not associated with the Z boson decay and two jets with the highest b-tagging score.

Kinematic constraints from reference distributions are used to create a single output weight, $w_{2\nu\text{SM}}$, for all hypotheses and then the combination with the largest weight is selected as the reconstructed dileptonic $t\bar{t}$ system. This output weight is showing a high discrimination power between $t\bar{t}Z$ and dileptonic $t\bar{t}$ and therefore can be used as a discriminating variable for MVA training.

At particle-level, a pseudo-top-quark reconstruction algorithm is employed. First the two leading p_{T} neutrinos (from the truth record) are associated with the two charged leptons left in the event after the Z boson candidate has been determined. From the two possible lepton-neutrino pairings, the one that yields an invariant mass closest to the W boson mass is retained. The two highest p_{T} jets that have been ghost-matched to b-hadrons define the b-candidates; where only one such jet exists in the event, the second b-candidate is taken to be the leading p_{T} jet amongst those left available. As before, both pairings of b- and W-candidates are considered, and the one that yields an invariant mass closest to the MC top quark mass (172.5 GeV) is used to define the reconstructed top and antitop quarks.

[8] The term leptonic-side top quark is taken to mean the top or anti-top quark from the $t\bar{t}$ pair for which the W boson decays via $W \to \ell\nu$, and similarly $W \to q'\bar{q}$ for the term hadronic-side.

6 Background estimation

Several processes can lead to background contaminations in the signal regions. The contributions from SM processes featuring the production of two, three or four prompt leptons is discussed in Section 6.1, whereas the estimation of processes where at least one of the reconstructed leptons is a lepton from a non-prompt process is explained in Section 6.2.

6.1 Prompt lepton backgrounds

6.1.1 Prompt backgrounds in 2ℓ regions

The opposite-sign dilepton channel is dominated by two large, prompt contributions: dileptonic $t\bar{t}$ and Z+jets. The former enters primarily in the regions where the two $b-$jets can be tagged and reconstructed; it makes up 35% of the total expected event yields in the SR-2ℓ-5j2b and SR-2ℓ-6j2b signal regions, but only 10% in SR-2ℓ-6j1b. The Z+jets process, on the other hand, contributes to around 80% of the event yields in the SR-2ℓ-6j1b signal region; this number reduces to $55-60$% in the other two regions. Since the modelling of Z+jets in high jet multiplicity regions can be problematic, especially in association to heavy-flavour jets, it is important to correct the predictions obtained from MC simulations with data: the normalisation of the $Z+b$ and $Z+c$ components are therefore obtained in data, simultaneously to the extraction of the signal strength in the combined inclusive fit described in Section 8.

To better model the $t\bar{t}$ process, a fully data-driven approach is instead preferred, which relies on the high $t\bar{t}$ purity of an $e\mu$ selection. Additional selection criteria are applied to replicate those of the signal regions, as defined in Table 2, and therefore limit the extrapolation between regions only to the change in lepton flavour to an OS different flavour (DF) lepton pair ($e^{\pm}\mu^{\mp}$ in the regions used for the data-driven $t\bar{t}$ estimate, $e^{\pm}e^{\mp}/\mu^{\pm}\mu^{\mp}$ in the SRs). These requirements are summarised in Table 6 below. To estimate the $t\bar{t}$ background in the signal regions, the distributions of the DNN output in data in these regions are used: 2ℓ-$e\mu$-6j1b, 2ℓ-$e\mu$-6j2b and 2ℓ-$e\mu$-5j2b.

Table 6: Definition of the dilepton regions used for data-driven estimate of the $t\bar{t}$ background.

Variable	**Preselection**		
N_ℓ $(\ell = e, \mu)$	$= 2$		
	$= 1$ OSDF lepton pair with $\lvert m_{\ell\ell} - m_Z \rvert < 10$ GeV		
p_{T} (ℓ_1, ℓ_2)	$> 30,\ 15$ GeV		
	2ℓ-$e\mu$-5j2b	**2ℓ-$e\mu$-6j1b**	**2ℓ-$e\mu$-6j2b**
N_{jets} $(p_{\mathrm{T}} > 25$ GeV)	$= 5$	≥ 6	≥ 6
$N_{b-\text{tagged jets@77\%}}$	≥ 2	$= 1$	≥ 2

To be able to use the distribution of the DNN output from data $e\mu$ events in the $\ell\ell$ signal regions, the different acceptances and efficiencies need to be considered, and the non-$t\bar{t}$ background must be taken into account. The MC prediction for all non-$t\bar{t}$ background is first subtracted from the distribution of the DNN

output in the $e\mu$ data. Then, the following correction factor is applied to the resulting data $e\mu$ distributions of the DNN output:

$$C_{t\bar{t}} = \frac{N_{t\bar{t}}^{\ell\ell}}{N_{t\bar{t}}^{e\mu}}, \tag{1}$$

where $N_{t\bar{t}}^{\ell\ell}$ and $N_{t\bar{t}}^{e\mu}$ are the number of expected $t\bar{t}$ events (from MC predictions) after the $\ell\ell$ selection in the SRs and the $e\mu$ selection in the regions for data-driven $t\bar{t}$ estimate, respectively. A total uncertainty on this number is derived including both the MC statistical error as well as differences between the prediction of alternative MC generators, obtained by comparing the nominal value of the ratio to the value obtained considering h_{damp} parameter variation, different showering generator (HERWIG 7.0.4) and different matrix element generator (MADGRAPH5_AMC@NLO 2.3.3). The correction factors obtained in each region are found to be very close to each other, and therefore a unique average factor of 0.982 ± 0.009 is used to apply the $e\mu \rightarrow \ell\ell$ correction in all dilepton signal regions. In addition to this uncertainty, the statistical uncertainty related to the Poisson fluctuations of the data and MC statistical uncertainty of the subtracted MC backgrounds are taken into account for this background bin-by-bin in all regions. Distributions for the p_T of the leading jet in 2ℓ-$e\mu$-5j2b, b-tagged-jet multiplicity in 2ℓ-$e\mu$-6j2b and jet multiplicity in 2ℓ-$e\mu$-6j1b are shown in Figure 1. The distribution of the b-tagged-jet multiplicity in particular highlights the need for this data-driven approach, in order to overcome the MC mismodelling.

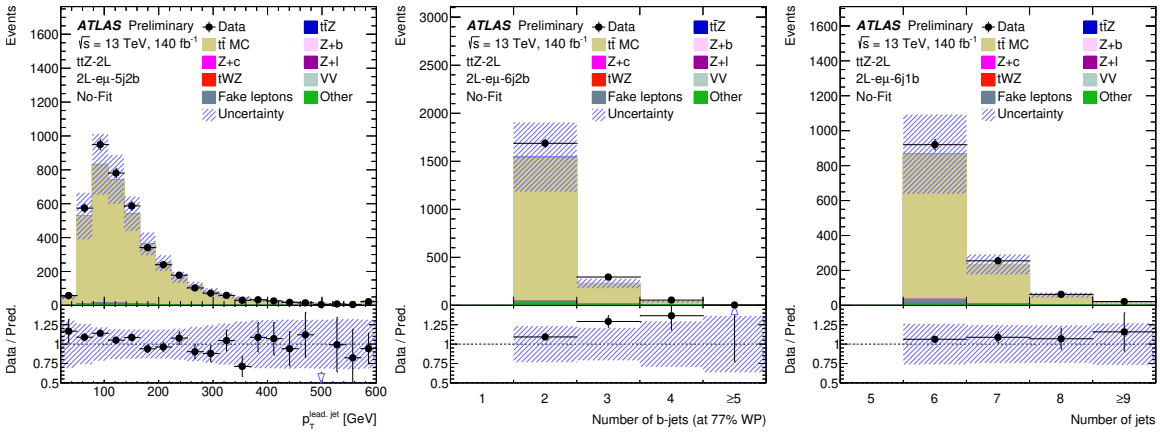

(a) (b) (c)

Figure 1: Distributions of: (a) the transverse momentum of the leading jet in 2ℓ-$e\mu$-5j2b, (b) the number of b-tagged jets in 2ℓ-$e\mu$-6j2b, and (c) the number of jets in 2ℓ-$e\mu$-6j1b. The shaded band corresponds to the total uncertainty (systematic and statistical) of the total pre-fit SM prediction. The lower panel shows the ratio of the data to the SM prediction. The last bin includes also the overflow. These regions are not included in the fit and are only used for fully data-driven estimate of the $t\bar{t}$ background in the dilepton signal regions.

6.1.2 Prompt backgrounds in 3ℓ regions

The dominant background processes in the trilepton signal regions are WZ+jets (with $WZ \rightarrow \ell\ell\ell\nu$) and tZq production. The heavy-flavour components of WZ+jets, in particular $WZ + b$, is most relevant, accounting for $\sim 5\%$ of the predicted event yields in SR-3ℓ-ttZ, $\sim 8\%$ in SR-3ℓ-tZq and $\sim 31\%$ in SR-3ℓ-WZ. The $WZ + c$ and $WZ + l$ contributions are roughly 3 and 20 times smaller, respectively. The tZq background is most relevant in SR-3ℓ-tZq, where it makes up $\sim 22\%$ of the predicted event yields – while the $t\bar{t}Z$

signal process is still twice as large. Since the tZq process cannot be completely separated from $t\bar{t}Z$, it is kept fixed to its best SM prediction and an appropriate set of normalisation and shape uncertainties are considered. The $WZ + b$ background, on the other hand, can be normalised to data due to a high contribution compared to other processes in SR-3ℓ-WZ. Another relevant process is tWZ, an irreducible singly-resonant background to $t\bar{t}Z$. Due to its kinematic properties being so close to those of the signal process, no efficient discrimination can be obtained from the neural network used to define the 3ℓ signal regions: the tWZ process therefore yields a flat $6-10\%$ contribution across the various DNN discriminant bins.

6.1.3 Prompt backgrounds in 4ℓ regions

The main background in the tetralepton channel is ZZ+jets, with $ZZ \to \ell^+\ell^-\ell'^+\ell'^-$. This background affects mostly the same-flavour signal region, but can also contribute in a minor way to the different-flavour region through $Z \to \tau^+\tau^- \to e^\pm\mu^\mp\nu_{\tau^+}\nu_{\tau^-}\nu_{e^\mp}\nu_{\mu^\pm}$. As for the trilepton channel, the tWZ process is a significant irreducible background, contributing between 8% and 10% of the total event yields in the signal regions. Other rare processes, such as VH or $t\bar{t}H$, have a contribution typically $\lesssim 2\%$. The contribution of the ZZ+jets process in the same-flavour signal region is about 13%, mostly from the $ZZ + b$ component: it is therefore useful to design a dedicated control region to normalise this component in data. The definition of the CR-4ℓ-ZZ is given in Table 7 below. It is similar to that of SR-4ℓ-SF (see Table 4), but relies on an inverted cut of the DNN discriminant to ensure orthogonality. To suppress contributions from the $ZZ + l$ and $ZZ + c$ components in the extraction of the $ZZ + b$ normalisation (each contributing approximately a third of the processes), the control region is split into two bins based on the PCBT bin value of the b-tagged jet with the highest value of PCBT bin. The first bin contains events for which it is tagged at the 85%, 77% and 70% WPs, while the second bin corresponds to the tightest 60% WP. The second bin is dominated by the $ZZ + b$ background, and there is non-negligible $ZZ + l$ and $ZZ + c$ contamination in the first bin.

Table 7: Definition of the tetralepton control region.

Variable	**Preselection**
N_ℓ $(\ell = e, \mu)$	$= 4$
	≥ 1 OSSF lepton pair with $\lvert m_{\ell\ell} - m_Z \rvert < 20$ GeV
	for all OSSF combinations: $m_{\text{OSSF}} > 10$ GeV
p_{T} $(\ell_1, \ell_2, \ell_3, \ell_4)$	$> 27,\ 7,\ 7,\ 7$ GeV
The sum of lepton charges	$= 0$
N_{jets} $(p_{\text{T}} > 25$ GeV)	≥ 2
$N_{b-\text{tagged jets}}$	≥ 1@85%
	CR-4ℓ-ZZ
$\ell\ell^{\text{non-Z}}$	e^+e^- or $\mu^+\mu^-$
DNN-SF output	< 0.4

6.2 Non-prompt/fake lepton background

Fake or non-prompt leptons are objects unintentionally misidentified as prompt leptons. They can originate from various sources including meson decays, photon conversions or light jets accidentally creating lepton-like detector signatures. In the signal regions the typical source of non-prompt leptons[9] are due to the semi-leptonic decay of heavy-flavour hadrons, mainly from contributions from $t\bar{t}$ and Z+jets processes. While the impact of fake leptons is negligible in the 2ℓ channel, the contribution is up to 12%(5%) of the total expected yields in the $3\ell(4\ell)$ SRs.

Due to the low amount of fake leptons in the dilepton channel, the MC estimate of the fake lepton backgrounds is used with a conservative 50% normalisation uncertainty. To estimate the contribution of fake leptons in the trilepton and tetralepton signal regions, a semi-data-driven method is used. The template fit method relies on the normalisation in data of dedicated MC templates for each source of fake leptons, using truth information about the MC origin and type of the fake leptons. Four distinct MC templates are defined based on the major source of fakes for this analysis: electrons from heavy-flavour sources ("F-e-HF"), electrons from other sources ("F-e-Other"), muons from heavy-flavour sources ("F-μ-HF"), and any other fake events not belonging to any of the other sets or events containing multiple fake leptons ("F-Other"). Only this last category is not normalised in data, and receives instead a 50% normalisation uncertainty.

To remain as kinematically close as possible to the 3ℓ signal regions, where the fake contribution is most important, a set of trilepton control regions are designed. These employ the same lepton p_{T}, jet and b-tagged jet multiplicity requirements as in the SRs. To ensure orthogonality with the SRs defined in Table 3, exactly one lepton is required to not satisfy the identification and isolation requirements applied to signal leptons – this lepton is referred to as "loose". The heavy-flavour fake components can be isolated by defining $t\bar{t}$-enriched control regions: any event with an OSSF pair of leptons is vetoed, and the loose lepton is required to be part of the same-sign pair of leptons. The flavour of the loose lepton is then used to categorise events into CR-$t\bar{t}$-e or CR-$t\bar{t}$-μ. On the other hand, the "F-e-Other" component can be obtained in a Z-like selection (CR-Z-e), requiring exactly three electrons of which two form an OS pair, and vetoing events with $E_{\mathrm{T}}^{\mathrm{miss}}$ greater than 80 GeV. These selection criteria are summarised in Table 8 below.

The extraction of the three fake factors ($\mathcal{N}_{e,\mathrm{HF}}$, $\mathcal{N}_{e,\mathrm{other}}$ and $\mathcal{N}_{\mu,\mathrm{HF}}$) is first performed independently of the inclusive combined fit to determine an additional uncertainty due to non-closure of key kinematic distributions in the Fake Factor CRs to be applied to the fake templates in the SRs, defined to be 20% on fake electrons and 10% on fake muons, and later used in the combined fits. In CR-$t\bar{t}$-e and CR-$t\bar{t}$-μ, the overall event yields are used in template fit, while in CR-Z-e, the distribution of transverse mass of the W boson is fitted in 6 bins. These distributions are displayed in Figure 2 with the corresponding event yields in Table 9 after the inclusive combined fit to data.

[9] Hereafter referred to as "fake leptons" or "fakes".

Table 8: Definition of the trilepton fakes control regions.

Variable	**Preselection**		
N_ℓ $(\ell = e, \mu)$	= 3 (of which = 1 loose non-tight)		
p_{T} (ℓ_1, ℓ_2, ℓ_3)	$> 27,\ 20,\ 15$ GeV		
Sum of lepton charges	± 1		
N_{jets} $(p_{\mathrm{T}} > 25$ GeV)	≥ 3		
$N_{b-\mathrm{tagged\ jets}}$	≥ 1@85%		
	CR-$t\bar{t}$-e	**CR-$t\bar{t}$-μ**	**CR-Z-e**
Lepton flavours	no OSSF pair	no OSSF pair	OSSF pair
	(loose lepton is an electron)	(loose lepton is a muon)	(exactly 3 electrons)
$E_{\mathrm{T}}^{\mathrm{miss}}$	—	—	< 80 GeV

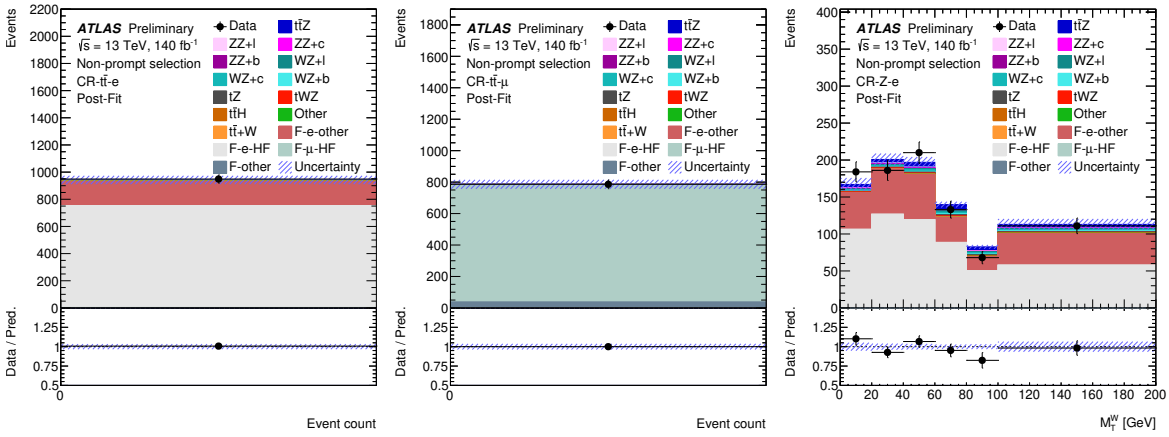

(a) (b) (c)

Figure 2: Post-fit distributions of: the overall event yields in (a) CR-$t\bar{t}$-e and (b) CR-$t\bar{t}$-μ, and (c) of the W boson transverse mass in CR-Z-e. The shaded band corresponds to the total uncertainty (systematic and statistical) of the total SM prediction. The lower panel shows the ratio of the data to the SM prediction. The last bin includes also the overflow.

Table 9: Observed and expected event yields in the fake factor control regions, obtained for an integrated luminosity of 140 fb^{-1} after the combined fit to data. The indicated errors include the Monte Carlo statistical uncertainty as well as all other systematic uncertainties discussed in Section 7. A dash (—) indicates event yields smaller than 0.1.

	CR-$t\bar{t}$-e	CR-$t\bar{t}$-μ	CR-Z-e
$t\bar{t}Z$	2.53 ± 0.21	0.71 ± 0.12	33.5 ± 1.4
$ZZ + l$	—	—	3.8 ± 1.1
$ZZ + c$	—	—	2.99 ± 0.95
$ZZ + b$	—	—	3.5 ± 1.8
$WZ + l$	0.29 ± 0.13	—	7.8 ± 3.1
$WZ + c$	0.36 ± 0.13	—	11.2 ± 4.3
$WZ + b$	0.16 ± 0.10	—	5.8 ± 3.3
tZq	0.21 ± 0.05	—	6.55 ± 0.99
tWZ	0.26 ± 0.04	—	3.81 ± 0.41
$t\bar{t}W$	2.9 ± 1.5	1.50 ± 0.75	1.41 ± 0.71
$t\bar{t}H$	4.46 ± 0.38	2.31 ± 0.20	3.20 ± 0.29
Other	1.2 ± 0.54	0.72 ± 0.32	0.52 ± 0.23
F-e-Other	177 ± 50	—	267 ± 72
F-e-HF	749 ± 70	—	548 ± 56
F-μ-HF	0.25 ± 0.02	744 ± 31	—
F-Other	3.0 ± 1.4	36 ± 16	1.03 ± 0.52
Total	943 ± 30	786 ± 28	901 ± 28
Data	949	786	892

7 Systematic uncertainties

The signal and background predictions in all regions are affected by several sources of experimental and theoretical systematic uncertainty. These are considered for both inclusive and differential measurements presented in Sections 8 and 9. The uncertainties can be classified into the different categories which are described in the following subsections.

7.1 Detector-related uncertainties

The uncertainty in the combined 2015–2018 integrated luminosity is 0.83% [32]. This systematic uncertainty affects all processes determined from MC simulations for which the normalization is not extracted from data.

The uncertainty in the reweighting of the MC pile-up distribution to match the distribution in data is evaluated by varying the pile-up correction factors and has a small impact on both the inclusive and differential results.

Uncertainties associated with the lepton selection arise from the trigger, reconstruction, identification and isolation efficiencies, and the lepton momentum scale and resolution [81–84]. They are below 1% for the individual sources and have a total impact of 1–3% on the inclusive measurements.

Uncertainties associated with the jet selection arise from the jet energy scale (JES), the JVT requirement and the jet energy resolution (JER). The JES and its uncertainties are derived by combining information from test-beam data, collision data and simulation [88]. The JER has been measured separately for data and MC using two in-situ techniques and a systematic uncertainty is defined as the quadratic difference between the jet energy resolutions for data and simulation. The uncertainties in the JER and JVT increase at lower jet p_{T}.

The efficiency of the flavour-tagging algorithm is measured for each jet flavour using control samples in data and in simulation. From these measurements, correction factors are derived to correct the tagging rates in the simulation. In the case of b-tagged jets, the correction factors and their uncertainties are estimated from data using dileptonic $t\bar{t}$ events [90]. In the case of c-tagged jets, they are derived from jets arising from W boson decays in $t\bar{t}$ events [99]. In the case of light-flavour jets, the correction factors are derived using dijet events [100]. Sources of uncertainty affecting the b- and c-tagging efficiencies are evaluated as a function of jet p_{T}, including bin-to-bin correlations. The uncertainties in the efficiency for tagging light-flavour jets depend on the jet p_{T} and on η. An additional uncertainty is assigned to account for the extrapolation of the b-tagging efficiency measurement from the p_{T} region used to determine the correction factors to regions with higher p_{T}. The impact of flavour-tagging uncertainties on the measurements depends on the signal regions and is 1.7% in total.

Uncertainties are applied to the scale and resolution of the soft track component of the missing transverse energy. They are derived from the agreement between data and MC of the p_{T} balance between the hard and soft E_T^{miss} components [101].

7.2 Signal modelling uncertainties

To obtain the uncertainties related to missing higher order effects, the renormalisation and factorisation scale parameters μ_R and μ_F are varied in the matrix element up and down simultaneously by a factor of 2 and compared to the nominal predictions. Uncertainties on the PDF are evaluated following the recommended PDF4LHC prescription [102] and include uncertainties related to the choice of PDF.

The uncertainties associated with the parton showering algorithm and the underlying event model[10] are evaluated by comparing the nominal samples, generated with MadGraph5_aMC@NLO interfaced to Pythia 8, to equivalent samples interfaced to Herwig 7 instead. Uncertainties related to the modelling of initial-state radiation are obtained by varying the Var3c parameter of the Pythia A14 tune in dedicated alternative samples.

The modelling of the $t\bar{t}Z$ signal process is cross-checked by comparing the nominal samples to alternative ones produced with the Sherpa generator, at various levels of precision (see Section 3 for more details). This comparison is not treated as an additional source of systematic uncertainty.

7.3 Background modelling uncertainties

Uncertainties on the $WZ \to \ell\ell\ell\nu$ (WZ+jets) and $ZZ \to \ell\ell\ell\ell$ (ZZ+jets) backgrounds related to the CKKW matching scale, QSF parameter (resummation scale) and alternative recoil scheme are estimated through the use of alternative truth-level samples. The renormalisation and factorisation scale uncertainties are evaluated following the same prescription as for the $t\bar{t}Z$ signal sample: the values of the scales are varied jointly by a factor of 2 and compared to the nominal predictions. Uncertainties related to the choice of PDF are evaluated following the recommended PDF4LHC prescription and are derived by comparing the nominal value to those from the CT14 and MMHT14 PDF sets. Variations of α_s in the nominal PDF are also included. In addition, a normalisation uncertainty of 30% is applied to the $WZ + l$ and $WZ + c$ components of the WZ+jets background, evaluated from discrepancies in data/MC comparisons. Similarly, normalisation uncertainties of 10% and 30% are applied to the $ZZ + l$ and $ZZ + c$ components of the ZZ+jets background.

A cross section normalisation uncertainty of 14% is assigned to the tZq process, based on the dedicated ATLAS measurement presented in Ref. [17]. A parton shower uncertainty is obtained by comparing an alternative sample of tZq events generated with MadGraph5_aMC@NLO interfaced to Herwig 7 to the nominal setup (MadGraph5_aMC@NLO interfaced to Pythia 8). As for $t\bar{t}Z$, variations of the Var3c parameter of the Pythia A14 tune, as well as of the factorisation and renormalisation scales, are considered. Uncertainties related to the choice of PDF are evaluated following the PDF4LHC prescriptions.

For the tWZ background process, no parton shower uncertainty is considered, but instead the difference between samples generated with the DR1 and DR2 diagram removal schemes [59] is treated as a modelling uncertainty. Furthermore, both the shape (acceptance) and normalisation components of this systematic uncertainty are considered: in the absence of higher-order theoretical calculations for the tWZ process, the comparison of the cross sections obtained in the five-flavour scheme in the DR1 and DR2 setups leads to an overall $10 - 15$% normalisation uncertainty. As for the processes described above, PDF and scale uncertainties are taken into account.

[10] In the following only denoted as "parton shower uncertainty".

Only theoretical uncertainties on the normalisation of the cross section of the $t\bar{t}H$ process are considered. Following the NLO QCD+EWK calculation presented in Ref. [19], the scale uncertainty is taken to be $+5.8\% - 9.2\%$ and the PDF+α_s uncertainty $\pm 3.6\%$.

As for the diboson processes, variations of the CKKW matching scale and QSF parameter define independent modelling uncertainties on the Z+jets process. Renormalisation and factorisation scales are further varied up and down by a factor of 2, and PDF uncertainties are evaluated according to the PDF4LHC prescription. The $Z + l$ component, the only one to not be extracted directly from a fit to data, is assigned a 10% normalisation uncertainty [103].

For other minor background processes, such as HV, VVV, $t\bar{t}W$, $t\bar{t}WW$ or multi-top-quark ($tt\bar{t}$, $t\bar{t}t\bar{t}$) production, an overall normalisation uncertainty of 50% is applied. For $t\bar{t}t\bar{t}$, an additional parton shower uncertainty is considered, by comparing samples interfaced to Pythia 8 and Herwig 7. These background components typically contribute $\lesssim 1\%$ of the total event yields in the signal regions. As defined in Section 6.2, the MC template for fake leptons that cannot be normalised in data as part of the Fake Factor method is assigned a 50% normalisation uncertainty. Non-closure uncertainties are derived for the other fake templates.

A few channel-specific exceptions from the above mentioned treatment of the theoretical systematic uncertainties of the background are also included. In the 2ℓ OS channel, the diboson background is significantly smaller than in 3ℓ and 4ℓ channels. Splitting it into 3 flavor components and using all aforementioned mentioned uncertainties would lead to large MC statistical uncertainties in those templates, therefore all diboson events are treated as one background and are assigned a conservative 50% uncertainty. In the 3ℓ channel, the $ZZ + b$ background is not negligible, but still not large enough to measure its normalisation directly in data, as is done in the 4ℓ channel. A 50% normalisation uncertainty is applied instead.

8 Results of the inclusive cross section measurement

The $t\bar{t}Z$ cross section is first measured separately in each channel. A final result is then obtained by simultaneously fitting all three channels.

The fit is based on the profile-likelihood technique [104], with a likelihood function as a product of Poisson probability functions given by the observed event yields in the signal and control regions. The signal strength $\mu_{t\bar{t}Z}$, defined as the ratio between the observed $t\bar{t}Z$ cross section and the cross section predicted by the Monte Carlo, as well as normalisations of some of the backgrounds (specified later in this section) are treated as free parameters of the fit. Systematic uncertainties described in Section 7 are introduced using additional parameters with Gaussian constraints. None of the uncertainties are found to be significantly constrained or pulled in the fit.

Since the signal MC samples with leptonic decay of the Z boson contain also a contribution from $\gamma \to \ell^+\ell^-$, the total cross section has to be corrected in order to remove the photon contribution. In accordance with the previous ATLAS [23] and CMS [22] measurements, the inclusive cross section fiducial volume is defined using the requirement that the invariant mass of the fermion pair originating from Z/γ^* must be close to the Z-boson mass: $70\ \text{GeV} < m_{f\bar{f}} < 110\ \text{GeV}$. The total cross section is thus corrected by the fraction of parton-level events with mass of the fermion pair in this Z mass window; this fraction is found to be 94.5 %, with an uncertainty well below 0.1%. The cross section, after correcting by the scale factor of 0.945, is 0.828 pb.

In the dilepton channel, the distributions of the DNN output are fitted in all 3 SRs. No additional control regions are used. The binning is optimised to achieve the lowest possible $\mu_{t\bar{t}Z}$ uncertainty. The event yields are shown in Table 10 and the post-fit distributions of the DNN output are shown in Figure 3. The free parameters of the dilepton fit are the signal strength and normalisations of $Z + c$ and $Z + b$ backgrounds. The $t\bar{t}$ background is fixed to its estimation from data in $e\mu$ events as described in Section 6.1.1. The fitted value of the cross section can be found in the Table 13.

Table 10: Post-fit event yields in the dilepton signal regions, obtained for an integrated luminosity of 140 fb^{-1}. The values of the fitted parameters from the combined fit are used. Data-driven approach described in Section 6.1.1 is used to estimate $t\bar{t}$ background. The indicated errors include the Monte Carlo statistical uncertainty as well as all other systematic uncertainties discussed in Section 7. Because of rounding and correlations between systematic uncertainties, the values quoted for the total yield and its uncertainty may differ from the simple sum over all processes.

	SR-2ℓ-5j2b	SR-2ℓ-6j2b	SR-2ℓ-6j1b
$t\bar{t}Z$	297 ± 20	443 ± 27	305 ± 28
$t\bar{t}$ DD	4 001 ± 72	1 913 ± 45	1 161 ± 35
$Z + b$	5 710 ± 170	2 680 ± 110	4 830 ± 280
$Z + c$	349 ± 95	189 ± 47	2 020 ± 480
$Z + l$	59 ± 25	19.6 ± 8.1	1 020 ± 240
tWZ	23.2 ± 0.92	34.4 ± 2.1	40.2 ± 1.9
Diboson	150 ± 80	95 ± 52	340 ± 180
Fake leptons	28 ± 14	18.6 ± 9.2	25 ± 12
Other	55 ± 25	49 ± 22	23 ± 10
Total	10 700 ± 100	5 440 ± 68	9 760 ± 110
Data	10 702	5 435	9 737

In the trilepton channel, the distribution of the DNN output, related to the probability of the event being the signal, is fitted in the SR-3ℓ-ttZ and SR-3ℓ-tZq regions. The total number of events is fitted in the SR-3ℓ-WZ region. The post-fit plots for these distributions are shown in Figure 4. The event yields in the trilepton signal regions are shown in Table 11. In addition to the three trilepton signal regions, the 3 fake lepton control regions, shown in Figure 2, are used in the fit to extract the normalisations of the fake lepton backgrounds. The trilepton fit has 5 free parameters: the signal strength, normalisation of the $WZ + b$ background and normalisations of the 3 fake lepton backgrounds. The fitted value of the cross section can be found in Table 13.

In the tetralepton channel, the distributions of the two DNN outputs are fitted in the SR-4ℓ-SF and SR-4ℓ-DF regions. The distribution of the b-tagging score of the leading b-tagged jet is fitted in CR-4ℓ-ZZ. The post-fit plots for these distributions are shown in Figure 5. The event yields in the tetralepton signal regions are shown in Table 11. In addition to the two tetralepton signal regions and ZZ control region, the 3 fake lepton control regions, shown in Figure 2, are used in the fit to extract the normalisations of the fake lepton backgrounds. The tetralepton fit has 5 free parameters: the signal strength, normalisation of the $ZZ + b$ background and normalisations of the 3 fake lepton backgrounds. The fitted value of the cross section can be found in the Table 13.

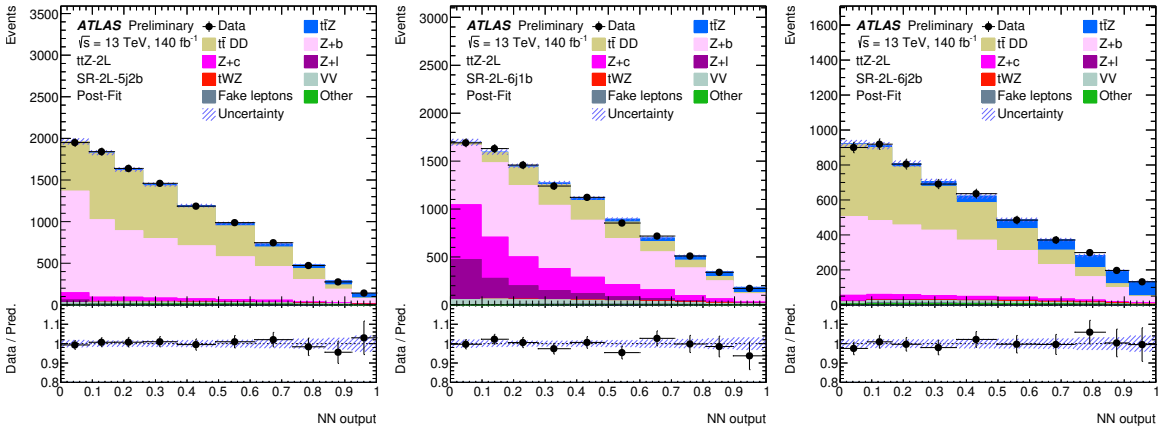

(a) (b) (c)

Figure 3: Distributions of the binary DNN output in the three dilepton signal regions used in the fit: (a) SR-2ℓ-5j2b, (b) SR-2ℓ-6j1b, and (c) SR-2ℓ-6j2b. The $t\bar{t}Z$ signal strength and the $Z+b$ and $Z+c$ normalisations are considered as free parameters in the fit. Data-driven approach described in Section 6.1.1 is used to estimate $t\bar{t}$ background. The fitted values of signal strength, background normalisations and nuisance parameters have been applied to the MC templates in the plots. The shaded band corresponds to the total uncertainty (systematic and statistical) of the total SM prediction. The lower panel shows the ratio of the data to the SM prediction.

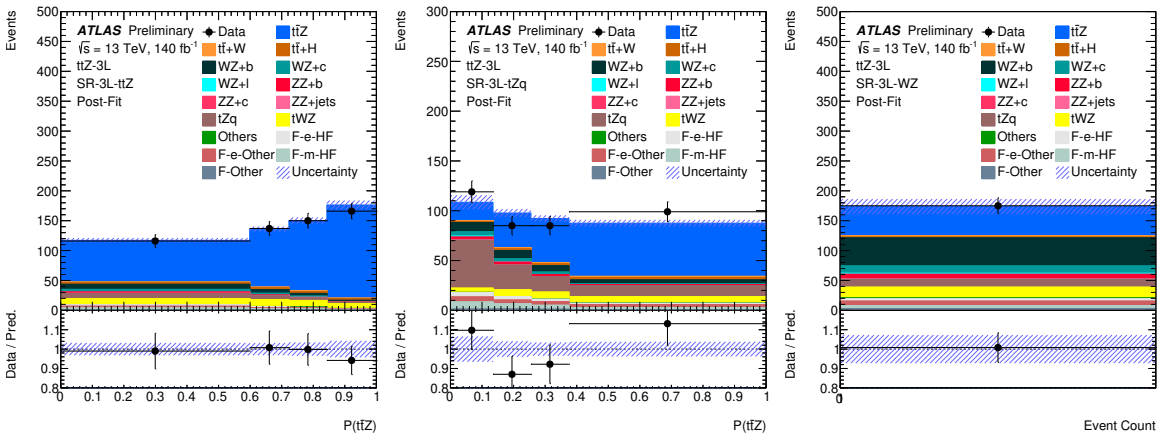

(a) (b) (c)

Figure 4: Distributions of the $t\bar{t}Z$-node of the multi-class DNN output and total event yield in the three trilepton signal regions used in the fit: (a) SR-3ℓ-ttZ, (b) SR-3ℓ-tZq, and (c) SR-3ℓ-WZ. The $t\bar{t}Z$ signal strength and the $WZ+b$ normalisation are considered as free parameters in the fit. The fitted values of signal strength, background normalisations and nuisance parameters have been applied to the MC templates in the plots. The shaded band corresponds to the total uncertainty (systematic and statistical) of the total SM prediction. The lower panel shows the ratio of the data to the SM prediction.

In the combined inclusive fit, all aforementioned signal and control regions are used, i.e.: 3 dilepton signal regions, 3 trilepton signal regions, 2 tetralepton signal regions, CR-4ℓ-ZZ and 3 fake lepton control regions. The fitted value of the inclusive cross section is found to be 0.86 ± 0.06 pb, in good agreement with the theory prediction [20] and with a relative precision of 6%. For comparison, the previous result [23]

Table 11: Post-fit event yields in the trilepton signal regions and the tetralepton signal and control regions, obtained for an integrated luminosity of 140 fb^{-1}. The values of the fitted parameters from the combined fit are used. The indicated errors include the Monte Carlo statistical uncertainty as well as all other systematic uncertainties discussed in Section 7. Because of rounding and correlations between systematic uncertainties, the values quoted for the total yield and its uncertainty may differ from the simple sum over all processes. A dash (—) indicates event yields smaller than 0.1.

	SR-3ℓ-ttZ	SR-3ℓ-WZ	SR-3ℓ-tZq	SR-4ℓ-SF	SR-4ℓ-DF	CR-4ℓ-ZZ
$t\bar{t}Z$	441 ± 21	49.0 ± 3.7	151 ± 11	49.4 ± 3.0	51.1 ± 2.9	2.36 ± 0.23
$t\bar{t}W$	4.3 ± 2.2	2.2 ± 1.1	5.3 ± 2.6	—	—	—
$t\bar{t}H$	11.9 ± 1.1	1.43 ± 0.13	6.70 ± 0.57	2.79 ± 0.24	2.82 ± 0.24	0.32 ± 0.04
$WZ + b$	21.1 ± 7.4	47 ± 16	27.1 ± 9.5	—	—	—
$WZ + c$	8.9 ± 3.6	12.2 ± 5.0	11.1 ± 4.6	—	—	—
$WZ + l$	1.19 ± 0.52	1.70 ± 0.76	1.81 ± 0.80	—	—	—
$ZZ + b$	4.3 ± 2.5	6.9 ± 4.0	7.3 ± 4.2	7.5 ± 2.0	0.46 ± 0.12	26.7 ± 6.9
$ZZ + c$	1.23 ± 0.42	1.22 ± 0.43	1.61 ± 0.53	2.13 ± 0.66	0.30 ± 0.09	24.6 ± 7.1
$ZZ + l$	0.42 ± 0.13	0.26 ± 0.09	0.53 ± 0.15	0.83 ± 0.24	0.34 ± 0.09	22.6 ± 5.2
tZq	20.8 ± 4.0	13.2 ± 2.3	99 ± 16	—	—	—
tWZ	40.0 ± 7.6	18.0 ± 4.2	24.2 ± 3.0	6.60 ± 0.82	7.3 ± 1.2	0.69 ± 0.10
$t\bar{t}t\bar{t}$	1.56 ± 0.78	0.13 ± 0.07	0.27 ± 0.14	—	—	—
Other	1.33 ± 0.61	1.40 ± 0.63	0.39 ± 0.19	0.55 ± 0.25	1.12 ± 0.52	0.55 ± 0.25
F-e-HF	4.6 ± 1.0	3.90 ± 0.87	12.0 ± 2.6	0.28 ± 0.07	0.45 ± 0.10	0.11 ± 0.03
F-e-Other	7.8 ± 2.7	7.3 ± 2.6	15.2 ± 5.4	0.39 ± 0.14	0.50 ± 0.18	0.10 ± 0.04
F-m-HF	6.98 ± 0.86	5.27 ± 0.66	18.2 ± 2.2	0.58 ± 0.07	0.62 ± 0.08	0.16 ± 0.02
F-Other	2.8 ± 1.2	2.7 ± 1.2	4.4 ± 2.0	0.90 ± 0.40	1.66 ± 0.74	0.33 ± 0.15
Total	580 ± 19	174 ± 13	386 ± 15	72.0 ± 3.4	66.7 ± 3.0	78.5 ± 8.0
Data	569	175	388	79	74	81

achieved a 10% uncertainty on the $t\bar{t}Z$ cross section, using the same dataset. All free floating background normalizations are consistent with the SM predictions within their uncertainties. The breakdown of the combination per channel can be found in Table 13. A mild upwards fluctuation in the data is observed in the 4ℓ channel. The compatibility (p-value) of the cross section measured in the combination and the values fitted individually is 53 %, signalling good agreement between the different analysis channels. The values of the background normalisation factors obtained from the inclusive cross section fit can be found in the Table 12. A deviation from unity is observed only for $\mathcal{N}_{Z+c}$, which compensates for the mismodelling of the Z+c background in SR-2ℓ-6j1b region. All other normalisation factors are consistent with their respective SM predictions. No significant pulls or constraints are observed in the fit, except for the CKKW and QSF scales of the Z+b background, which are pulled by $\approx 1\sigma$. These pulls are caused by the mismodelling of the Z+jets background in the SR-2ℓ-5j2b and SR-2ℓ-6j1b signal regions. The impact of systematic uncertainties on the result is listed in Table 14. The dominant systematic uncertainties are background normalisations and detector systematics related to jets and missing transverse energy.

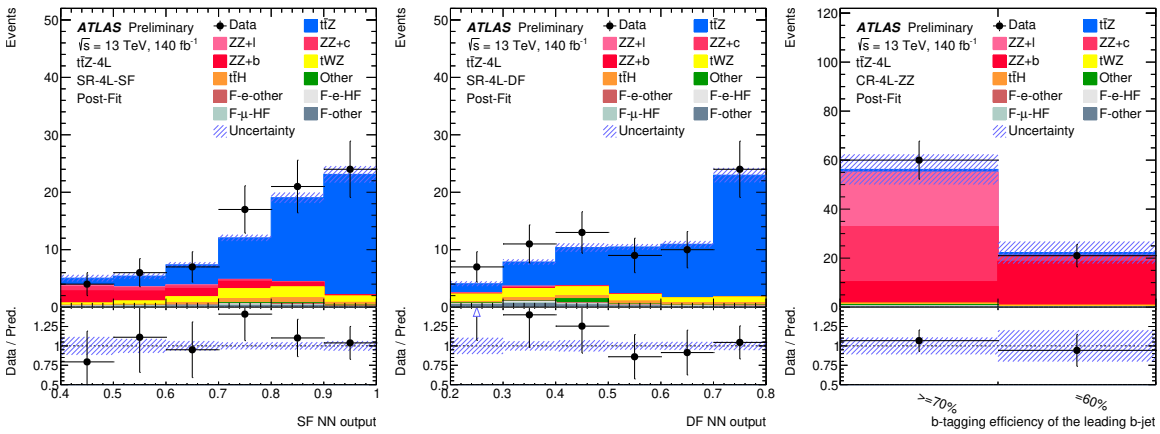

(a) (b) (c)

Figure 5: Distributions of the binary DNN outputs in the two tetralepton signal regions used in the fit: (a) SR-4ℓ-SF, (b) SR-4ℓ-DF; as well as (c) of the b-tagging efficiency of the leading b-tagged jet in the control region CR-4ℓ-ZZ. The $t\bar{t}Z$ signal strength and the $ZZ + b$ normalisation, $\mathcal{N}_{ZZ+b}$, are considered as free parameters in the fit. The fitted values of signal strength, background normalisations and nuisance parameters have been applied to the MC templates in the plots. The shaded band corresponds to the total uncertainty (systematic and statistical) of the total SM prediction. The lower panel shows the ratio of the data to the SM prediction.

Table 12: Values of background normalisation factors measured in the combined inclusive fit.

Norm. factor	Value
$\mathcal{N}_{ZZ+b}$	$1.1^{+0.4}_{-0.4}$
$\mathcal{N}_{WZ+b}$	$0.9^{+0.4}_{-0.4}$
$\mathcal{N}_{Z+b}$	$1.08^{+0.11}_{-0.10}$
$\mathcal{N}_{Z+c}$	$0.61^{+0.23}_{-0.20}$
$\mathcal{N}_{e,\mathrm{HF}}$	$0.89^{+0.09}_{-0.09}$
$\mathcal{N}_{e,\mathrm{other}}$	$1.2^{+0.4}_{-0.4}$
$\mathcal{N}_{\mu,\mathrm{HF}}$	$1.02^{+0.08}_{-0.08}$

Table 13: Measured $t\bar{t}Z$ cross sections obtained from the fits in the signal regions with different lepton multiplicities and corrected to parton-level. The uncertainties include statistical and systematic sources.

Channel	$\sigma_{t\bar{t}Z}$
Dilepton	0.84 ± 0.11 pb $= 0.84 \pm 0.06$ (stat.) ± 0.09 (syst.) pb
Trilepton	0.84 ± 0.07 pb $= 0.84 \pm 0.05$ (stat.) ± 0.05 (syst.) pb
Tetralepton	$0.97^{+0.13}_{-0.12}$ pb $= 0.97 \pm 0.11$ (stat.) ± 0.05 (syst.) pb
Combination ($2\ell, 3\ell$ & 4ℓ)	0.86 ± 0.06 pb $= 0.86 \pm 0.04$ (stat.) ± 0.04 (syst.) pb

Table 14: Grouped impact of systematic uncertainties in the combined inclusive fit to data. The uncertainties are symmetrised for presentation and grouped into the categories described in the text. The quadrature sum of the individual uncertainties is not equal to the total uncertainty due to correlations introduced by the fit.

Uncertainty Category	$\Delta\sigma_{t\bar{t}Z}/\sigma_{t\bar{t}Z}$ [%]
Background normalisations	2.0
Jets and $E_{\mathrm{T}}^{\mathrm{miss}}$	1.9
b-tagging	1.7
$t\bar{t}Z$ μ_F and μ_R scales	1.6
Leptons	1.6
Z +jets modelling	1.5
tWZ modelling	1.1
$t\bar{t}Z$ showering	1.0
$t\bar{t}Z$ A14	1.0
Luminosity	1.0
Diboson modelling	0.8
tZq modelling	0.7
PDF (signal & backgrounds)	0.6
MC statistical	0.5
Other backgrounds	0.5
Fake leptons	0.4
Pile-up	0.3
Data-driven $t\bar{t}$	0.1

9 Unfolding and differential cross section measurements

The differential measurement is performed in the 3ℓ and 4ℓ channels, using definitions of the fiducial volumes described in Section 5.4. The dilepton channel is not used because of its high background contamination. A profile-likelihood unfolding method is used, which is described in Section 9.1. The observables that are unfolded and their binning are listed in Section 9.2, and the results presented in Section 9.3.

9.1 Profile likelihood unfolding procedure

The profile likelihood unfolding procedure uses the following formula for the likelihood

$$L\left(\vec{n}|\mu,\vec{\theta},\vec{k}\right) = \prod_{r\in\text{regions}}\prod_{i\in\text{bins}} \text{Pois}\left(n_{i,r}|\vec{\mu}\vec{S}_{i,r}(\vec{\theta}) + B_{i,r}(\vec{\theta},\vec{k})\right) \times \prod_{j\in\text{NPs}} \text{Gaus}\left(\theta_j\right) \times R(\vec{\mu}), \tag{2}$$

where $n_{i,r}$ is the number of events observed in i-th bin of r-th region, $\vec{S}_{i,r}$ is the response matrix, $B_{i,r}(\vec{\theta},\vec{k})$ is the background contribution, $\vec{k}$ is vector of free-floating background normalisations and $\vec{\theta}$ is vector of nuisance parameters related to the systematic uncertainties. In case of the normalised distribution, the $\vec{\mu}$ is reparametrised in the way, that the last element of the vector is the overall signal normalisation. In this case, the content of the last bin of the unfolded distribution is dropped from the $\vec{\mu}$, since it is no longer a free parameter and it can be calculated based on the values in other bins and the overall normalisation.

This likelihood is similar to the likelihood used in the inclusive measurement, but there are two important modifications. While a single signal strength μ is used in the inclusive measurement, in the differential measurement, it is replaced by a vector of signal strengths, $\vec{\mu}$, where each element of the vector corresponds to a signal strength in a given bin of the unfolded distribution. The other difference with respect to the inclusive cross section likelihood is the regularisation term $R(\vec{\mu})$, however it is used only for a subset of the unfolded variables as summarised in Table 15. Discrete second derivative regularisation, also known as Tikhonov's regularisation [105–108], is used with the regularisation term given by the following formula:

$$R(\vec{\mu}) = \exp\left[-\frac{\tau^2}{2}\sum_{i=2}^{i+1<N_{bins}}\left((\mu_i - \mu_{i-1}) - (\mu_{i+1} - \mu_i)\right)^2\right], \tag{3}$$

where the sum runs over the bins of the unfolded distribution and τ is the regularisation parameter. The values of τ are summarised in Table 15, they depend on the variable and may differ between particle and parton levels.

The aim of the regularisation is to suppress strong anti-correlations between the bins of the unfolded distribution, arising from migrations between the bins. Higher values of the regularisation parameter τ lead to lower uncertainties. However, too strong regularisation can lead to biased results and turns anti-correlations between the neighbouring bins into correlations. In order to find a compromise between these two effects, the τ values have been scanned with a step 0.1, starting from 0. For each τ, the unfolding

on the Asimov dataset[11] has been performed and the global correlation factor ρ defined in Equation 4 has been evaluated:

$$\rho = \left\langle \sqrt{1 - (C_{ii} C_{ii}^{-1})^{-1}} \right\rangle, \tag{4}$$

where C_{ii} is the correlation matrix, C_{ii}^{-1} is inverted correlation matrix and the brackets represent the mean value over the diagonal elements. The τ value where the global correlation reaches its minimum was chosen as the optimal value.

In order to validate the ability of the unfolding to recover an alternative truth-level distribution a number of stress tests are performed. Motivated by the potential impact of EFT effects on the high-p_{T} tail of the p_{T}^{Z} distribution, this observable is linearly reweighted, with slopes ranging from 0.75 to 2.00 between 0 and 1 TeV. The corresponding event-wise correction, which is 1.0 at $p_{\mathrm{T}}^{Z} = 0$ TeV and ranges from 0.75 to 2.0 at $p_{\mathrm{T}}^{Z} = 1$ TeV, is used to reweight all of the other observables in this EFT-like stress test. Additionally, data-driven stress tests are performed where the histogram of the ratio between observed and expected signal in the unfolded variable at detector level is fitted by a quadratic function and the value of the function is then used to apply the weight. Another kind of stress test uses a histogram of the ratio of observed and expected signal as a function of H_{T}^{ℓ}, which was found to be the variable with the worst modelling (lowest p-value at detector-level), where the value of the ratio is used to apply the weight. All the stress tests show good ability of the unfolding to recover an alternative distribution, with average χ^2/n.d.f. well below 0.05.

9.2 Differential observables

The choice of the unfolded observables was optimised based on their physics importance and sensitivity to EFT operators. The list of the observables used in the differential measurement can be found in the Table 15.

The observables are either unfolded in one of the channels, or in their combination, taken as the union of the fiducial volumes defined in Section 5.4. The observables relying on a particular decay mode of the $t\bar{t}$ system are unfolded only in the corresponding channel. Two observables were unfolded separately in both channels, as their distributions are expected to differ among the channels: N_{jets} and H_{T}^{ℓ}. The observables not requiring a particular decay of the $t\bar{t}$ system are unfolded in the combination of the 3ℓ and 4ℓ channels. All the variables are unfolded to both particle and parton level, except for the N_{jets}, which is unfolded only to particle level. For observables requiring hadronic top reconstruction the migration matrices are somewhat non-diagonal (~40-70% on diagonal compared to purely leptonic observables with >90% on the diagonal). In these cases unregularised unfolding would yield large fluctuations. Therefore, Tikhonov regularisation is applied for these observables.

The binning for all the observables is summarised in Table 25. The binning is optimised, starting from the requirement that the statistical uncertainty in all unfolded bins be lower than 35 % for variables unfolded in the 4ℓ channel only, and lower than 25 % for the 3ℓ and 3ℓ+4ℓ variables, Furthermore, diagonal elements of the migration matrix (MM) must be higher than a chosen threshold (starting from a high value and iteratively decreasing it). The range of the first bin of the distribution is chosen at the lowest possible

[11] Asimov dataset means fitting Monte Carlo with the same Monte Carlo templates

Table 15: Summary of the variables used for the differential measurement and the value of the regularisation parameter τ for both particle and parton level for the relevant variables.

	Variable	Regularisation	τ^{particle}	τ^{parton}	Definition
$3\ell + 4\ell$	p_{T}^{Z}	No	-	-	Transverse momentum of the Z boson
	$\lvert y^{Z} \rvert$	No	-	-	Absolute rapidity of the Z boson
	$\cos\theta_{Z}^{*}$	No	-	-	Angle between the direction of the Z boson in the detector reference frame and the direction of the negatively charged lepton in the rest frame of the Z boson
	p_{T}^{t}	Yes	1.5	1.4	Transverse momentum of the top quark
	$p_{\text{T}}^{t\bar{t}}$	Yes	1.6	1.5	Transverse momentum of the $t\bar{t}$ system
	$\lvert\Delta\phi(t\bar{t}, Z)\rvert$	Yes	2.4	2.1	Absolute azimuthal separation between the Z boson and the $t\bar{t}$ system
	$m^{t\bar{t}Z}$	Yes	1.5	1.6	Invariant mass of the $t\bar{t}Z$ system
	$m^{t\bar{t}}$	Yes	1.5	1.4	Invariant mass of the $t\bar{t}$ system
	$\lvert y^{t\bar{t}Z} \rvert$	Yes	1.5	1.5	Absolute rapidity of the $t\bar{t}Z$ system
3ℓ	H_{T}^{ℓ}	No	-	-	Sum of the transverse momenta of all the signal leptons
	$\lvert\Delta\phi(Z, t_{\text{lep}})\rvert$	No	-	-	Absolute azimuthal separation between the Z boson and the top (anti-top) quark featuring the $W \to \ell\nu$ decay
	$\lvert\Delta y(Z, t_{\text{lep}})\rvert$	No	-	-	Absolute rapidity difference between the Z boson and the top (anti-top) quark featuring the $W \to \ell\nu$ decay
	$p_{\text{T}}^{\ell,\text{non}-Z}$	No	-	-	Transverse momentum of the lepton which is not associated with the Z boson
	N_{jets}	No	-	-	Number of selected jets with $p_{\text{T}} > 25\,\text{GeV}$ and $\lvert\eta\rvert < 2.5$
4ℓ	H_{T}^{ℓ}	No	-	-	Sum of the transverse momenta of all the signal leptons
	$\lvert\Delta\phi(\ell_{t}^{+}, \ell_{\bar{t}}^{-})\rvert$	No	-	-	Absolute azimuthal separation between the two leptons from the $t\bar{t}$ system
	N_{jets}	No	-	-	Number of selected jets with $p_{\text{T}} > 25\,\text{GeV}$ and $\lvert\eta\rvert < 2.5$

value where these two requirements are satisfied (narrow bins lead to high migrations and high statistical uncertainties, widening the bin decreases the uncertainty and increases diagonal elements of the migration matrix). When the range of the first bin is found, the next bin is optimised. For the given two requirements, only a limited number of bins can be found. The requirement on the minimal value of MM diagonal elements is gradually decreased to obtain binning for a higher number of bins. The binning is optimised for a number of bins ranging from 2 to 10, using only the predicted statistical uncertainties and unfolding to particle-level. Then stress tests are performed for each choice of binning: the one with the largest number of bins that still passes all stress tests is selected. The same binning is used for both particle- and parton-level.

9.3 Unfolded cross section measurements

The full set of unfolded results for the transverse momentum of the Z boson are presented in this section. For brevity, only the absolute differential cross sections unfolded to particle-level are shown for other

observables. All other differential results (including normalised distributions, and unfolding to parton-level) are available in the Appendix.

Figure 6 shows the distribution of detector-level p_{T}^{Z} in 3ℓ signal regions, as well as migration matrices, acceptance and efficiency corrections. The acceptance is the ratio of the signal at the given bin of the detector-level distribution which passes the truth-level fiducial volume cuts. The efficiency is defined as the fraction of the events from a given bin of the truth-level distribution passing the selection in the given detector-level region. Figure 7 shows similar plots for 4ℓ signal regions. The unfolded distributions, nominal truth-level MC prediction, as well as alternative generator predictions are shown in Figure 8. The uncertainties of the unfolded distributions range approximately from 15% to 40%. In general, low uncertainties are observed for the variables which are reconstructed from leptons only and unfolded in the combination of both channels. Large number of data events and low migrations between the bins lead to the low uncertainties. On the other hand, the variables unfolded only in the 4ℓ channel suffer from low number of events, which causes relatively high statistical uncertainties. The unfolding to the particle level has lower uncertainties compared to parton-level, because of the more diagonal migration matrices, and normalised unfolded distributions are also more precise than the absolute distributions, because of a significant reduction of the normalisation effect of the uncertainties. The dominant source of the uncertainty is the statistical uncertainty of data in all distributions and bins. The effect of the systematic uncertainties is significantly lower than the effect of the statistical uncertainty.

The compatibility between the unfolded distributions and the predictions have been evaluated using χ^2 (which is calculated from the uncertainties of the unfolded distribution and their correlations), and the corresponding p-values, which can be found in Table 26 for absolute unfolded distributions and in Table 27 for normalised distributions. The p-values show a good agreement between the unfolded data and the prediction for most of the variables. The lowest p-values, around 2%, are observed for H_{T}^{ℓ}, this was expected since this variable has the worst modelling (lowest p-values) also at the detector-level.

The absolute differential cross sections unfolded to particle-level for observables defined in the 3ℓ and 4ℓ channels separately are shown in Figures 9 and 10, while Figures 11 and 12 present those defined in the combination of the two channels. All other results are available in the Appendix: Figures 16 and 17 for the unregularised observables in the combination of the 3ℓ and 4ℓ channels, Figures 18-23 for the regularised ones, Figures 24-28 for those defined in the 3ℓ channel only, and Figures 29-31 for those defined in the 4ℓ channel only.

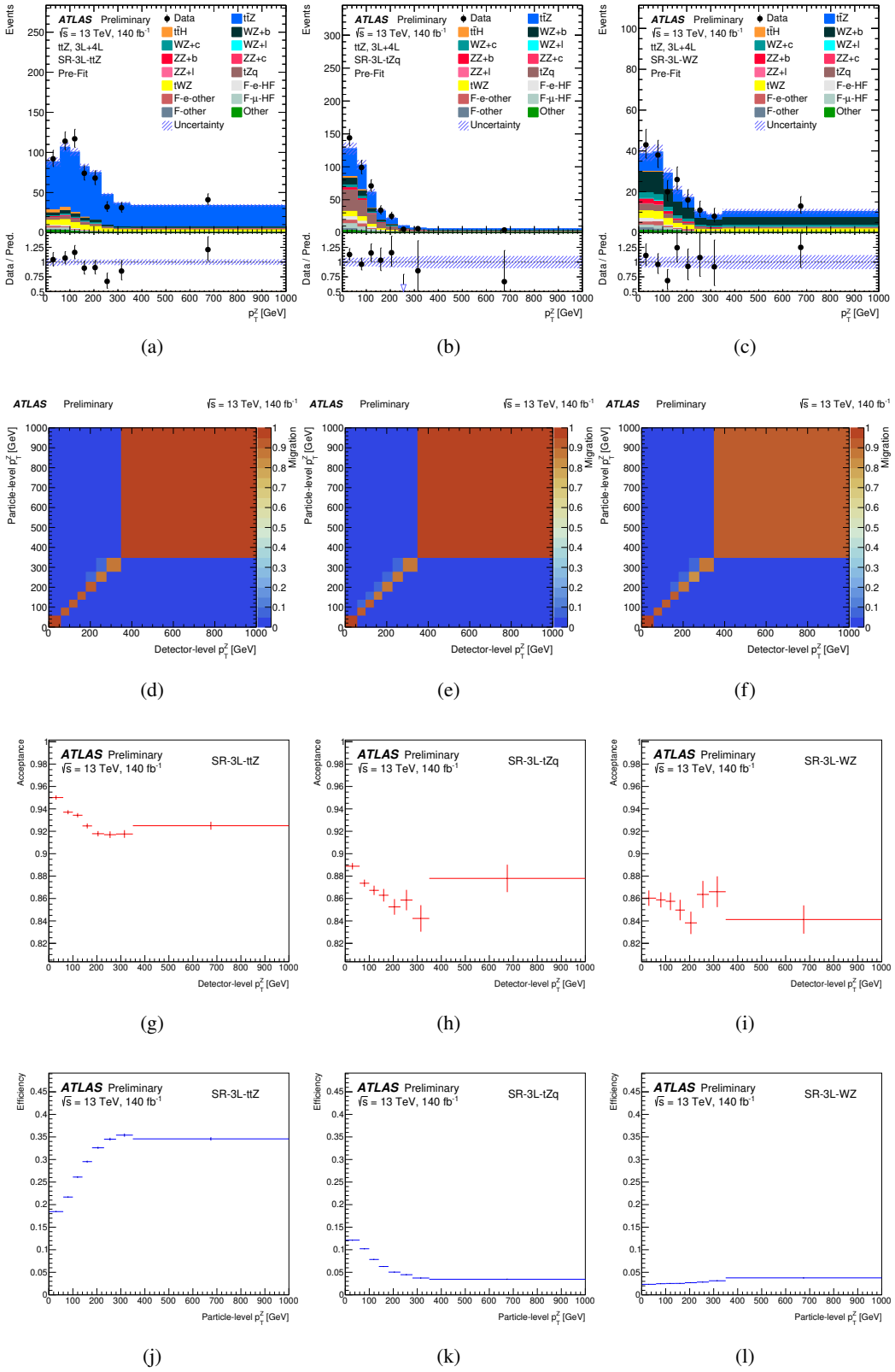

Figure 6: Detector-level distributions (top), together with migration matrices (second row) and acceptance (third row) and efficiency (bottom) histograms for the p_{T}^{Z} observable in the trilepton channel regions: SR-3ℓ-ttZ (left), SR-3ℓ-tZq (center) and SR-3ℓ-WZ (right).

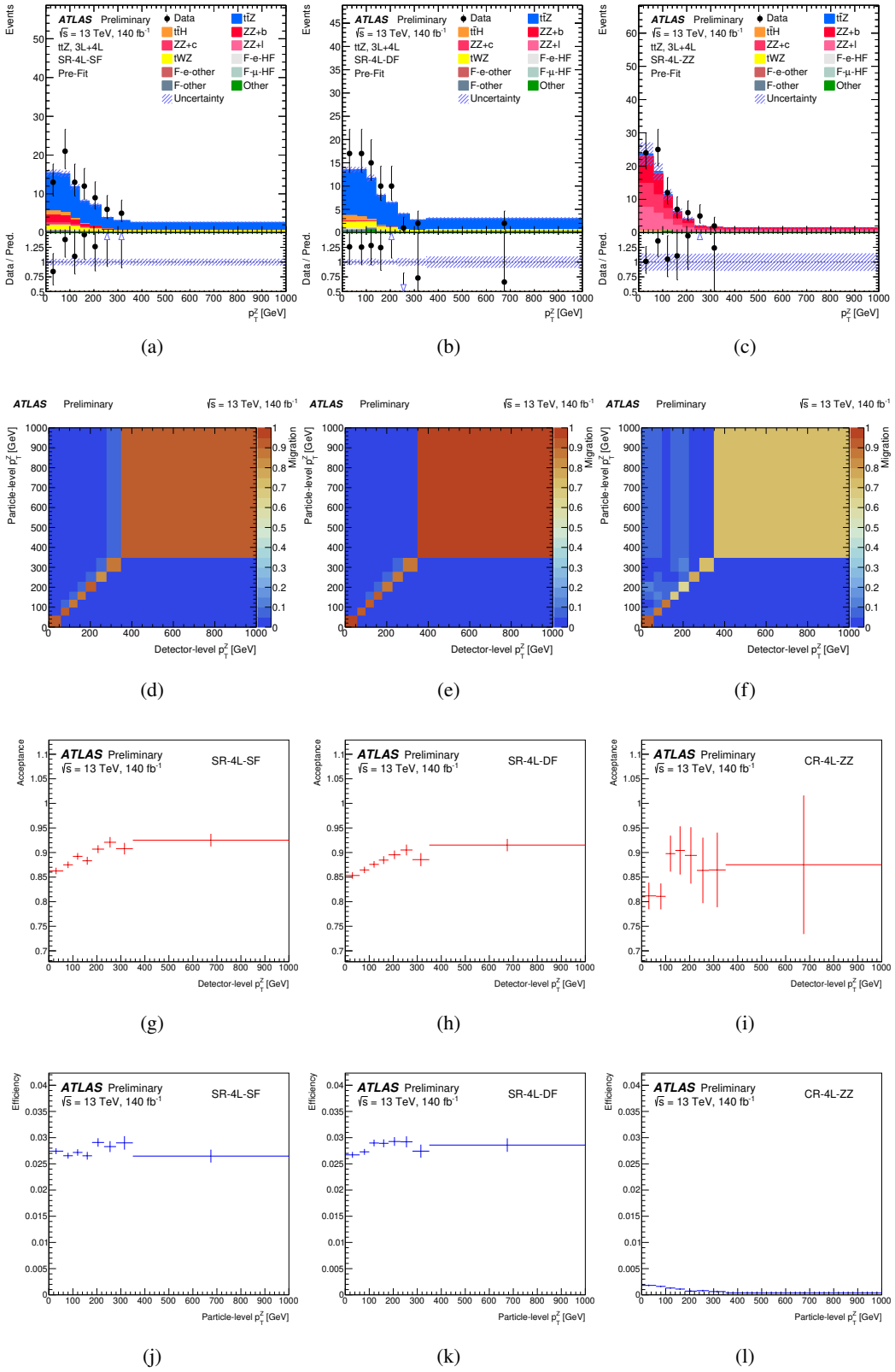

(a) (b) (c)

(d) (e) (f)

(g) (h) (i)

(j) (k) (l)

Figure 7: Detector-level distributions (top), together with migration matrices (second row) and acceptance (third row) and efficiency (bottom) histograms for the p_{T}^{Z} observable in the tetralepton channel regions: SR-4ℓ-SF (left), SR-4ℓ-DF (center) and CR-4ℓ-ZZ (right). Migration matrices and corrections apply to the particle level.

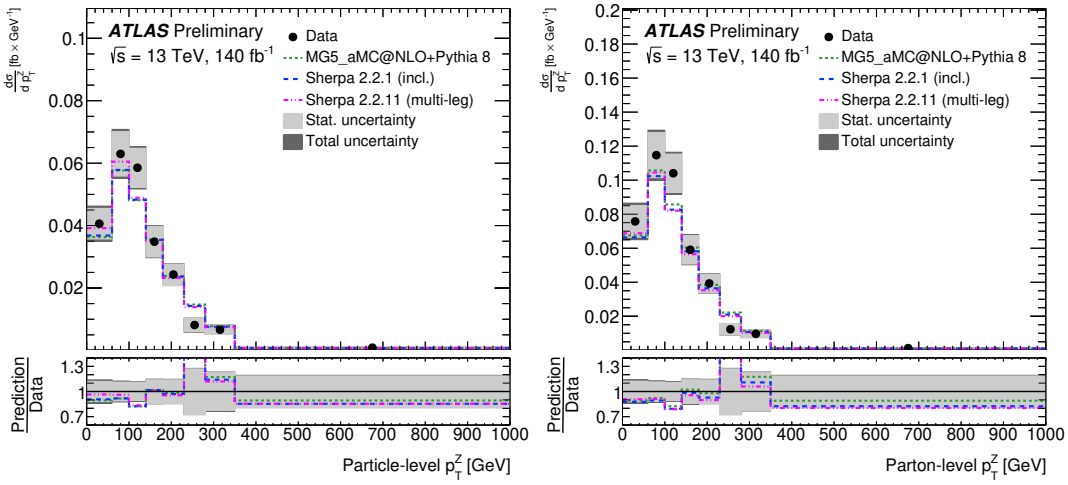

(a) (b)

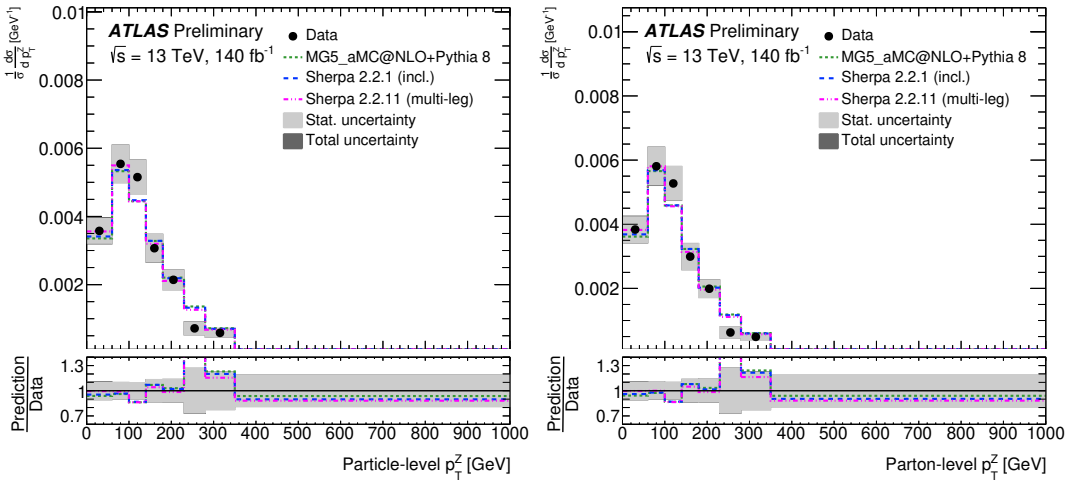

(c) (d)

Figure 8: Cross section measurement as a function of the p_{T}^{Z} observable in the combination of the 3ℓ and 4ℓ channels, absolute (top) and normalised (bottom), unfolded to particle level (left) and parton level (right). The dark grey band corresponds to the total uncertainty on the measurement; in some cases, it is almost fully covered by the light grey band, representing the dominating statistical uncertainty. Alternative generator predictions are overlaid as solid coloured lines.

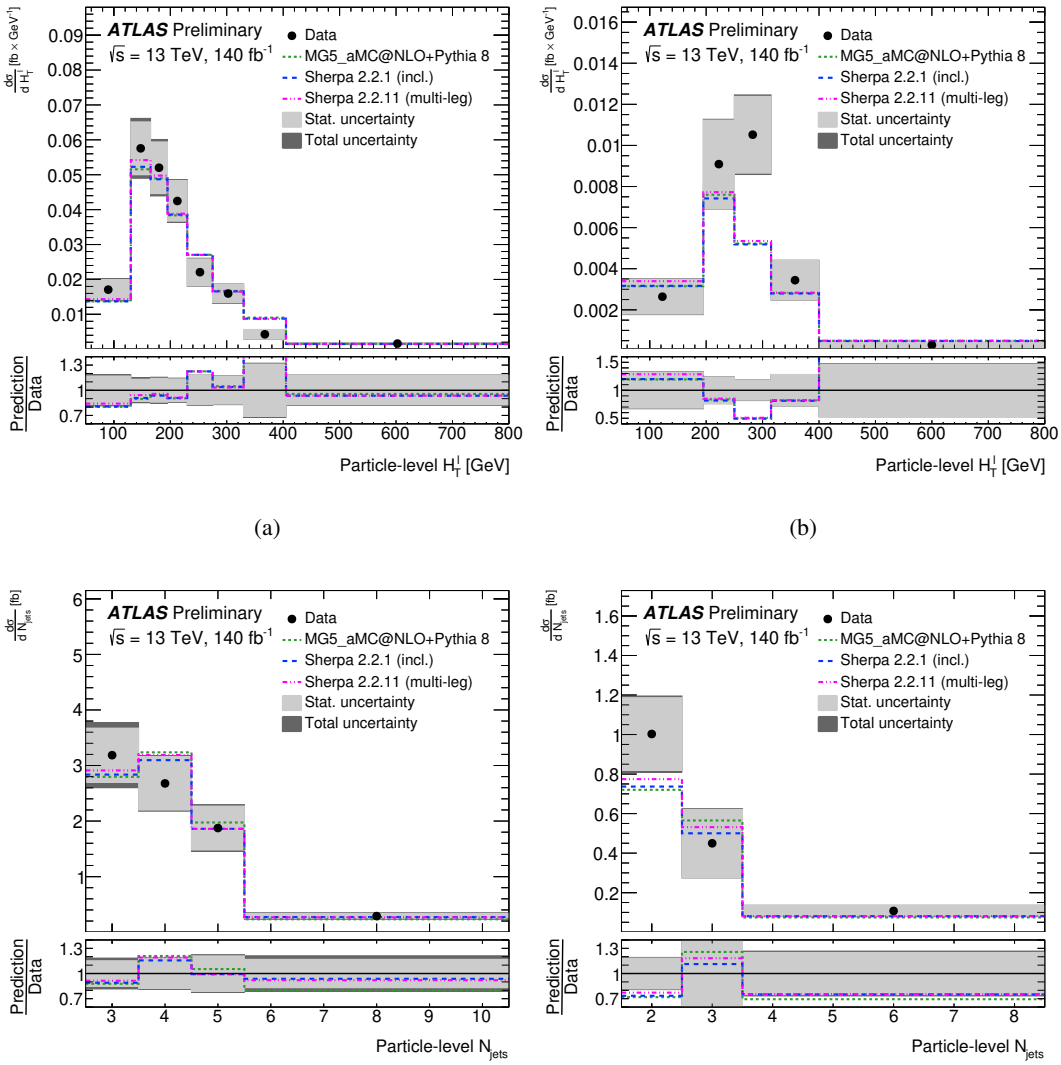

Figure 9: Absolute differential cross section measurements unfolded to particle-level of: $H_{\mathrm{T}}^{\mathrm{leptons}}$ in the (a) 3ℓ and (b) 4ℓ channels, N_{jets} in the (c) 3ℓ and (d) 4ℓ channels. The dark grey band corresponds to the total uncertainty on the measurement; in some cases, it is almost fully covered by the light grey band, representing the dominating statistical uncertainty. Alternative generator predictions are overlaid as solid coloured lines.

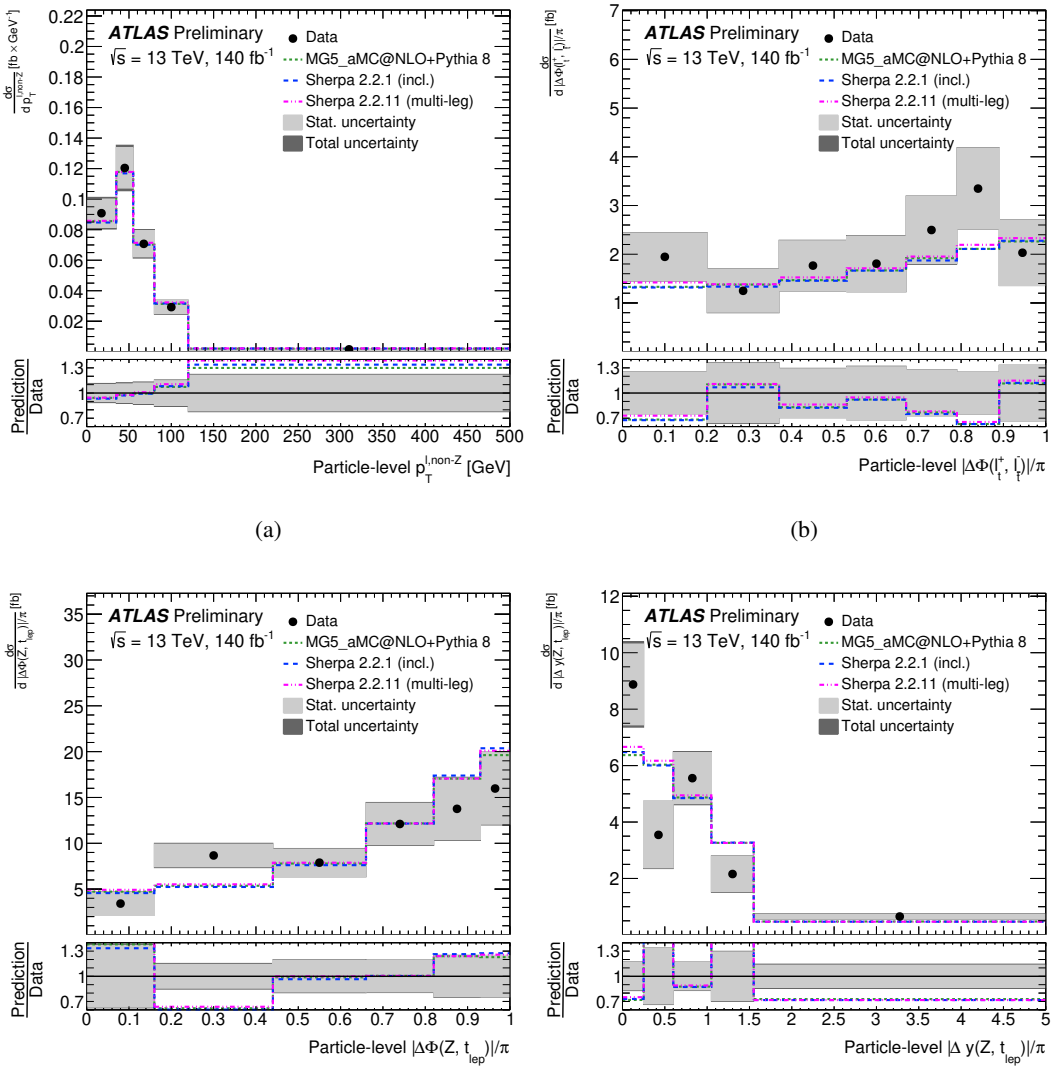

Figure 10: Absolute differential cross section measurements unfolded to particle-level of: (a) $p_{\mathrm{T}}^{\ell,\mathrm{non-}Z}$ in the 3ℓ channel, (b) $|\Delta\phi(\ell_t^+, \ell_{\bar{t}}^-)|$ in the 4ℓ channel, (c) $|\Delta\phi(Z, t_{\mathrm{lep}})|/\pi$ and (d) $|\Delta y(Z, t_{\mathrm{lep}})|$ in the 3ℓ channel. The dark grey band corresponds to the total uncertainty on the measurement; in some cases, it is almost fully covered by the light grey band, representing the dominating statistical uncertainty. Alternative generator predictions are overlaid as solid coloured lines.

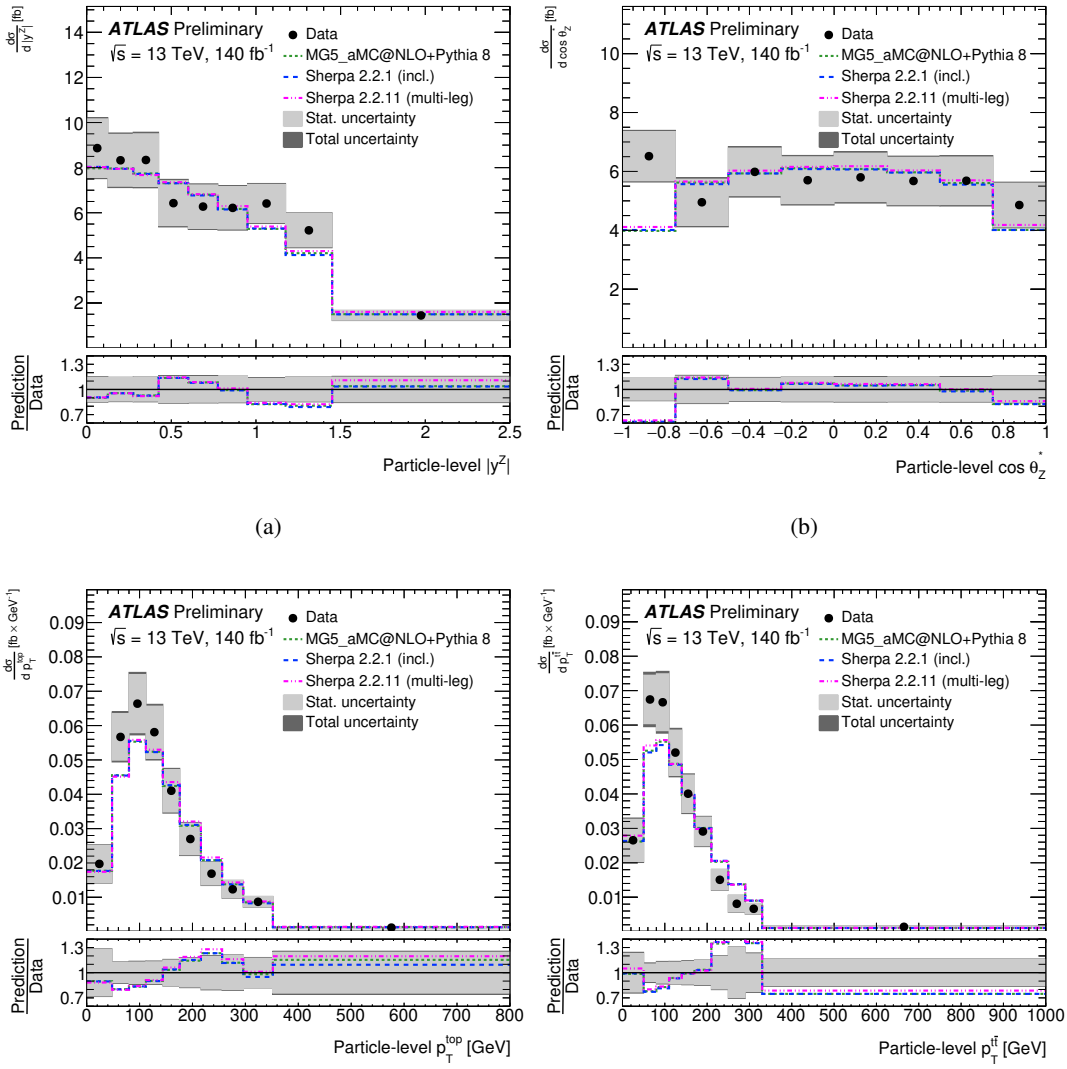

Figure 11: Absolute differential cross section measurements unfolded to particle-level in the combination of the 3ℓ and 4ℓ channels of: (a) $|y^Z|$, (b) $\cos\theta^*_Z$, (c) p^t_{T}, and (d) $p^{t\bar{t}}_{\mathrm{T}}$. The dark grey band corresponds to the total uncertainty on the measurement; in some cases, it is almost fully covered by the light grey band, representing the dominating statistical uncertainty. Alternative generator predictions are overlaid as solid coloured lines.

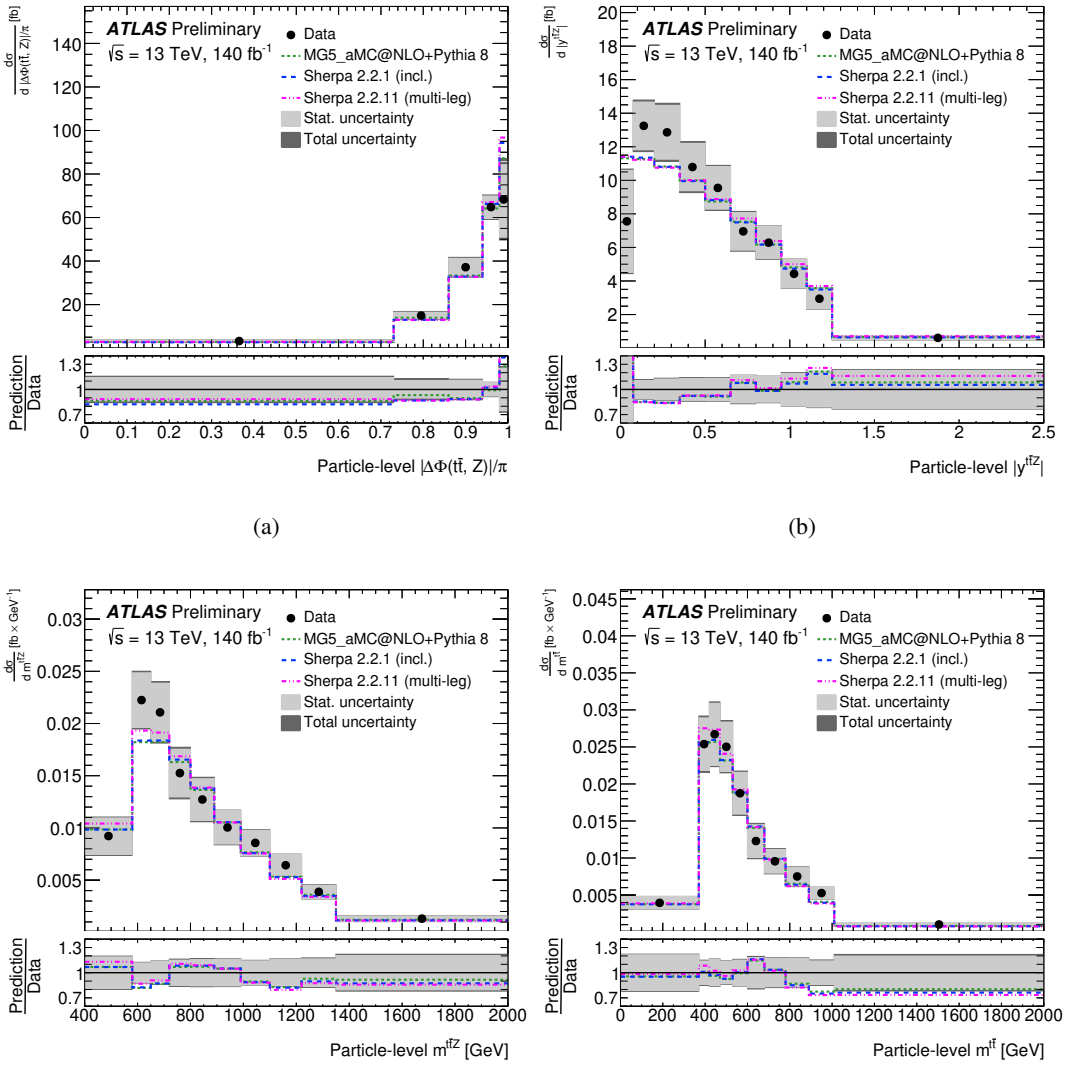

(a) (b)

(c) (d)

Figure 12: Absolute differential cross section measurements unfolded to particle-level in the combination of the 3ℓ and 4ℓ channels of: (a) $|\Delta\phi(t\bar{t}, Z)|/\pi$, (b) $|y^{t\bar{t}Z}|$, (c) $m^{t\bar{t}Z}$, and (d) $m^{t\bar{t}}$. The dark grey band corresponds to the total uncertainty on the measurement; in some cases, it is almost fully covered by the light grey band, representing the dominating statistical uncertainty. Alternative generator predictions are overlaid as solid coloured lines.

10 Spin correlations interpretation

The first search for top quark spin correlations in $t\bar{t}Z$ events is presented, using detector-level distributions. Following the work of Ref. [26], the helicity (k), transverse (n) and r-axes in the $t\bar{t}$ rest frame are defined, and the polar angle of the charged lepton or down-type quark from the (anti-)top decay with respect to one of these axes, in the rest frame of its parent (anti-)top, is considered as a measure of (anti-)top polarisations and $t\bar{t}$ spin correlations. Six independent observables can thus be defined:

$$\cos\theta_k^+, \quad \cos\theta_k^-, \quad \cos\theta_n^+, \quad \cos\theta_n^-, \quad \cos\theta_r^+, \quad \cos\theta_r^-, \tag{5}$$

where the ± superscript indicates the sign of the charge of the lepton/quark. As shown in Ref. [26], the coefficients of the spin density matrix can be extracted from the averages of the angular distributions corresponding to the observables listed in (5). These relations are summarised in Table 16; the c_{ii} components are hereafter referred to as "spin correlations", the $c_{ij}(i \neq j)$ and c_i components as "spin cross-correlations", and the $b_i^{\pm}$ components as "polarisations". The $t\bar{t}Z$ process, differing from $t\bar{t}$ production not only by the emission of an additional Z boson but also by different fractions of $q\bar{q}$- and qg-initiated Feynman diagrams, leads to a different picture of top quark spin correlations: the three coefficients c_{rr}, c_{kk} and c_{nn} adopt negative values and different magnitudes as in the $t\bar{t}$ case, and a small longitudinal polarisation is induced by the emission of the Z boson, resulting in non-zero $b_r^{\pm}$ and $b_k^{\pm}$ coefficients [26]. Future measurements of the full spin density matrix in $t\bar{t}Z$ production will be able to probe possible CP-violation effects and four-fermion interactions with complementary sensitivity to $t\bar{t}$ production [109].

Table 16: Coefficients of the spin density matrix and their expressions as averages of angular distributions.

Coefficient	Expression
c_{rr}	$-9\langle\cos\theta_r^+ \cdot \cos\theta_r^-\rangle$
c_{kk}	$-9\langle\cos\theta_k^+ \cdot \cos\theta_k^-\rangle$
c_{nn}	$-9\langle\cos\theta_n^+ \cdot \cos\theta_n^-\rangle$
c_{rk}	$-9\langle\cos\theta_r^+ \cdot \cos\theta_k^- + \cos\theta_r^- \cdot \cos\theta_k^+\rangle$
c_{kn}	$-9\langle\cos\theta_k^+ \cdot \cos\theta_n^- + \cos\theta_k^- \cdot \cos\theta_n^+\rangle$
c_{rn}	$-9\langle\cos\theta_r^+ \cdot \cos\theta_n^- + \cos\theta_r^- \cdot \cos\theta_n^+\rangle$
c_r	$-9\langle\cos\theta_k^+ \cdot \cos\theta_n^- - \cos\theta_k^- \cdot \cos\theta_n^+\rangle$
c_k	$-9\langle\cos\theta_n^+ \cdot \cos\theta_r^- - \cos\theta_n^- \cdot \cos\theta_r^+\rangle$
c_n	$-9\langle\cos\theta_r^+ \cdot \cos\theta_k^- - \cos\theta_r^- \cdot \cos\theta_k^+\rangle$
b_r^+	$3\langle\cos\theta_r^+\rangle$
b_r^-	$3\langle\cos\theta_r^-\rangle$
b_k^+	$3\langle\cos\theta_k^+\rangle$
b_k^-	$3\langle\cos\theta_k^-\rangle$
b_n^+	$3\langle\cos\theta_n^+\rangle$
b_n^-	$3\langle\cos\theta_n^-\rangle$

In the 4ℓ channel, all these observables can be defined in terms of leptons from the $t\bar{t}$ system, while in the 3ℓ channel only one lepton is available which can be used to the define the polarisation observables. In order to access the spin correlations in semi-leptonic $t\bar{t}$ events, the down-type quark from the hadronic W boson decay must be used. Relying on the $\sim 50\%$ branching ratio of the hadronic W boson into $c\bar{s}/\bar{c}s$, s-candidates are selected by applying a simultaneous b-tag and b-veto to the jets selected by the top reconstruction algorithm as belonging to that W boson: if the jet is tagged at least at the 85% WP but not

at the 60% WP, it is considered to be c-tagged, and its companion W-jet is the resulting s-jet. 3ℓ events where the s-jet cannot be identified in this way are rejected.

A final observable of interest can be constructed in both the 3ℓ and 4ℓ channels: the opening angle between the two charged leptons (charged lepton and s-jet) from the dileptonic (semi-leptonic) $t\bar{t}$ system, where each decay product is first boosted to the rest frame of its respective parent (anti-)top quark. This angle φ is particularly sensitive to spin correlations, and the following three relations hold [26]:

$$\frac{1}{\sigma}\frac{\mathrm{d}\sigma}{\mathrm{d}\cos\varphi} = \frac{1}{2}\left(1 - D\cos\varphi\right), \quad D = -\frac{c_{rr} + c_{kk} + c_{nn}}{3}, \quad D = -3\langle\cos\varphi\rangle. \tag{6}$$

Since the angular observables listed in Table 16 suffer from low statistics in the 4ℓ channel and in general highly non-diagonal migration matrices (since all the observables rely on the precise reconstruction of the top quarks), unfolding these distributions using the profile-likelihood method defined in Section 9 is not possible without large amounts of regularisation. Instead, a detector-level template fit is preferred, comparing two "spin scenarios":

$$O = f_{\mathrm{SM}} \cdot O_{\text{spin-on}} + (1 - f_{\mathrm{SM}}) \cdot O_{\text{spin-off}}. \tag{7}$$

Each observable O (the 15 coefficients of the spin density matrix and the $\cos\varphi$ distribution) is thus fitted to a linear combination of a SM-like template (taken from the nominal $t\bar{t}Z$ MC predictions) and to its predicted values in the absence of any spin correlation or top polarisation. The latter predictions are identically 0 for all spin coefficients, and therefore lead to a flat distribution of the $\cos\varphi$ observable. These "spin-off" predictions at parton-level are forward-folded through a migration matrix built from the nominal MC samples to produce corresponding detector-level templates, and are assigned the same uncertainties as the nominal templates. The single parameter of interest f_{SM} is 0 in the absence of spin correlations and 1 in case of perfect agreement of the unfolded data with the SM.

Since some parameters of the $t\bar{t}Z$ spin correlation matrix are zero within theoretical uncertainties [26] they are not considered in order to improve the stability of the combined fit. The only coefficients to be significantly non-zero in the SM are the three spin correlations (c_{rr}, c_{kk} and c_{nn}), one of the cross-correlations (c_{rk}), four of the polarisations ($b_r^{\pm}$ and $b_k^{\pm}$), as well as D. Each observable is defined and measured in the combination of the 3ℓ and 4ℓ channels. The strategy outlined above results in the extraction of 9 different values of f_{SM} at detector-level, which are then combined in a profiled χ^2-fit. The fit fully takes into account the statistical overlap in the data, as well as the correlations between the NPs from the different measurements of f_{SM}.

The expected and observed values of f_{SM} for each individual detector-level template fit to a single angular distribution are given in Table 17. For each individual measurement it is checked that the fit does not exhibit any strong pull or constraint of the nuisance parameters, compared to the inclusive cross section measurement presented in Section 8, and the values are found to be consistent with the SM within uncertainties.

Using the covariance matrices, impacts and correlations of all NPs from each fit, these extracted values of f_{SM} are combined following the statistical prescriptions described above, and yield:

$$f_{\mathrm{SM}}^{\text{obs.}} = 1.20 \pm 0.63\ (\text{stat.}) \pm 0.25\ (\text{syst.}) = 1.20 \pm 0.68\ (\text{tot.}). \tag{8}$$

The result is in agreement with the SM expectation, disfavouring the no-spin hypothesis with a significance of 1.8σ. The main systematic uncertainties arise from the signal and background modelling, as well as the

impact of $E_{\mathrm{T}}^{\mathrm{miss}}$ and flavour-tagging uncertainties on the reconstruction of the full $t\bar{t}$ system, though the measurement is dominated by the statistical uncertainty.

Table 17: Values of the f_{SM} parameter extracted from the detector-level template fits to the angular distributions listed in Table 16. The "observed" values refer to measurements in data, whereas the "expected" numbers are obtained from an Asimov dataset (with $f_{\mathrm{SM}} = 1$). Quoted are the total errors on each measurement, including both the statistical uncertainty and all sources of systematic uncertainties.

Distribution	Channel	Expected values	Observed values
$\cos\varphi$	$3\ell + 4\ell$	$1^{+1.39}_{-1.38}$	$-0.09^{+1.34}_{-1.28}$
$\cos\theta_r^+ \cdot \cos\theta_r^-$	$3\ell + 4\ell$	$1^{+1.83}_{-1.82}$	$1.17^{+1.80}_{-1.76}$
$\cos\theta_k^+ \cdot \cos\theta_k^-$	$3\ell + 4\ell$	$1^{+1.78}_{-1.78}$	$1.39^{+1.72}_{-1.73}$
$\cos\theta_n^+ \cdot \cos\theta_n^-$	$3\ell + 4\ell$	$1^{+1.87}_{-1.86}$	$-1.05^{+2.06}_{-1.96}$
$\cos\theta_r^+ \cdot \cos\theta_k^- + \cos\theta_r^- \cdot \cos\theta_k^+$	$3\ell + 4\ell$	$1^{+1.93}_{-1.93}$	$0.36^{+1.99}_{-1.93}$
$\cos\theta_r^+$	$3\ell + 4\ell$	$1^{+1.81}_{-1.80}$	$1.56^{+1.86}_{-1.98}$
$\cos\theta_r^-$	$3\ell + 4\ell$	$1^{+1.82}_{-1.78}$	$1.81^{+1.63}_{-1.68}$
$\cos\theta_k^+$	$3\ell + 4\ell$	$1^{+1.69}_{-1.67}$	$2.00^{+1.65}_{-1.70}$
$\cos\theta_k^-$	$3\ell + 4\ell$	$1^{+1.68}_{-1.68}$	$2.31^{+1.68}_{-1.68}$

11 SMEFT interpretation

The Standard Model Effective Field Theory (SMEFT) [24, 25] provides a complete phenomenological extension of the SM beyond dimension-4 terms in the Lagrangian. By employing the degrees of freedom and gauge symmetries of the SM, the SMEFT builds an infinite series of operators sorted by canonical dimension. New physics effects from Beyond the Standard Model (BSM) theories characterised by a higher mass scale than the energies probed in a typical LHC collision can therefore be related to a set of operators $\{Q\}$, together with their Wilson coefficients $\{C\}$. Observed deviations from the SM can then be expressed in terms of $\{C\}$, without specifying a particular BSM model. Similarly, LHC data found to be in agreement with the SM lead to constraints in the phenomenological space spanned by the Wilson coefficients $\{C\}$, which in turn can be translated into exclusions of various BSM scenarios. The Lagrangian of the SMEFT thus reads:

$$\mathcal{L}_{\mathrm{SMEFT}} = \mathcal{L}_{\mathrm{SM}} + \sum_{d>4} \mathcal{L}^{(d)}, \quad \mathcal{L}^{(d)} = \sum_{i=1}^{n_d} \frac{C_i^{(d)}}{\Lambda^{d-4}} Q_i^{(d)}, \tag{9}$$

where Λ is a suitable cutoff scale, chosen as the conventional $\Lambda = 1$ TeV in this analysis. The number of such operators $Q^{(d)}$, n_d, is known up to $d = 8$, however current computational tools only allow the study of SMEFT effects up to $d = 6$ where generation of LHC-like collision events is required. Operators contributing to $\mathcal{L}^{(5)}$ are known to include baryon- and lepton-number violating terms, and are therefore ignored in this analysis; similarly, higher order operators are Λ-suppressed, and therefore only $\mathcal{L}^{(6)}$ is considered in the following.

Using the EFT Monte Carlo samples described in Section 3 (produced with the `SMEFTsim 3.0` UFO model [25]), the dependence of a generic observable O (e.g. an inclusive or differential cross section) on a set of Wilson coefficients $\{C\}$ can be parameterised as:

$$O = O_{\text{SM}} + \sum_i C_i A_i + \sum_{i,j} C_i C_j B_{ij}. \tag{10}$$

The reweighting approach taken in the generation of these MC samples probes multiple values of the individual Wilson coefficients per event, as well as pairs of coefficients. A simple quadratic fit to any observable of interest therefore yields the linear term A_i, which represents the interference between the SM and the SMEFT, and the quadratic term B_{ij}, which represents a pure SMEFT contribution.[12]

In order to remove possible discrepancies between the SMEFT prediction of the SM term O_{SM}, obtained at LO in QCD, and the observed $t\bar{t}Z$ data, the SMEFT predictions for the observables are scaled by a factor $O_{\text{SM}}^{\text{NLO}}/O_{\text{SM}}^{\text{LO}}$, where $O_{\text{SM}}^{\text{NLO}}$ is obtained from the modelling of the nominal MadGraph5_aMC@NLO +Pythia 8 $t\bar{t}Z$ sample.

The SMEFT predictions rely on the `top` flavour structure of the `SMEFTsim 3.0` model, which is defined by the following assumptions:

- quarks of the first two generations and quarks of the third are described by independent fields, denoted (q, u, d) and (Q, t, b) respectively;
- a symmetry $U(2)^3 = U(2)_q \times U(2)_u \times U(2)_d$ is imposed on the Lagrangian, under which only the light quarks transform (e.g. $q \mapsto \Omega_q q$, but $t \mapsto t$);
- mixing effects in the quark sector are neglected (the CKM matrix is unity);
- a symmetry $U(1)^3_{l+e} = U(1)_e \times U(1)_\mu \times U(1)_\tau$ is imposed on the Lagrangian, which corresponds to simple flavour diagonality in the lepton sector.

In this analysis 20 dimension-6 SMEFT operators are considered, corresponding to 23 degrees of freedom (3 Wilson coefficients have a distinct imaginary part). They are defined in Table 18, and broadly fall into two classes: top-boson operators (classes 5 and 6 in the notation of Ref. [25]) and four-quark operators (classes 8a-c). The $t\bar{t}Z$ vertex is sensitive to particular combinations of some operators, which are made explicit in other models (such as `dim6top` [110]):

$$c_{tZ} = -\sin\theta_W C_{tB} + \cos\theta_W C_{tW}, \tag{11}$$

$$c^-_{\varphi Q} = C^{(1)}_{HQ} - C^{(3)}_{HQ}, \tag{12}$$

where the operators on the left-handside are in the notation of Ref. [110], and θ_W is the Weinberg angle. It is shown in the following that the above relations can be recovered by identifiying the directions in the EFT phase-space that are probed by this measurement.

[12] In what follows the "pure quadratic" and "cross" terms may be referred to, meaning B_{ii} and $B_{ij,i\neq j}$ respectively.

Table 18: Definitions of the relevant dimension-6 SMEFT operators. For the three top-boson operators indicated with a ($\star$) the real and imaginary parts of the corresponding Wilson coefficients are considered separately.

	Operator	Definition	
top-boson	O_{tW}	$(\bar{Q}\sigma^{\mu\nu}t)\sigma^i\tilde{H}W^i_{\mu\nu}$	($\star$)
	O_{tB}	$(\bar{Q}\sigma^{\mu\nu}t)\tilde{H}B_{\mu\nu}$	($\star$)
	O_{tG}	$(\bar{Q}\sigma^{\mu\nu}T^a t)\tilde{H}G^a_{\mu\nu}$	($\star$)
	$O^{(1)}_{HQ}$	$(H^\dagger i\overleftrightarrow{D}_\mu H)(\bar{Q}\gamma^\mu Q)$	
	$O^{(3)}_{HQ}$	$(H^\dagger i\overleftrightarrow{D}^i_\mu H)(\bar{Q}\sigma^i\gamma^\mu Q)$	
	O_{Ht}	$(H^\dagger i\overleftrightarrow{D}_\mu H)(\bar{t}\gamma^\mu t)$	
four-quark	$O^{(1)}_{tu}$	$(\bar{t}\gamma_\mu t)(\bar{u}\gamma^\mu u)$	
	$O^{(8)}_{tu}$	$(\bar{t}T^a\gamma_\mu t)(\bar{u}T^a\gamma^\mu u)$	
	$O^{(1)}_{td}$	$(\bar{t}\gamma_\mu t)(\bar{d}\gamma^\mu d)$	
	$O^{(8)}_{td}$	$(\bar{t}T^a\gamma_\mu t)(\bar{d}T^a\gamma^\mu d)$	
	$O^{(1)}_{qt}$	$(\bar{q}\gamma_\mu q)(\bar{t}\gamma^\mu t)$	
	$O^{(8)}_{qt}$	$(\bar{q}T^a\gamma_\mu q)(\bar{t}T^a\gamma^\mu t)$	
	$O^{(1)}_{Qu}$	$(\bar{Q}\gamma_\mu Q)(\bar{u}\gamma^\mu u)$	
	$O^{(8)}_{Qu}$	$(\bar{Q}T^a\gamma_\mu Q)(\bar{u}T^a\gamma^\mu u)$	
	$O^{(1)}_{Qd}$	$(\bar{Q}\gamma_\mu Q)(\bar{d}\gamma^\mu d)$	
	$O^{(8)}_{Qd}$	$(\bar{Q}T^a\gamma_\mu Q)(\bar{d}T^a\gamma^\mu d)$	
	$O^{(1,1)}_{Qq}$	$(\bar{Q}\gamma_\mu Q)(\bar{q}\gamma^\mu q)$	
	$O^{(3,1)}_{Qq}$	$(\bar{Q}\sigma^i\gamma_\mu Q)(\bar{q}\sigma^i\gamma^\mu q)$	
	$O^{(1,8)}_{Qq}$	$(\bar{Q}T^a\gamma_\mu Q)(\bar{q}T^a\gamma^\mu q)$	
	$O^{(3,8)}_{Qq}$	$(\bar{Q}\sigma^i T^a\gamma_\mu Q)(\bar{q}\sigma^i T^a\gamma^\mu q)$	

Several different fitting scenarios are employed to extract as much information from the data as possible, in a self-consistent way. Each fit is performed in the on-shell $t\bar{t}Z$ fiducial region (combination of the 3ℓ and 4ℓ channels), separately to the top-boson and four-quark operators of Table 18. The differential distributions unfolded to particle-level in Section 9.3 are parameterised in terms of these EFT operators, and taken as joint input measurements for the EFT interpretation.

A nominal fit using the full quadratic parametrisation of Equation (10) is considered, where both the linear and quadratic terms as well as the cross-terms are used, for all operators simultaneously. Secondly a fit where only the linear terms are present provides an approximate measure of the importance of the interference terms when compared to the full quadratic fits. Full quadratic fits are also performed for each operator individually, where only a single Wilson coefficient is probed while all others are fixed to zero, in

order to provide results which can be compared to other analyses.

Finally, following the work of Ref. [111], the inverse covariance matrix of the unfolded measurements is rotated into the space of the Wilson coefficients $\{C\}$ (top-boson and four-quark operators together), considering only the linear SM/EFT interferences. The resulting matrix provides a lower bound on the Fisher information matrix. Its eigenvectors correspond to the directions in the space of Wilson coefficients probed by the measurements, with the corresponding eigenvalues providing a measure of the sensitivity achieved along these directions. The inverse of the square root of an eigenvalue can be understood as a predictor of the limit that would be obtained when fitting the linear combination of operators defined by the eigenvector, rather than the individual operators themselves. Only the eigenvectors whose eigenvalues are greater than 0.1 are considered, corresponding to a truncation of expected limits greater than $\sim \pi$, beyond the natural range of the Wilson coefficients of $O(1)$ and the range of validity of the linear approximation.

A multimodal Gaussian likelihood function is implemented with the `EFTfitter` tool [112], relying on the `BAT.jl` package [113], to perform the EFT interpretation in a Bayesian statistical framework. The overlap in data between the different measurements is suitably taken into account via correlation matrices. The results of the various EFT fits described above are presented in Figure 13 for the two scenarios with only top-boson operators and with only four-quark operators, taking as input measurements the fiducial $t\bar{t}Z$ cross section and the following normalised differential distributions defined in the combination of the 3ℓ and 4ℓ channels at particle-level: p_{T}^{Z}, $|y^{Z}|$, $\cos\theta_{Z}^{*}$, p_{T}^{t}, $|\Delta\phi(t\bar{t},Z)|$ and $|y^{t\bar{t}Z}|$. Out of these, p_{T}^{Z} typically carries the most sensitivity to top-Z operators, whereas p_{T}^{t} is particularly relevant for constraining four-quark operators. The corresponding numerical values are reported in Tables 19 and 20. A uniform prior in the range $[-10, 10]$ is used in every case. The independent fits, where all Wilson coefficients other than the one considered are set to zero, offer the tightest constraints, typically $C/\Lambda^2 \lesssim 0.5$ TeV^{-2} in 95% credible intervals.

The quadratic fits, capturing the full EFT picture at dimension 6, also show competitive constraints in the range $C/\Lambda^2 \lesssim 0.5 - 1$ TeV^{-2} for 95% credible intervals. Some of the operators can be observed to feature slightly asymmetric limits or non-zero global modes (but still compatible with the SM within their 1σ range): this pattern is a consequence of the interplay between the different operators in the global fit, as they do not all represent directions in the EFT space that can be individually probed by the various input measurements.

This pattern is also present in the linearised global fit, which can be used to gauge the relative importance of the SM/EFT interference terms. For some operators (e.g. the imaginary and CP-violating parts of C_{tG}, C_{tW} and C_{tB}, or most of the colour-singlet four-quark operators), the results of the linear fits are not quoted since the corresponding interference term is vanishing at LO in QCD. As expected, $\Re[C_{tG}]$ and the top-Z operators $C_{HQ}^{(1)}$, $C_{HQ}^{(3)}$ and C_{Ht} have strong linear contributions; the inclusion of their pure EFT contributions in the quadratic fit however leads to tighter constraints by a factor 2 to 4. The real parts of the C_{tW} and C_{tB} operators, giving rise to weak dipole moments in the top quark, have comparatively smaller linear terms: the typically soft Z boson emission produces a momentum suppression, and there is an accidental cancellation between the $q\bar{q}$- and gg-initiated channels [114]. On the other hand, while four-quark operators can interfere with SM-like $t\bar{t}Z$ diagrams, due to the predominance of the $gg \to t\bar{t}Z$ production channel at the LHC the linearised limits are drastically reduced when introducing pure EFT contributions in the quadratic fit: for e.g. $C_{Qq}^{(3,1)}$ and $C_{Qq}^{(3,8)}$, these effects range from factor 6 to factor 30 improvements.

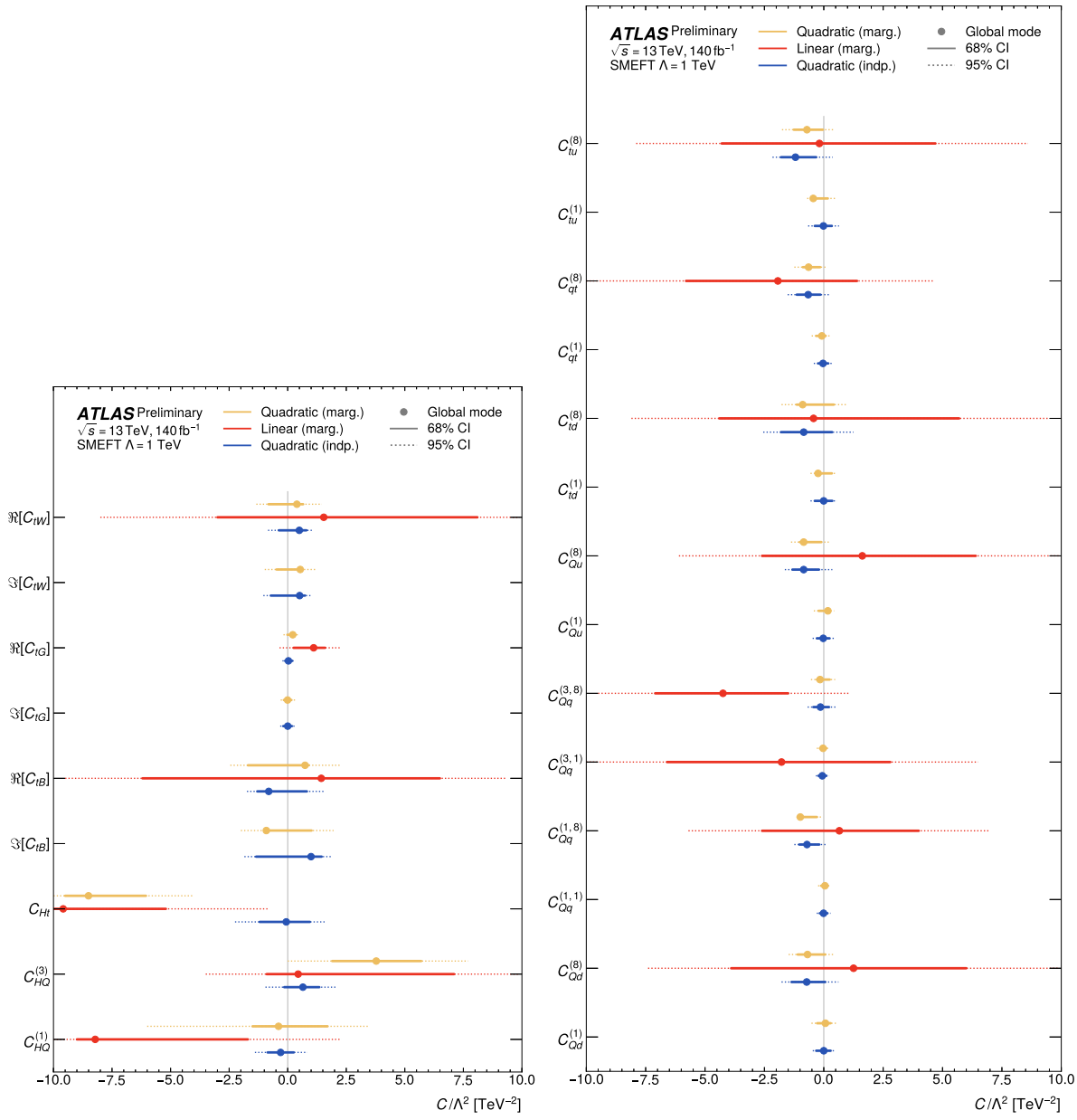

(a) (b)

Figure 13: Comparison of the 68% and 95% credible intervals obtained in the (a) top-boson scenario and (b) four-quark scenario for the marginalised linear and quadratic fits, as well as the independent quadratic fit. The imaginary (CP-violating) part of the C_{tW} and C_{tB} operators, as well as the colour-singlet four-quark operator, have no interference with the SM at leading order: no linear fit (red) is performed. Also shown are the best-fit values (global mode) for each operator.

Table 19: Observed and expected 68% and 95% credible intervals for the top-boson operators, comparing the results obtained from the marginalised linear and quadratic fits, as well as the independent quadratic fit. Also shown are the best-fit values (global mode) for each operator.

Wilson coefficient		68% CI (exp.)	95% CI (exp.)	68% CI (obs.)	95% CI (obs.)	Best-fit
$C_{HQ}^{(1)}$	$\mathcal{O}(\Lambda^{-2})$ (marg.)	$[-5.1, 5.4]$	$[-8.9, 8.7]$	$[-9.0, -1.7]$	$[-10, 2.3]$	-8
	$\mathcal{O}(\Lambda^{-4})$ (marg.)	$[-1.2, 1.8]$	$[-3.1, 4.7]$	$[-1.5, 1.7]$	$[-6.0, 3.5]$	-0.4
	$\mathcal{O}(\Lambda^{-4})$ (indep.)	$[-0.58, 0.56]$	$[-1.1, 1.1]$	$[-0.86, 0.26]$	$[-1.4, 0.84]$	-0.3
$C_{HQ}^{(3)}$	$\mathcal{O}(\Lambda^{-2})$ (marg.)	$[-4.7, 4.7]$	$[-8.5, 8.4]$	$[-0.90, 7.1]$	$[-3.5, 9.9]$	0.5
	$\mathcal{O}(\Lambda^{-4})$ (marg.)	$[-1.1, 2.6]$	$[-2.8, 4.4]$	$[1.9, 5.7]$	$[0, 7.7]$	4
	$\mathcal{O}(\Lambda^{-4})$ (indep.)	$[-0.85, 0.75]$	$[-1.6, 1.4]$	$[-0.15, 1.3]$	$[-0.95, 2.0]$	0.7
C_{Ht}	$\mathcal{O}(\Lambda^{-2})$ (marg.)	$[-4.3, 4.2]$	$[-7.9, 8.1]$	$[-10, -5.2]$	$[-10, -0.80]$	-10
	$\mathcal{O}(\Lambda^{-4})$ (marg.)	$[-4.0, 0.90]$	$[-6.1, 3.5]$	$[-9.5, -6.0]$	$[-10, -4.0]$	-9
	$\mathcal{O}(\Lambda^{-4})$ (indep.)	$[-1.0, 0.95]$	$[-2.0, 1.7]$	$[-1.2, 0.95]$	$[-2.2, 1.6]$	-0.06
$\Im[C_{tB}]$	$\mathcal{O}(\Lambda^{-2})$ (marg.)	—	—	—	—	—
	$\mathcal{O}(\Lambda^{-4})$ (marg.)	$[-0.84, 1.0]$	$[-1.6, 1.7]$	$[-0.80, 1.0]$	$[-2.0, 2.0]$	-0.9
	$\mathcal{O}(\Lambda^{-4})$ (indep.)	$[-1.0, 1.0]$	$[-1.6, 1.6]$	$[-1.4, 1.5]$	$[-1.9, 1.9]$	1
$\Re[C_{tB}]$	$\mathcal{O}(\Lambda^{-2})$ (marg.)	$[-6.7, 6.7]$	$[-9.3, 9.7]$	$[-6.2, 6.5]$	$[-9.5, 9.3]$	1
	$\mathcal{O}(\Lambda^{-4})$ (marg.)	$[-1.3, 0.90]$	$[-2.3, 2.0]$	$[-1.7, 0.90]$	$[-2.5, 2.3]$	0.7
	$\mathcal{O}(\Lambda^{-4})$ (indep.)	$[-1.0, 0.92]$	$[-1.6, 1.6]$	$[-1.3, 0.82]$	$[-1.7, 1.6]$	-0.8
$\Im[C_{tG}]$	$\mathcal{O}(\Lambda^{-2})$ (marg.)	—	—	—	—	—
	$\mathcal{O}(\Lambda^{-4})$ (marg.)	$[-0.19, 0.17]$	$[-0.32, 0.32]$	$[-0.16, 0.16]$	$[-0.30, 0.31]$	-0.01
	$\mathcal{O}(\Lambda^{-4})$ (indep.)	$[-0.22, 0.22]$	$[-0.36, 0.36]$	$[-0.19, 0.18]$	$[-0.32, 0.33]$	-0
$\Re[C_{tG}]$	$\mathcal{O}(\Lambda^{-2})$ (marg.)	$[-0.70, 0.70]$	$[-1.4, 1.3]$	$[0.25, 1.6]$	$[-0.35, 2.2]$	1
	$\mathcal{O}(\Lambda^{-4})$ (marg.)	$[-0.11, 0.23]$	$[-0.27, 0.38]$	$[-0.015, 0.32]$	$[-0.18, 0.43]$	0.2
	$\mathcal{O}(\Lambda^{-4})$ (indep.)	$[-0.14, 0.21]$	$[-0.26, 0.36]$	$[-0.11, 0.20]$	$[-0.23, 0.34]$	0.03
$\Im[C_{tW}]$	$\mathcal{O}(\Lambda^{-2})$ (marg.)	—	—	—	—	—
	$\mathcal{O}(\Lambda^{-4})$ (marg.)	$[-0.56, 0.56]$	$[-1.1, 1.1]$	$[-0.48, 0.62]$	$[-0.98, 1.2]$	0.5
	$\mathcal{O}(\Lambda^{-4})$ (indep.)	$[-0.56, 0.56]$	$[-0.92, 0.92]$	$[-0.72, 0.74]$	$[-1.0, 1.0]$	0.5
$\Re[C_{tW}]$	$\mathcal{O}(\Lambda^{-2})$ (marg.)	$[-5.8, 5.9]$	$[-9.4, 9.7]$	$[-3.0, 8.1]$	$[-8.0, 9.9]$	2
	$\mathcal{O}(\Lambda^{-4})$ (marg.)	$[-0.72, 0.60]$	$[-1.3, 1.3]$	$[-0.82, 0.66]$	$[-1.3, 1.5]$	0.4
	$\mathcal{O}(\Lambda^{-4})$ (indep.)	$[-0.52, 0.60]$	$[-0.88, 0.92]$	$[-0.38, 0.80]$	$[-0.84, 1.0]$	0.5

Table 20: Observed and expected 68% and 95% credible intervals for the four-quark operators, comparing the results obtained from the marginalised linear and quadratic fits, as well as the independent quadratic fit. Also shown are the best-fit values (global mode) for each operator.

Wilson coefficient		68% CI (exp.)	95% CI (exp.)	68% CI (obs.)	95% CI (obs.)	Best-fit
$C_{Qd}^{(1)}$	$\mathcal{O}(\Lambda^{-2})$ (marg.)	—	—	—	—	—
	$\mathcal{O}(\Lambda^{-4})$ (marg.)	$[-0.31, 0.32]$	$[-0.54, 0.55]$	$[-0.28, 0.29]$	$[-0.52, 0.53]$	0.07
	$\mathcal{O}(\Lambda^{-4})$ (indep.)	$[-0.39, 0.37]$	$[-0.56, 0.56]$	$[-0.32, 0.29]$	$[-0.47, 0.46]$	-0
$C_{Qd}^{(8)}$	$\mathcal{O}(\Lambda^{-2})$ (marg.)	$[-4.8, 5.0]$	$[-8.7, 8.6]$	$[-3.9, 6.0]$	$[-7.4, 9.9]$	1
	$\mathcal{O}(\Lambda^{-4})$ (marg.)	$[-0.90, 0.34]$	$[-1.5, 0.82]$	$[-1.1, 0.060]$	$[-1.5, 0.46]$	-0.7
	$\mathcal{O}(\Lambda^{-4})$ (indep.)	$[-1.4, 0.50]$	$[-2.0, 1.1]$	$[-1.4, 0.060]$	$[-1.8, 0.62]$	-0.7
$C_{Qq}^{(1,1)}$	$\mathcal{O}(\Lambda^{-2})$ (marg.)	—	—	—	—	—
	$\mathcal{O}(\Lambda^{-4})$ (marg.)	$[-0.14, 0.17]$	$[-0.29, 0.30]$	$[-0.11, 0.17]$	$[-0.24, 0.30]$	0.05
	$\mathcal{O}(\Lambda^{-4})$ (indep.)	$[-0.21, 0.21]$	$[-0.34, 0.34]$	$[-0.17, 0.16]$	$[-0.29, 0.29]$	-0.01
$C_{Qq}^{(1,8)}$	$\mathcal{O}(\Lambda^{-2})$ (marg.)	$[-3.3, 3.3]$	$[-6.6, 6.5]$	$[-2.6, 4.0]$	$[-5.7, 7.0]$	0.7
	$\mathcal{O}(\Lambda^{-4})$ (marg.)	$[-0.72, -0.090]$	$[-1.0, 0.19]$	$[-0.89, -0.29]$	$[-1.1, -0.030]$	-1
	$\mathcal{O}(\Lambda^{-4})$ (indep.)	$[-0.76, 0.28]$	$[-1.3, 0.40]$	$[-1.0, -0.19]$	$[-1.2, 0.080]$	-0.7
$C_{Qq}^{(3,1)}$	$\mathcal{O}(\Lambda^{-2})$ (marg.)	$[-4.9, 5.0]$	$[-8.6, 8.8]$	$[-6.6, 2.8]$	$[-10, 6.5]$	-2
	$\mathcal{O}(\Lambda^{-4})$ (marg.)	$[-0.18, 0.13]$	$[-0.32, 0.26]$	$[-0.17, 0.12]$	$[-0.29, 0.24]$	-0.03
	$\mathcal{O}(\Lambda^{-4})$ (indep.)	$[-0.26, 0.18]$	$[-0.41, 0.31]$	$[-0.23, 0.11]$	$[-0.34, 0.23]$	-0.06
$C_{Qq}^{(3,8)}$	$\mathcal{O}(\Lambda^{-2})$ (marg.)	$[-2.9, 2.9]$	$[-5.7, 5.8]$	$[-7.1, -1.5]$	$[-9.5, 1.1]$	-4
	$\mathcal{O}(\Lambda^{-4})$ (marg.)	$[-0.31, 0.29]$	$[-0.57, 0.55]$	$[-0.29, 0.25]$	$[-0.54, 0.48]$	-0.2
	$\mathcal{O}(\Lambda^{-4})$ (indep.)	$[-0.42, 0.48]$	$[-0.74, 0.76]$	$[-0.44, 0.22]$	$[-0.68, 0.54]$	-0.1
$C_{Qu}^{(1)}$	$\mathcal{O}(\Lambda^{-2})$ (marg.)	—	—	—	—	—
	$\mathcal{O}(\Lambda^{-4})$ (marg.)	$[-0.26, 0.24]$	$[-0.46, 0.44]$	$[-0.22, 0.24]$	$[-0.42, 0.43]$	0.2
	$\mathcal{O}(\Lambda^{-4})$ (indep.)	$[-0.37, 0.35]$	$[-0.59, 0.56]$	$[-0.29, 0.24]$	$[-0.47, 0.43]$	-0.02
$C_{Qu}^{(8)}$	$\mathcal{O}(\Lambda^{-2})$ (marg.)	$[-4.7, 4.6]$	$[-8.4, 8.5]$	$[-2.6, 6.4]$	$[-6.1, 9.9]$	2
	$\mathcal{O}(\Lambda^{-4})$ (marg.)	$[-0.82, 0.18]$	$[-1.3, 0.60]$	$[-1.0, -0.10]$	$[-1.4, 0.27]$	-0.8
	$\mathcal{O}(\Lambda^{-4})$ (indep.)	$[-1.2, 0.34]$	$[-1.7, 0.80]$	$[-1.3, -0.20]$	$[-1.6, 0.36]$	-0.8
$C_{qt}^{(1)}$	$\mathcal{O}(\Lambda^{-2})$ (marg.)	—	—	—	—	—
	$\mathcal{O}(\Lambda^{-4})$ (marg.)	$[-0.28, 0.16]$	$[-0.47, 0.34]$	$[-0.32, 0.080]$	$[-0.51, 0.27]$	-0.08
	$\mathcal{O}(\Lambda^{-4})$ (indep.)	$[-0.31, 0.27]$	$[-0.50, 0.45]$	$[-0.24, 0.19]$	$[-0.42, 0.36]$	-0.03
$C_{qt}^{(8)}$	$\mathcal{O}(\Lambda^{-2})$ (marg.)	$[-3.6, 3.6]$	$[-7.1, 7.1]$	$[-5.8, 1.4]$	$[-10, 4.6]$	-2
	$\mathcal{O}(\Lambda^{-4})$ (marg.)	$[-0.68, 0.080]$	$[-1.1, 0.36]$	$[-0.88, -0.15]$	$[-1.2, 0.12]$	-0.6
	$\mathcal{O}(\Lambda^{-4})$ (indep.)	$[-0.90, 0.36]$	$[-1.6, 0.54]$	$[-1.1, -0.14]$	$[-1.5, 0.22]$	-0.7
$C_{td}^{(1)}$	$\mathcal{O}(\Lambda^{-2})$ (marg.)	—	—	—	—	—
	$\mathcal{O}(\Lambda^{-4})$ (marg.)	$[-0.32, 0.38]$	$[-0.53, 0.57]$	$[-0.35, 0.34]$	$[-0.56, 0.54]$	-0.2
	$\mathcal{O}(\Lambda^{-4})$ (indep.)	$[-0.62, 0.64]$	$[-1.0, 1.0]$	$[-0.38, 0.36]$	$[-0.56, 0.56]$	-0
$C_{td}^{(8)}$	$\mathcal{O}(\Lambda^{-2})$ (marg.)	$[-5.0, 5.1]$	$[-8.9, 8.8]$	$[-4.4, 5.7]$	$[-8.1, 9.5]$	-0.4
	$\mathcal{O}(\Lambda^{-4})$ (marg.)	$[-1.0, 0.68]$	$[-1.8, 1.3]$	$[-1.1, 0.42]$	$[-1.8, 0.94]$	-0.9
	$\mathcal{O}(\Lambda^{-4})$ (indep.)	$[-1.8, 0.85]$	$[-2.8, 1.7]$	$[-1.8, 0.35]$	$[-2.5, 1.2]$	-0.8
$C_{tu}^{(1)}$	$\mathcal{O}(\Lambda^{-2})$ (marg.)	—	—	—	—	—
	$\mathcal{O}(\Lambda^{-4})$ (marg.)	$[-0.31, 0.34]$	$[-0.59, 0.63]$	$[-0.44, 0.17]$	$[-0.70, 0.47]$	-0.4
	$\mathcal{O}(\Lambda^{-4})$ (indep.)	$[-0.46, 0.46]$	$[-0.76, 0.76]$	$[-0.38, 0.34]$	$[-0.66, 0.64]$	-0.01
$C_{tu}^{(8)}$	$\mathcal{O}(\Lambda^{-2})$ (marg.)	$[-4.6, 4.4]$	$[-8.4, 8.2]$	$[-4.3, 4.7]$	$[-7.9, 8.6]$	-0.2
	$\mathcal{O}(\Lambda^{-4})$ (marg.)	$[-1.0, 0.32]$	$[-1.6, 0.90]$	$[-1.3, -0.040]$	$[-1.8, 0.46]$	-0.7
	$\mathcal{O}(\Lambda^{-4})$ (indep.)	$[-1.6, 0.50]$	$[-2.2, 1.2]$	$[-1.8, -0.32]$	$[-2.2, 0.38]$	-1

The covariance matrix obtained in the linear fit is inverted to yield a lower bound on the underlying Fisher information matrix, and a new linear fit in the rotated EFT directions of sensitivity, as previously described, is performed. The following eigenvectors are extracted, corresponding to eigenvalues larger than 0.1:

$$\begin{aligned}
\lambda_1 = 40,\ \mathcal{F}_1 : &+ 0.75 \cdot \Re[C_{tG}] + 0.01 \cdot \Re[C_{tW}] + 0.23 \cdot C_{HQ}^{(1)} - 0.15 \cdot C_{HQ}^{(3)} - 0.13 \cdot C_{Ht} - 0.10 \cdot C_{Qd}^{(8)} \\
&- 0.42 \cdot C_{Qq}^{(1,8)} - 0.15 \cdot C_{Qq}^{(3,1)} + 0.06 \cdot C_{Qq}^{(3,8)} - 0.13 \cdot C_{Qu}^{(8)} - 0.05 \cdot C_{td}^{(8)} - 0.33 \cdot C_{qt}^{(8)} - 0.08 \cdot C_{tu}^{(8)}, \qquad (13) \\
\lambda_2 = 8,\ \mathcal{F}_2 : &- 0.41 \cdot \Re[C_{tG}] + 0.04 \cdot \Re[C_{tW}] - 0.02 \cdot \Re[C_{tB}] - 0.34 \cdot C_{HQ}^{(1)} + 0.27 \cdot C_{HQ}^{(3)} + 0.18 \cdot C_{Ht} \\
&- 0.12 \cdot C_{Qd}^{(8)} - 0.57 \cdot C_{Qq}^{(1,8)} - 0.22 \cdot C_{Qq}^{(3,1)} - 0.05 \cdot C_{Qq}^{(3,8)} - 0.22 \cdot C_{Qu}^{(8)} - 0.05 \cdot C_{td}^{(8)} - 0.39 \cdot C_{qt}^{(8)} \\
&- 0.12 \cdot C_{tu}^{(8)}, \qquad (14) \\
\lambda_3 = 0.5,\ \mathcal{F}_3 : &- 0.07 \cdot \Re[C_{tG}] + 0.06 \cdot \Re[C_{tW}] - 0.01 \cdot \Re[C_{tB}] + 0.18 \cdot C_{HQ}^{(1)} + 0.04 \cdot C_{HQ}^{(3)} - 0.33 \cdot C_{Ht} \\
&- 0.07 \cdot C_{Qd}^{(8)} + 0.13 \cdot C_{Qq}^{(1,8)} + 0.04 \cdot C_{Qq}^{(3,1)} - 0.68 \cdot C_{Qq}^{(3,8)} - 0.42 \cdot C_{Qu}^{(8)} - 0.11 \cdot C_{td}^{(8)} + 0.08 \cdot C_{qt}^{(8)} \\
&- 0.41 \cdot C_{tu}^{(8)}. \qquad (15)
\end{aligned}$$

These relations can also be visualised in Figure 14. Of particular interest is the combination $\mathcal{F}_1$, which clearly emerges as the most important direction of SMEFT constraints in the linear fit. It features most prominently the $\Re[C_{tG}]$ operator together with the two four-quark operators $C_{Qq}^{(1,8)}$ and $C_{qt}^{(8)}$ that couple the top quark field to left-handed light quark fields, but also involves a non-trivial combination of most of the other operators. From the inverse square root of the eigenvalue λ_1, limits on $\mathcal{F}_1$ are expected to be set at $\sim 0.15\ \text{TeV}^{-2}$.

While no clear picture of the four-quark sector appears, some of the expected relations between top-boson operators are recovered (see Equation (11)). The effective impact of $\Re[C_{tG}]$ in the linear combination $\mathcal{F}_1$ was gauged by separating it from the four-quark operators: it is much more constrained than the top-Z operators, but surprisingly to a similar level as the leading combination of four-quark operators. In other words, while the $t\bar{t}Z$ process is mostly gluon-initiated and therefore sensitive to modifications of the top-gluon vertex by the operator $\Re[C_{tG}]$, it is also highly affected by any non-SM-like structure in the quark-initated channel. The linear combinations in the subspace of four-quark operators should be compared to those found elsewhere for the $t\bar{t}$ process: the possibility of radiating the Z boson in $t\bar{t}Z$ production from an initial-state quark should provide novel directions of sensitivity.

The results of the linearised Fisher-rotated fit are presented in Figure 15 and Table 21. The limit expected by construction on $\mathcal{F}_1$ is indeed recovered.

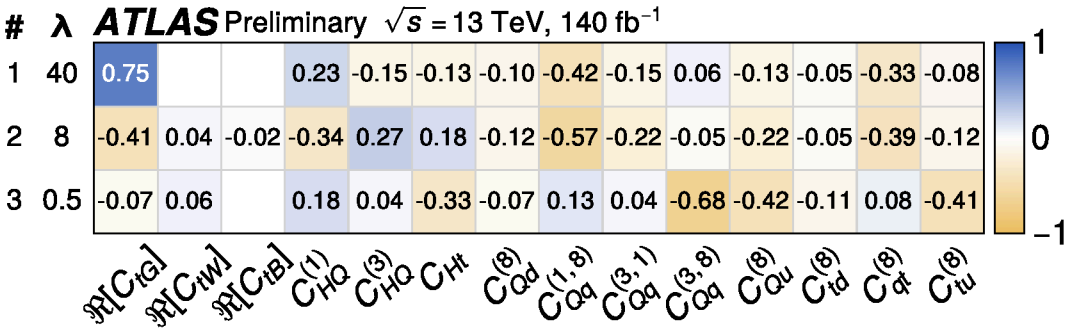

Figure 14: Eigenvector decomposition of the Fisher information matrix obtained from the linear global EFT fit. Each row represents a Fisher-rotated direction $\mathcal{F}$, for which the corresponding eigenvalue satisfies $\lambda > 0.1$, expressed in terms of the underlying Wilson coefficients in the Warsaw basis (columns).

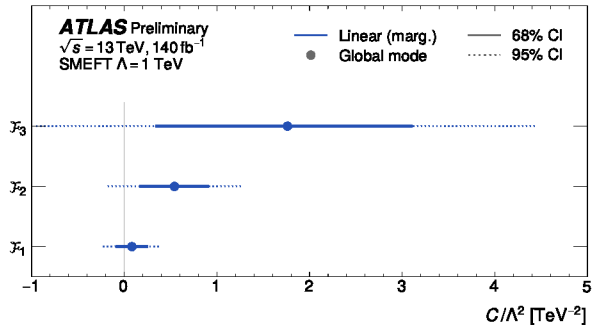

Figure 15: Comparison of the 68% and 95% credible intervals obtained for the Fisher-rotated linear fit. Also shown are the best-fit values (global mode) for each linear combination.

Table 21: Observed and expected 68% and 95% credible intervals for the main EFT directions of sensitivity, showing the results obtained from the Fisher-rotated linear fit. Also shown are the best-fit values (global mode) for each linear combination.

Wilson coefficient		68% CI (exp.)	95% CI (exp.)	68% CI (obs.)	95% CI (obs.)	Best-fit
$\mathcal{F}_1$	$O(\Lambda^{-2})$ (marg.)	$[-0.15, 0.16]$	$[-0.30, 0.31]$	$[-0.080, 0.24]$	$[-0.23, 0.39]$	0.08
$\mathcal{F}_2$	$O(\Lambda^{-2})$ (marg.)	$[-0.36, 0.36]$	$[-0.72, 0.70]$	$[0.18, 0.90]$	$[-0.18, 1.3]$	0.5
$\mathcal{F}_3$	$O(\Lambda^{-2})$ (marg.)	$[-1.4, 1.3]$	$[-2.7, 2.7]$	$[0.35, 3.1]$	$[-0.95, 4.5]$	2

12 Conclusion

This paper has presented the measurements of the inclusive and differential production cross sections of a pair of top-anti-top quarks in association with a Z boson ($t\bar{t}Z$). The full Run 2 dataset collected with the ATLAS experiment between 2015 and 2018, amounting to an integrated luminosity of 140 fb^{-1}, has been

used for this analysis. The targeted final states feature two, three or four leptons, focusing on the decay of the Z boson to pairs of electrons and muons but remain inclusive in the decays of the $t\bar{t}$ system. This analysis supersedes, and largely improves, upon the previous Run 2 ATLAS result [23].

The inclusive $t\bar{t}Z$ cross section corresponding to the on-shell Z phase-space region for difermion masses in $70 < m_{f\bar{f}} < 110$ GeV is measured to be $\sigma_{t\bar{t}Z} = 0.86 \pm 0.06\,\text{pb} = 0.86 \pm 0.04(\text{stat.}) \pm 0.04(\text{syst.})$ pb. The observed result is in agreement with the SM prediction $\sigma_{t\bar{t}Z}^{\text{NLO+NNLL}} = 0.86^{+0.08}_{-0.09}$ pb [20] and other calculations at NLO QCD and electroweak accuracy [19, 21, 115]. The result is limited by the systematic uncertainties associated with the modelling of background processes (Z+jets, non-prompt leptons), renormalisation and factorisation scales of the signal process, and the determination of the integrated luminosity. The total uncertainty on the $t\bar{t}Z$ cross section is reduced by 35% (factor 2 for the systematic uncertainties alone) compared to the previous analysis in Ref. [23].

Detector-level observables sensitive to polarisation and spin correlation of the top quarks are statistically combined to search for such effects, for the first time in $t\bar{t}Z$ production. Simulated templates of $t\bar{t}Z$ events with and without the SM spin density matrix are used to extract a fraction of SM-like spin $f_{\text{SM}} = 1.20 \pm 0.68$, where the total uncertainty is largely dominated by its statistical component. This result is in agreement with the SM, and represents a 1.8σ departure from the null hypothesis of no spin correlations.

Furthermore, absolute and normalised differential production cross sections of the $t\bar{t}Z$ process are presented, in a large number of observables sensitive to MC modelling and potential BSM effects. Distributions at particle- and parton-level, unfolded to specific fiducial volumes, are compared to various choices of $t\bar{t}Z$ MC generators and fixed-order theoretical predictions. Since the difference between the MC generators considered in this analysis is usually significantly smaller than the uncertainty of the measurement, it is not possible to decide which generators describe the data better.

Finally, the unfolded particle-level distributions are used to constrain potential BSM effects from dimension-6 operators in the framework of the SMEFT. Various fitting scenarios are considered, in order to give a complete picture of EFT effects in $t\bar{t}Z$ production. A large number of operators are considered, affecting both the top-Z coupling and $t\bar{t}$ production, and also including four-quark operators. The three most sensitive directions in the EFT space are identified through the Fisher information matrix of the measurements and lead to the tightest constraints. Compared to recent EFT searches covering large regions of phase-space and including multiple $t\bar{t} + X$ processes [116], the results presented in this paper leverage more information from the measurement of a single process. Overall, no significant devation from the SM is observed, and exclusion limits are placed on several top-electroweak and four-quark SMEFT operators.

Appendix

This Appendix provides additional information on the MVA approaches used to measure the inclusive $t\bar{t}Z$ cross section, as well as the full set of differential cross sections (absolute and normalised, unfolded to particle- and parton-level) and further details on the unfolding procedure.

Tables 22, 23 and 24 list the kinematic quantities used as inputs to the training of the DNNs in the 2ℓ, 3ℓ and 4ℓ channels respectively. Table 25 collects the specific binning used for each differential cross section measurement; the same binning is used whether unfolding to particle- or parton-level.

Figures 16 to 23 present the differential cross sections for observables defined in the combination of the 3ℓ and 4ℓ fiducial volumes. Each figure contains four distributions: unfolded to particle- or parton-level, absolute or normalised cross sections. Figures 24 to 28 similarly correspond to observables defined in the 3ℓ channel, and Figures 29 to 31 to those defined in the 4ℓ channel.

Finally, Tables 26 and 27 summarise the compatibility of the unfolded data with predictions from various MC generators, for the absolute and normalised differential spectra respectively.

Table 22: Definition of the DNN variables used in 2ℓOS signal regions. Jets and leptons are ordered by their p_{T} starting with the largest. To suppress effect of the mismodelling in the events with high jet multiplicity, only the first 8 jets ordered by p_{T} are considered when calculating DNN input variables if an event has more than 8 jets, otherwise all jets in the event are considered.

Variable	**Definition**
H_T	sum of p_T of all objects (jets and leptons) in the event
$H_{\mathrm{T}}^{\mathrm{jets}}$	sum of p_T of all jets in the event
$p_{\mathrm{T}}^{X.\mathrm{jet}}$	p_T of the Xth jet, where only the first 8 jets are considered
$p_{\mathrm{T}}^{X.\mathrm{lep}}$	p_T of the Xth lepton
W_{1t1W}	weight for one-top hypothesis and 1W from multihypothesis hadronic t/W reconstruction. It is the probability that the event contains all 3 jets from one of the top quark and two light jets from the decay of the other top quark. More details are provided in Section 5.5.
W_{1t}	weight for one-top hypothesis from multihypothesis hadronic t/W reconstruction. The same as W_{1t1W}, with one top quark only.
$Centr_{\mathrm{jets}}$	scalar sum of p_T divided by sum of E for all jets
$\Delta R(b_1, b_2)$	ΔR between two jets with highest b-tagging working point. The jets with the same working point are ordered by p_{T}.
H_1^{jets}	first Fox-Wolfram moment built from jets only. The first Fox-Wolfram moment is defined as $H_1 = \sum_{i,j} \frac{\vec{p}_i \cdot \vec{p}_j}{E_{vis}^2}$, where $\vec{p}_i$ and $\vec{p}_j$ are 3-momenta of i-th and j-th object (jet or lepton) and E_{vis} is all visible energy in the event.
$N_{jj}^{m<50\mathrm{GeV}}$	number of jj combinations with mass lower than 50 GeV
m_Z, y^Z, p_{T}^Z	mass, rapidity and transverse momentum of Z boson
$minM_{jj}^{\mathrm{ave}}$	average (over the number of jets in event) minimum invariant mass of jet pairs. For each jet, the other jet which results in the minimum dijet invariant mass is found. The observable is the average of these masses over all jets in the event.
$\Delta R(l, l)$	ΔR between two leptons
PCBT_{Xj}	discretised b-tagging efficiency (100-85-77-70-60%) of the Xth jet
$N_{\mathrm{lep}}^{\mathrm{top}}$	number of leptonic top candidates
$N_{\mathrm{had}}^{\mathrm{top}}$	number of hadronic top candidates
N_{had}^{W}	number of hadronic W candidates
$E_{\mathrm{T}}^{\mathrm{miss}}$	missing transverse energy in the event
H_1	first Fox-Wolfram momentent built from jets and leptons
$p_{\mathrm{T}}^{t\bar{t},\mathrm{spanet}}$	transverse momentum of the $t\bar{t}$ system reconstructed from jets predicted by SPANet

Table 23: Definition of the DNN variables used in 3ℓ signal regions. Jets and leptons are ordered by their p_{T} starting with the largest.

Variable	**Definition**
PCBT_{b1}	highest discretised b-tagging efficiency (100-85-77-70-60%) of all jets in the event.
PCBT_{b2}	second highest discretised b-tagging efficiency of all jets in the event.
Jet $p_{\mathrm{T},i}$	transverse momentum of the i'th jet in the event where $i \in [1,4]$
$E_{\mathrm{T}}^{\mathrm{miss}}$	missing transverse energy of the event
Lepton $p_{\mathrm{T},i}$	transverse momentum of the i'th lepton in the event where $i \in [1,3]$
m_t^{lep}	reconstructed mass of the leptonically decaying top quark
m_t^{had}	reconstructed mass of the hadronically decaying top quark
N_{jets}	jet multiplicity in event
Leading b-tagged jet p_{T}	transverse momentum of the jet with the highest discretised b-tagging efficiency. If two have the same bin the leading p_{T} jet of the two is used.
H_{T}	sum of the transverse momentum of all jets in the event
$\Delta R(l_i, b_1)$	distance in ΔR between the i'th lepton and the b-tagged jet tagged with the highest working point in the event where $i \in [1,3]$
$p_{\mathrm{T},i}^{Z}$	transverse momentum of the first and second lepton ($i \in [1,2]$) assigned to the Z boson based on their invariant mass being closest to the Z mass
η_i^{Z}	pseudo-rapidity of the first and second lepton ($i \in [1,2]$) assigned to the Z boson based on their invariant mass being closest to the Z mass
Lepton $p_{\mathrm{T}}^{\mathrm{non-}Z}$	transverse momentum of the remaining lepton not assigned to the Z boson

Table 24: Definition of the DNN variables used in 4ℓ signal regions for the same-flavour (SF) and different-flavour (DF) trainings. Jets and leptons are ordered by their p_{T} starting with the largest.

Variable	**Definition**	**SF**	**DF**
E_T^{miss}	the missing transverse energy in the event	✓	—
$m^{\ell\ell,non-Z}$	the invariant mass of two leptons which were not reconstructed as originating from Z	✓	✓
2νSM weight	the output of the *Two neutrino scanning method* for event	✓	✓
p_T^Z	the transverse momentum of OSSF lepton pair identified as Z pair (invariant mass of lepton pair closest to Z mass)	✓	✓
$m_t^{\ell b}$	the invariant mass of lepton and b-tagged jet reconstructed as originating from top by *Two neutrino scanning method*	✓	✓
$m_{\bar{t}}^{\ell b}$	the invariant mass of lepton and b-tagged jet reconstructed as originating from antitop by *Two neutrino scanning method*	✓	✓
PCBT_{b1}	highest discretised b-tagging efficiency (100-85-77-70-60%) of all jets in the event.	✓	—
$p_T^{\mathrm{lep}_1}$	the transverse momentum of the leading lepton	✓	✓
$p_T^{\mathrm{jet}_2}$	the transverse momentum of the sub-leading jet	✓	✓
PCBT_{b2}	second highest discretised b-tagging efficiency of all jets in the event.		
N_{jets}	jet multiplicity in event	—	✓
$N_{b-\mathrm{tagged\ jets}}$	b-tagged jet multiplicity in event	—	✓

Table 25: Bin ranges for the differential observables defined in Table 15. The bin ranges are identical for particle- and parton-level measurements.

Observable	Channels	Bins	Bin Ranges
p_{T}^{Z} [GeV]	$3\ell + 4\ell$	8	[0, 60, 100, 140, 180, 230, 280, 350, 1000]
$\lvert y^{Z} \rvert$	$3\ell + 4\ell$	9	[0, 0.125, 0.275, 0.425, 0.6, 0.775, 0.95, 1.175, 1.45, 2.5]
$p_{\mathrm{T}}^{\ell,\mathrm{non}-Z}$	3ℓ	5	[0, 35, 55, 80, 120, 500]
$\lvert \Delta y(Z, t_{\mathrm{lep}}) \rvert$	3ℓ	5	[0, 0.25, 0.6, 1.05, 1.55, 5]
$\lvert \Delta\phi(Z, t_{\mathrm{lep}}) \rvert$	3ℓ	6	[0, 0.16, 0.44, 0.66, 0.82, 0.93, 1]
$\lvert \Delta\phi(\ell_t^+, \ell_{\bar{t}}^-) \rvert$	4ℓ	7	[0, 0.2, 0.37, 0.53, 0.67, 0.79, 0.89, 1]
H_{T}^{ℓ}	3ℓ	8	[50, 130, 165, 195, 230, 275, 330, 405, 800]
H_{T}^{ℓ}	4ℓ	5	[50, 195, 250, 315, 400, 800]
N_{jets}	3ℓ	4	[2.5, 3.5, 4.5, 5.5, 10.5]
N_{jets}	4ℓ	3	[1.5,2.5,3.5,8.5]
p_{T}^{t} [GeV]	$3\ell + 4\ell$	10	[0, 48, 80, 112, 144, 176, 216, 256, 296, 352, 800]
$p_{\mathrm{T}}^{t\bar{t}}$ [GeV]	$3\ell + 4\ell$	10	[0, 50, 80, 110, 140, 170, 210, 250, 290, 330, 1000]
$\lvert \Delta\phi(t\bar{t}, Z) \rvert / \pi$	$3\ell + 4\ell$	5	[0, 0.73, 0.86, 0.94, 0.98, 1]
$m_{t\bar{t}}$ [GeV]	$3\ell + 4\ell$	10	[0, 370, 420, 470, 530, 600, 680, 780, 890, 1010, 2000]
$m_{t\bar{t}Z}$ [GeV]	$3\ell + 4\ell$	10	[400, 580, 650, 720, 800, 890, 990, 1100, 1220, 1350, 2000]
$\lvert y^{t\bar{t}Z} \rvert$	$3\ell + 4\ell$	10	[0, 0.075, 0.2, 0.35, 0.5, 0.65, 0.8, 0.95, 1.1, 1.25, 2.5]
$\cos\theta_{Z}^{*}$	$3\ell + 4\ell$	8	[-1, -0.75, -0.5, -0.25, 0, 0.25, 0.5, 0.75, 1]

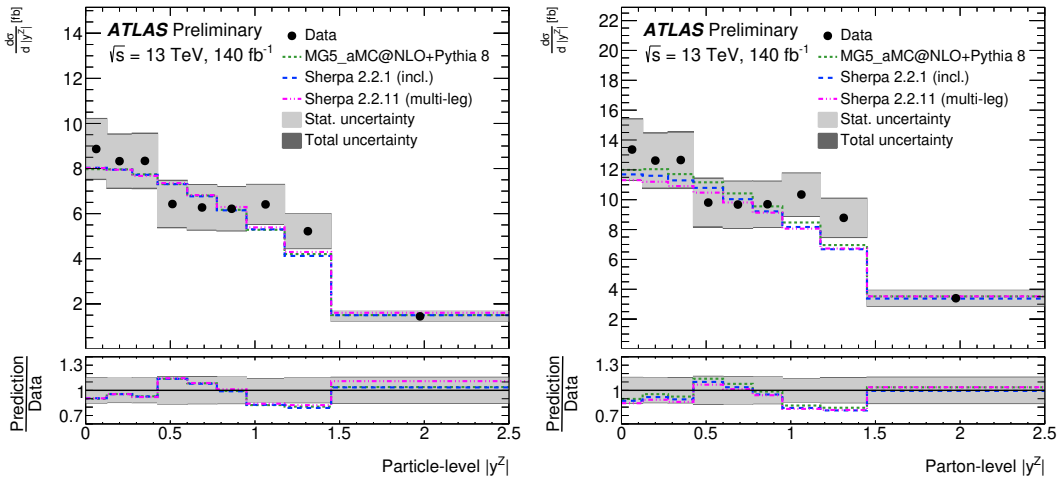

(a) (b)

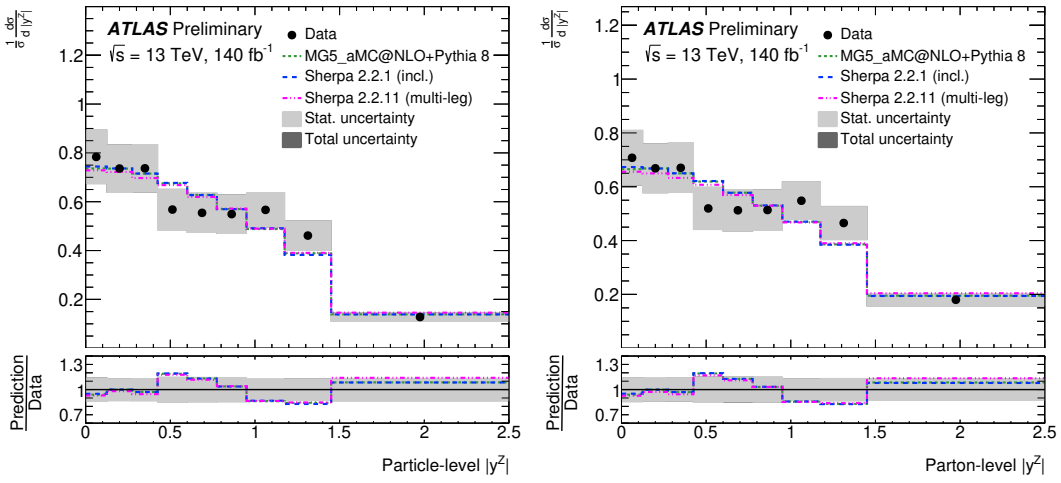

(c) (d)

Figure 16: Cross section measurement of the $|y^Z|$ observable in the combination of the 3ℓ and 4ℓ channels, absolute (top) and normalised (bottom), unfolded to particle-level (left) and parton-level (right).

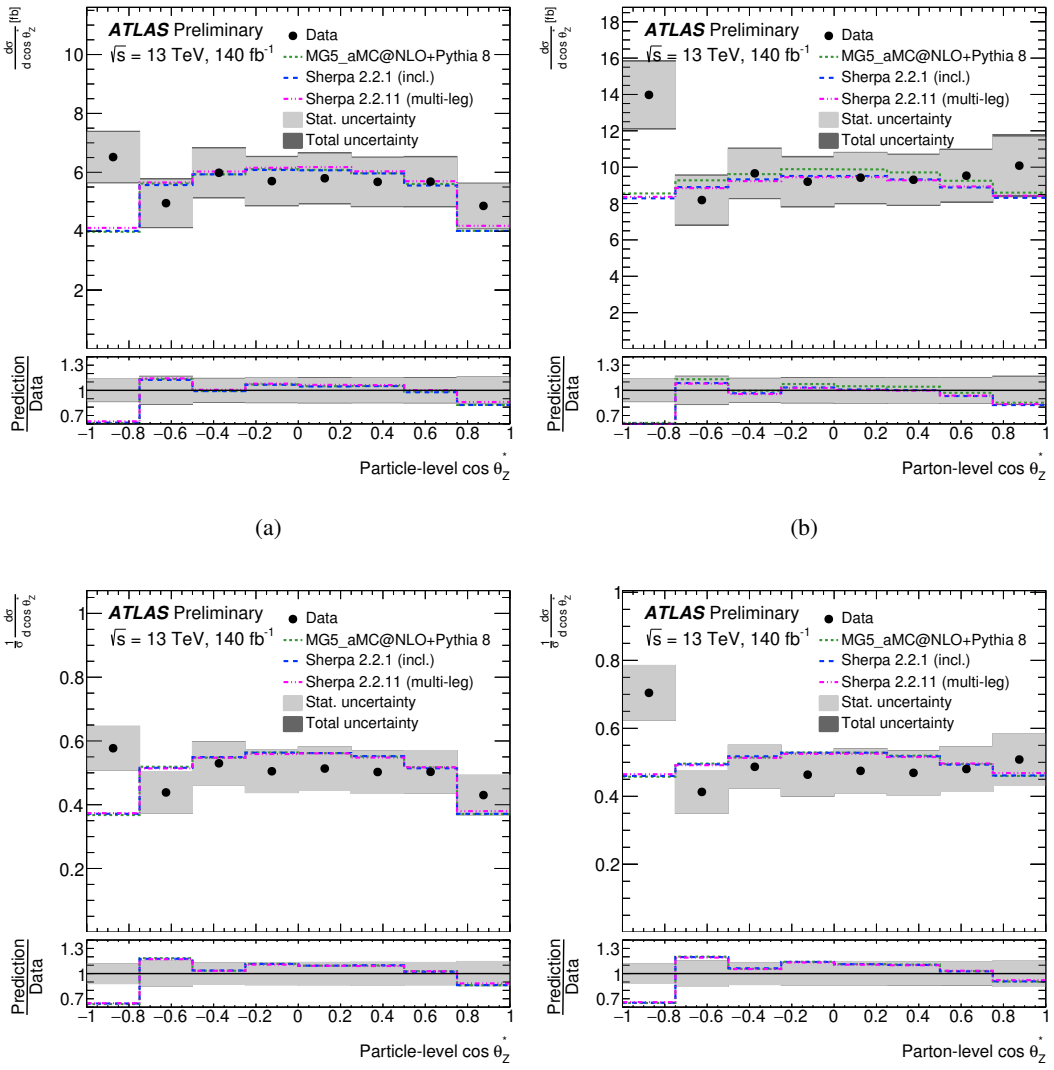

Figure 17: Cross section measurement of the $\cos\theta^*_Z$ observable in the combination of the 3ℓ and 4ℓ channels, absolute (top) and normalised (bottom), unfolded to particle-level (left) and parton-level (right).

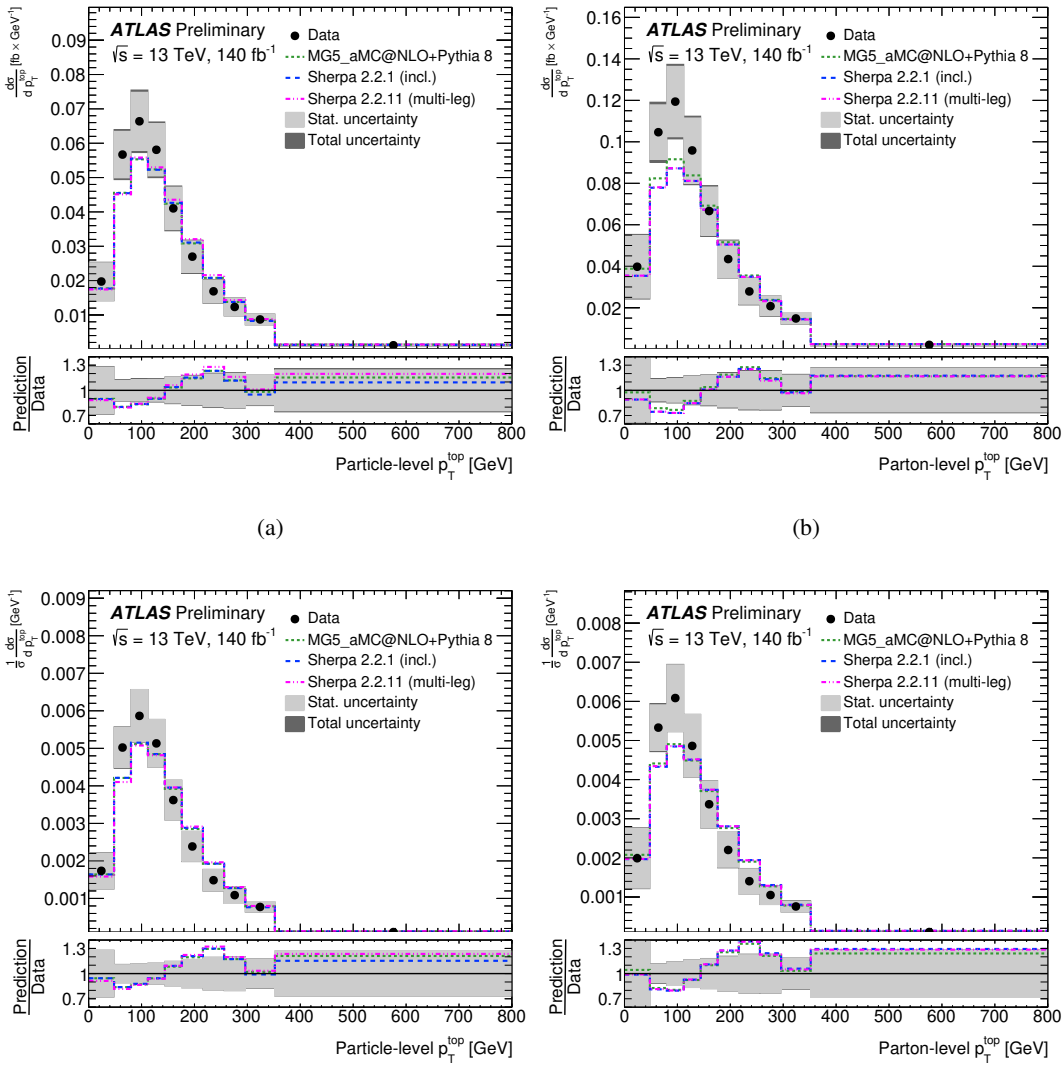

Figure 18: Cross section measurement of the p_{T}^{t} observable in the combination of the 3ℓ and 4ℓ channels, absolute (top) and normalised (bottom), unfolded to particle-level (left) and parton-level (right).

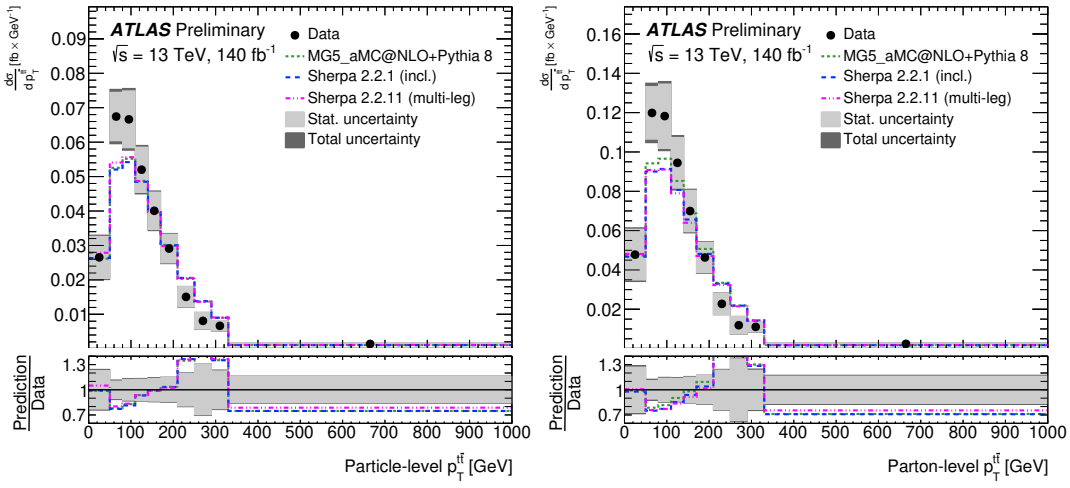

(a) (b)

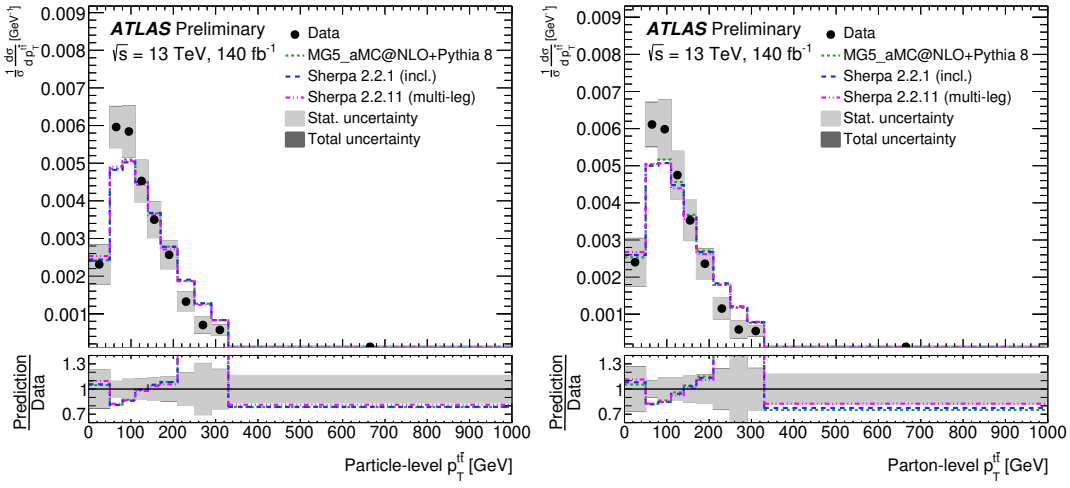

(c) (d)

Figure 19: Cross section measurement of the $p_{\mathrm{T}}^{t\bar{t}}$ observable in the combination of the 3ℓ and 4ℓ channels, absolute (top) and normalised (bottom), unfolded to particle-level (left) and parton-level (right).

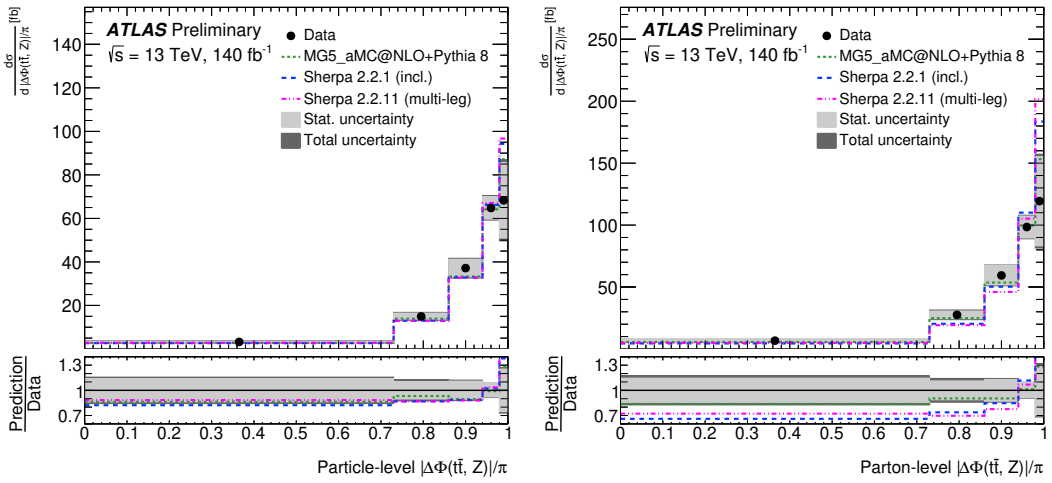

(a) (b)

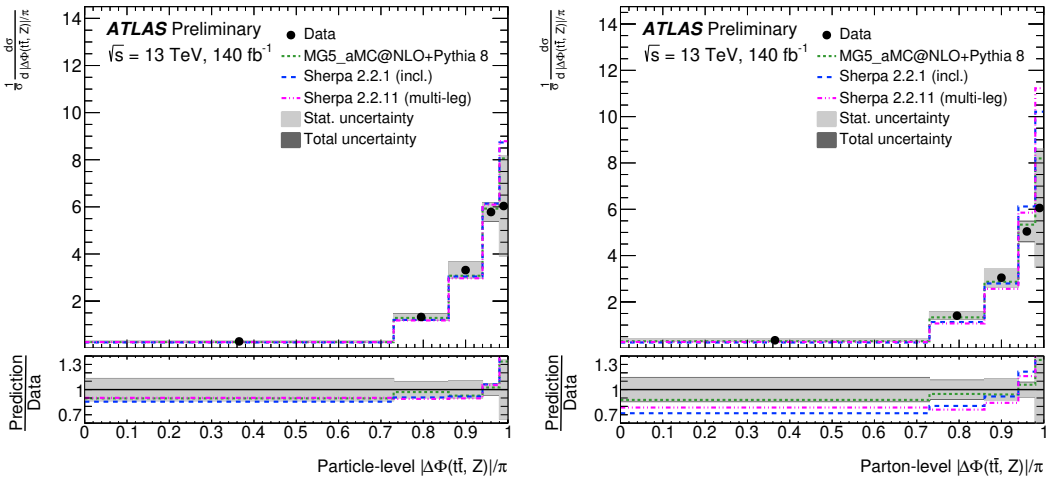

(c) (d)

Figure 20: Cross section measurement of the $|\Delta\phi(t\bar{t}, Z)|/\pi$ observable in the combination of the 3ℓ and 4ℓ channels, absolute (top) and normalised (bottom), unfolded to particle-level (left) and parton-level (right).

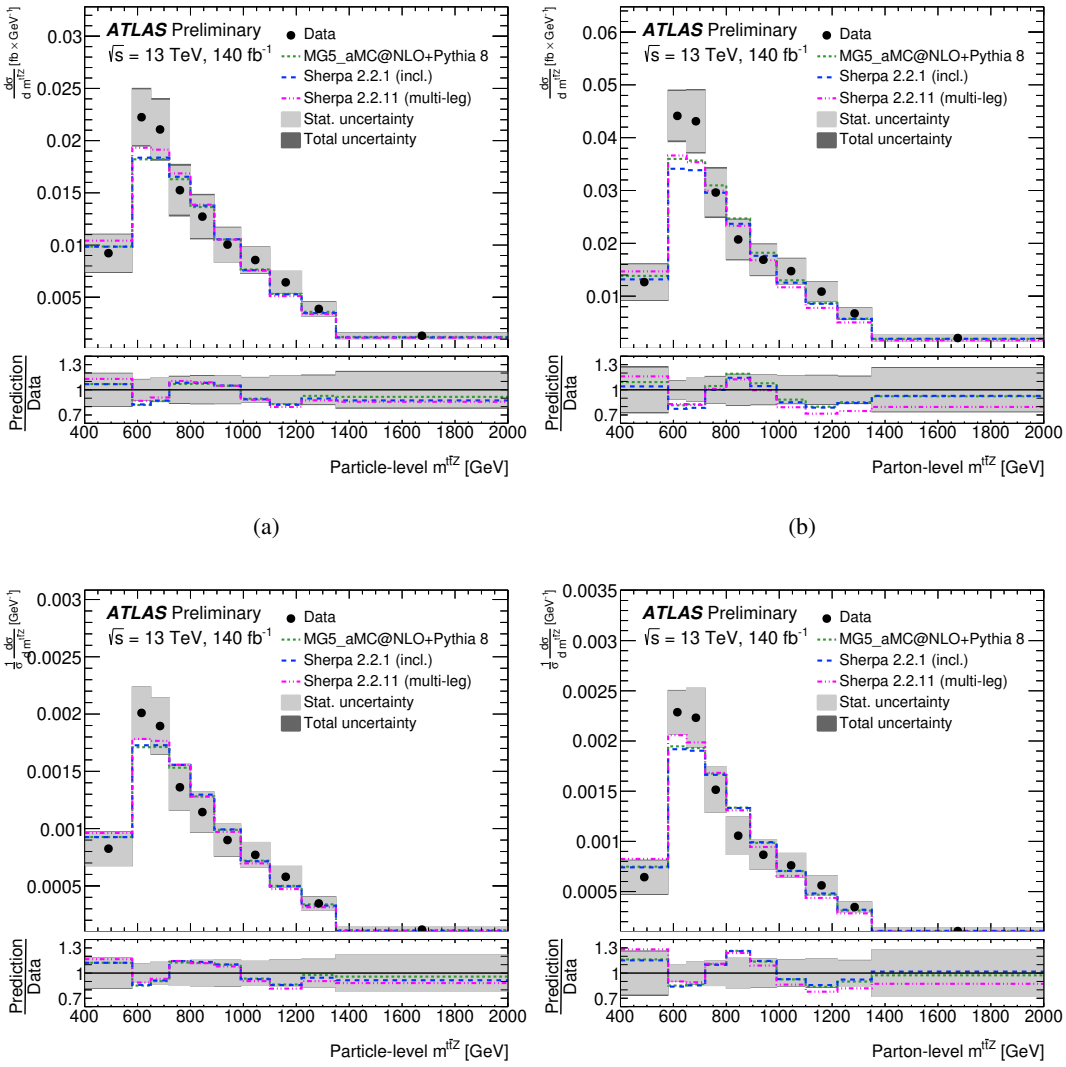

Figure 21: Cross section measurement of the $m^{t\bar{t}Z}$ observable in the combination of the 3ℓ and 4ℓ channels, absolute (top) and normalised (bottom), unfolded to particle-level (left) and parton-level (right).

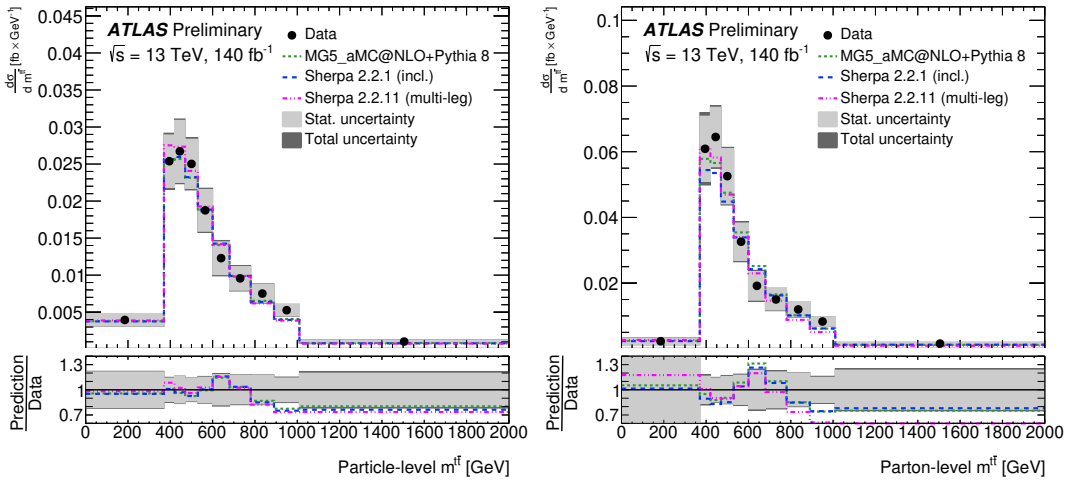

(a) (b)

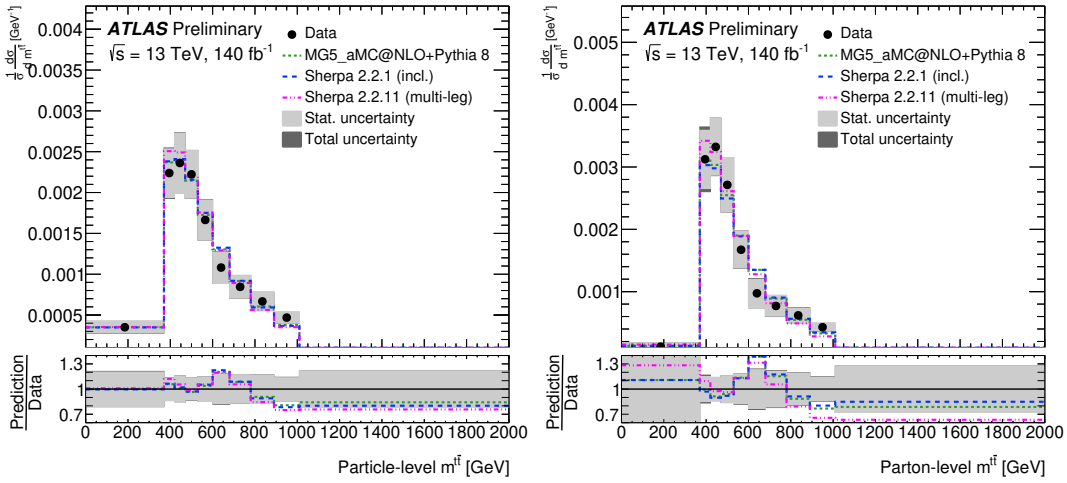

(c) (d)

Figure 22: Cross section measurement of the $m^{t\bar{t}}$ observable in the combination of the 3ℓ and 4ℓ channels, absolute (top) and normalised (bottom), unfolded to particle-level (left) and parton-level (right).

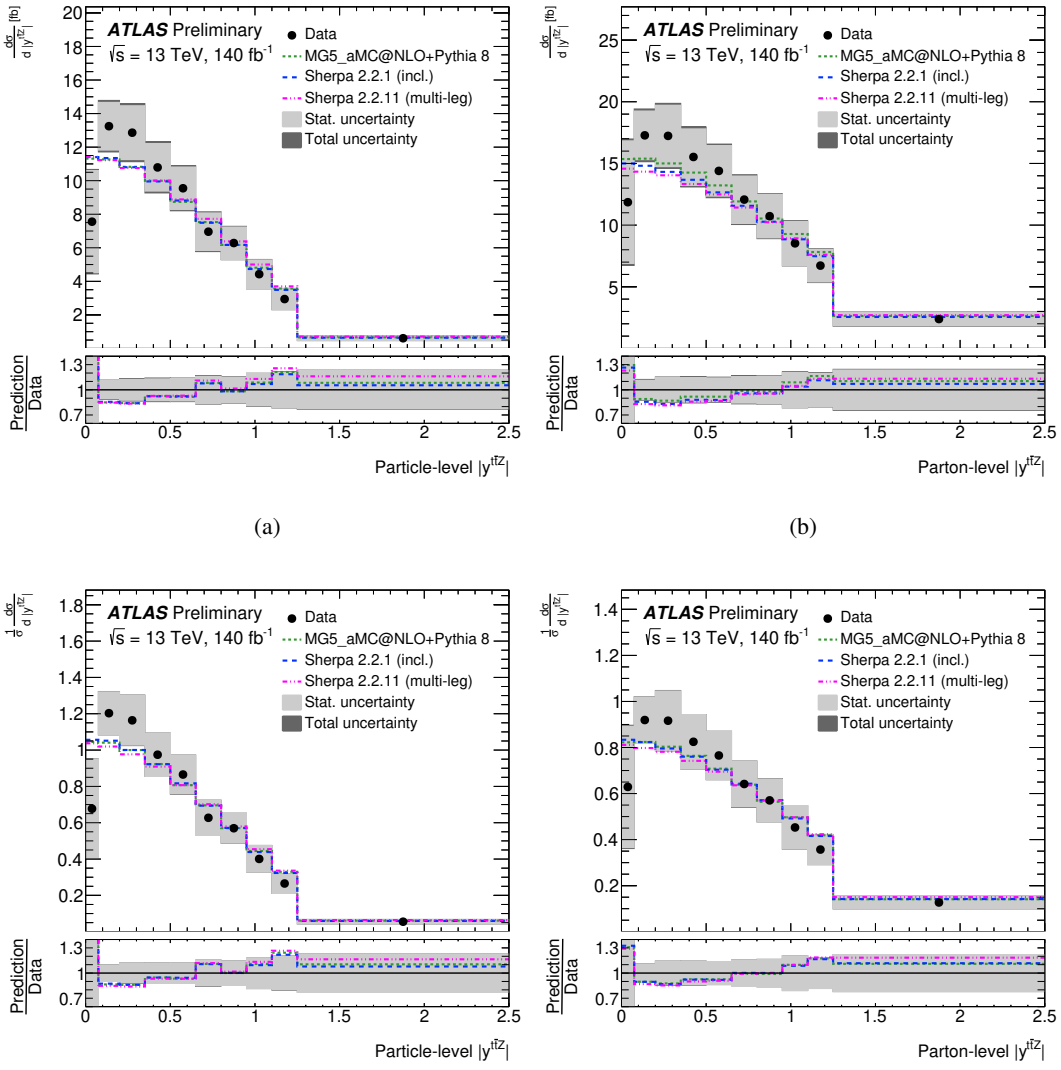

Figure 23: Cross section measurement of the $|y^{t\bar{t}Z}|$ observable in the combination of the 3ℓ and 4ℓ channels, absolute (top) and normalised (bottom), unfolded to particle-level (left) and parton-level (right).

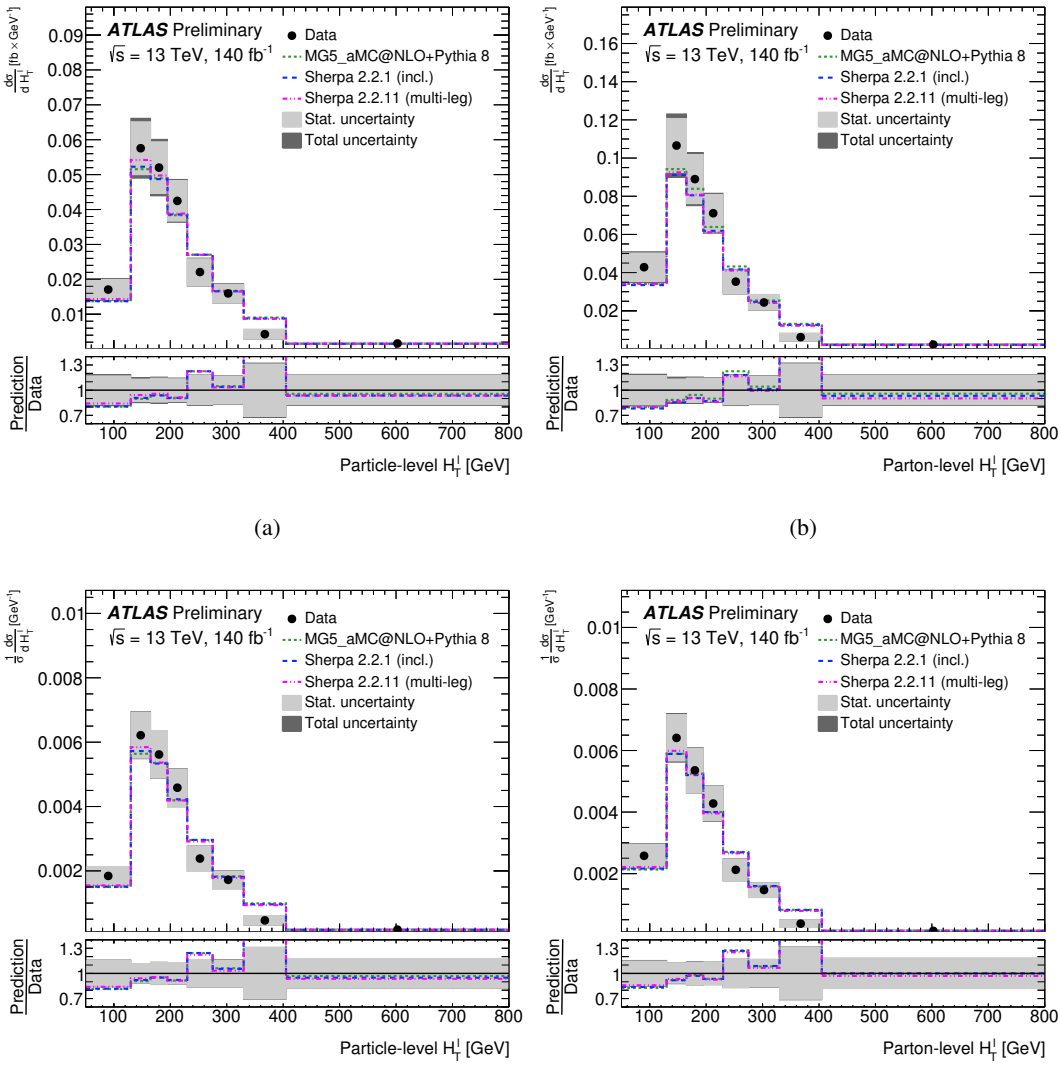

Figure 24: Cross section measurement of the $H_{\mathrm{T}}^{\mathrm{leptons}}$ observable in the 3ℓ channel, absolute (top) and normalised (bottom), unfolded to particle-level (left) and parton-level (right).

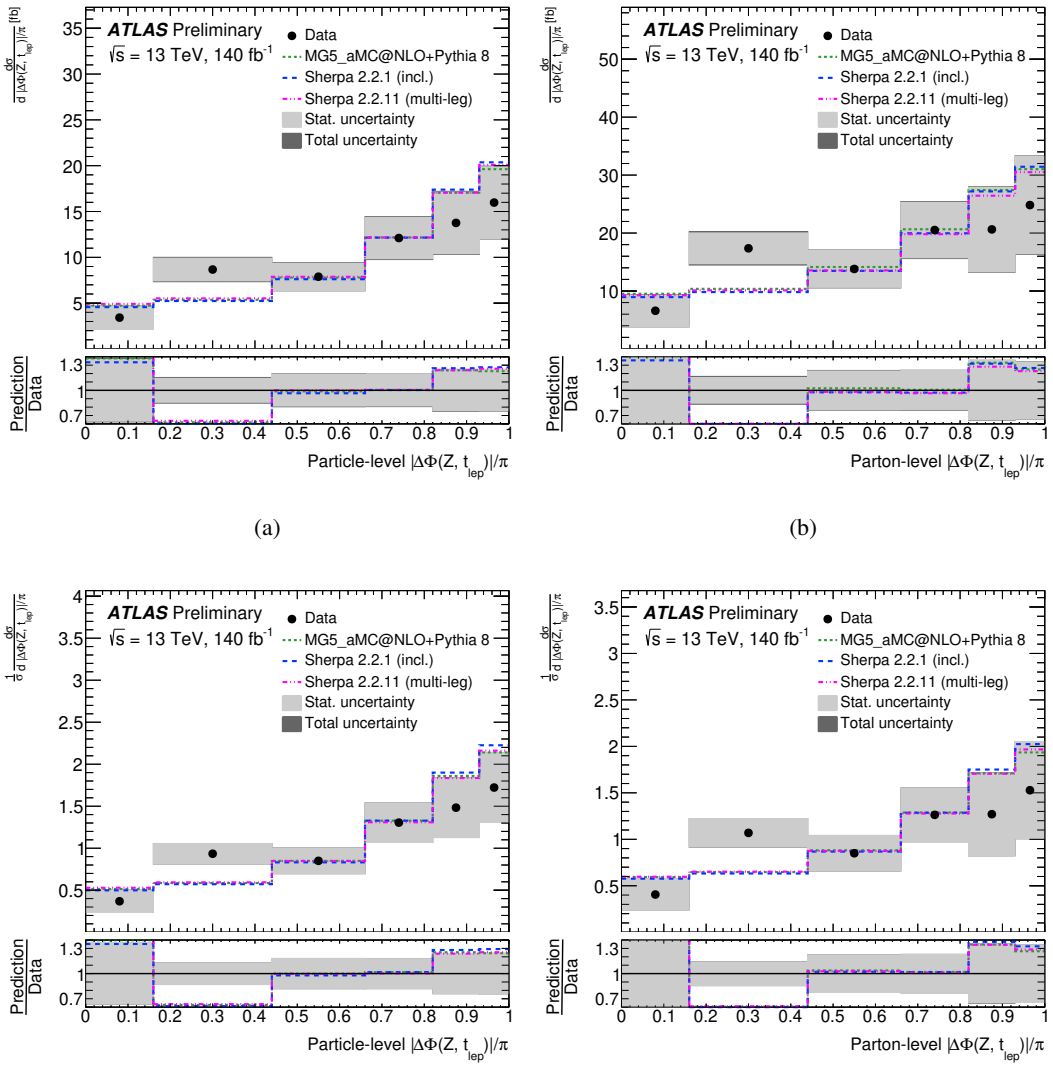

Figure 25: Cross section measurement of the $|\Delta\phi(Z, t_{\text{lep}})|/\pi$ observable in the 3ℓ channel, absolute (top) and normalised (bottom), unfolded to particle-level (left) and parton-level (right).

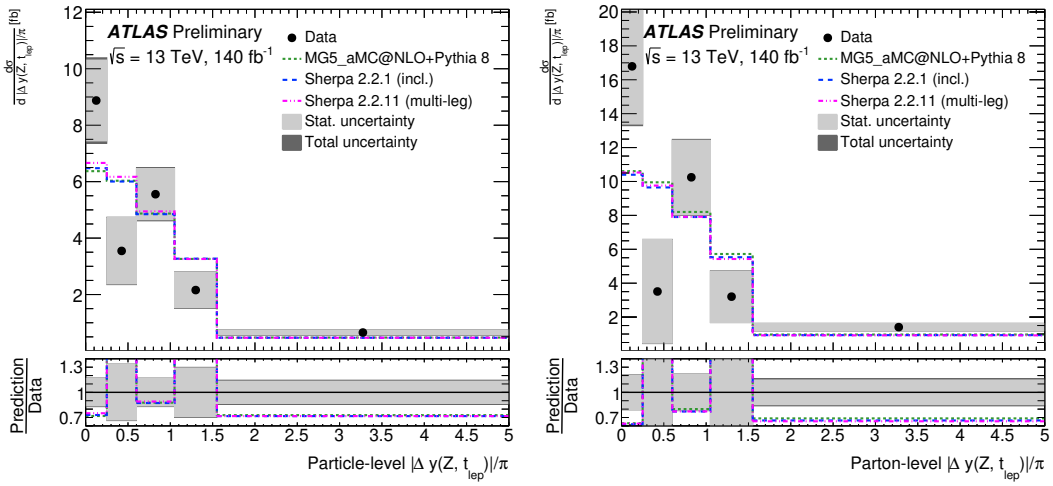

(a) (b)

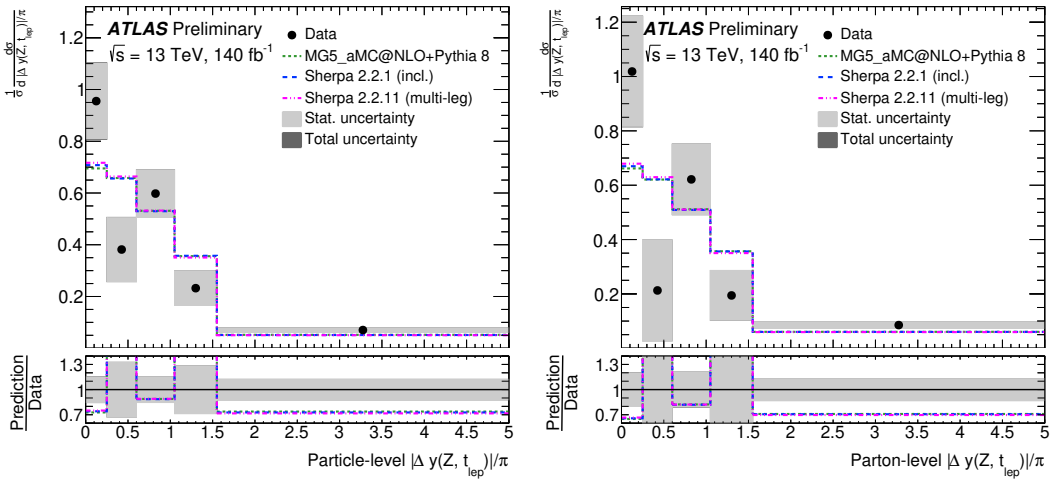

(c) (d)

Figure 26: Cross section measurement of the $|\Delta y(Z, t_{\text{lep}})|$ observable in the 3ℓ channel, absolute (top) and normalised (bottom), unfolded to particle-level (left) and parton-level (right).

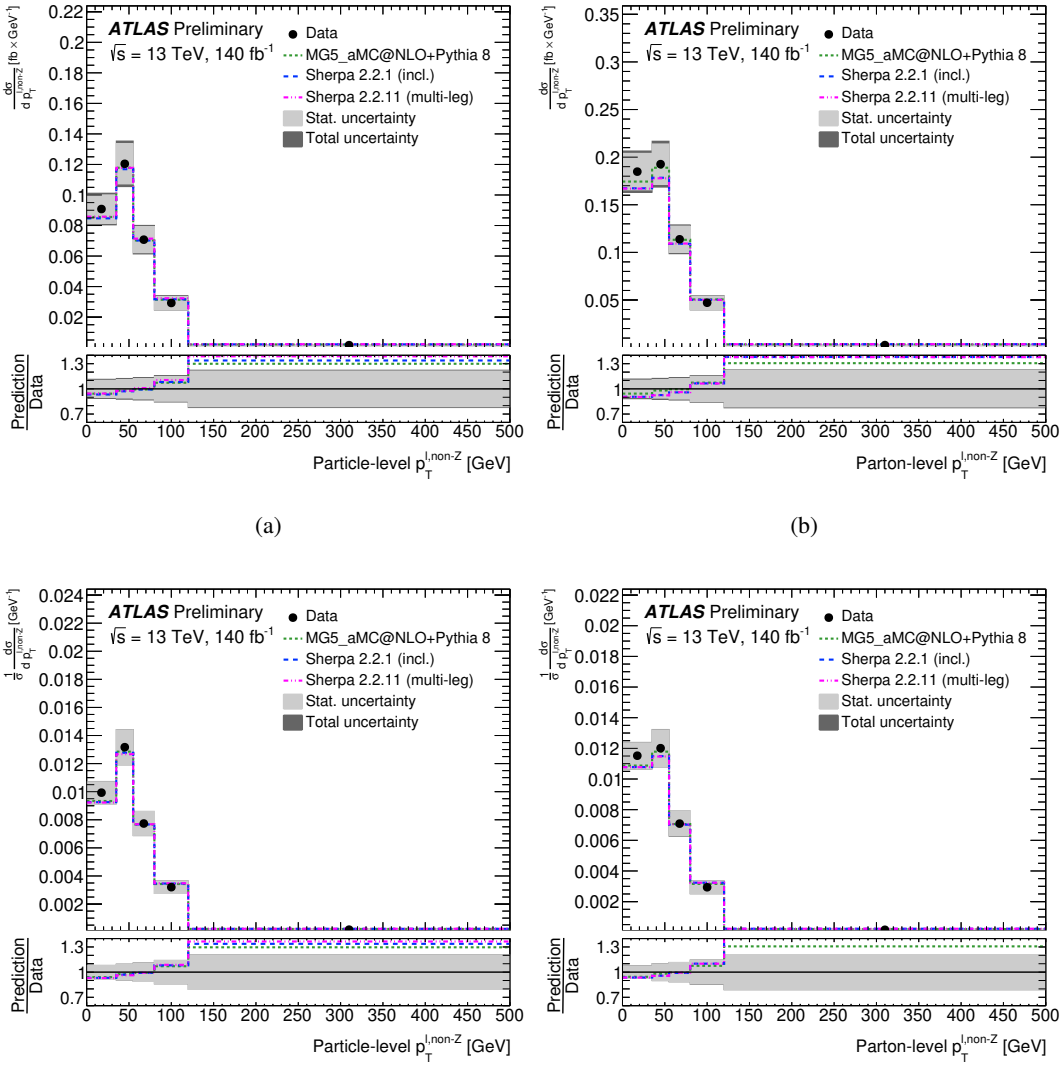

Figure 27: Cross section measurement of the $p_{\mathrm{T}}^{\ell,\mathrm{non-}Z}$ observable in the 3ℓ channel, absolute (top) and normalised (bottom), unfolded to particle-level (left) and parton-level (right).

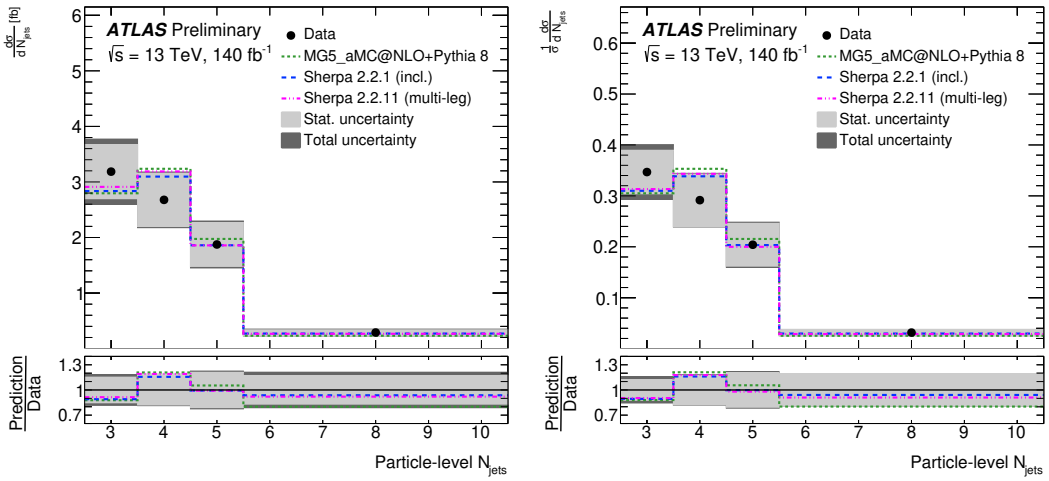

(a) (b)

Figure 28: Cross section measurement of the N_{jets} observable in the 3ℓ channel, unfolded to particle-level, absolute (left) and normalised (right).

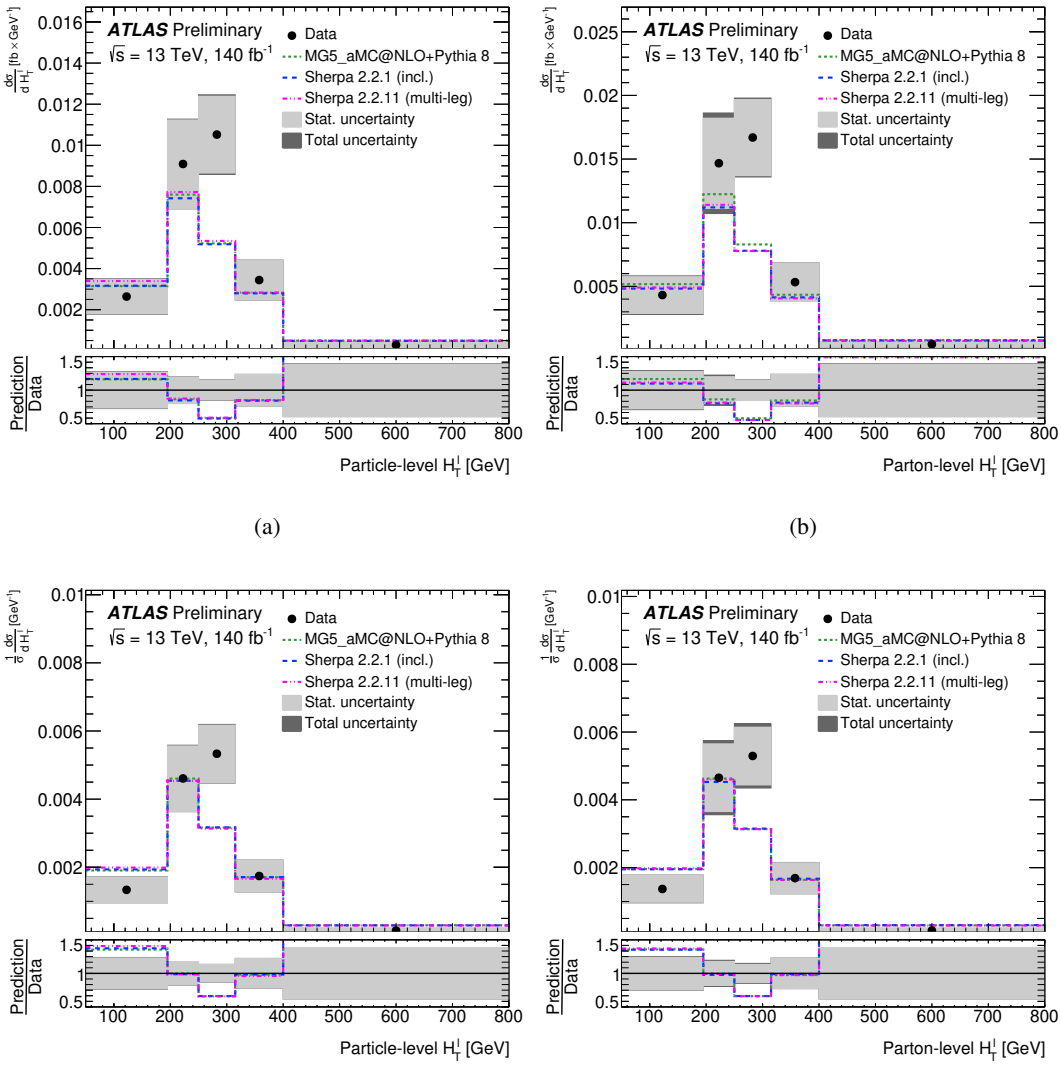

Figure 29: Cross section measurement of the H_{T}^{ℓ} observable in the 4ℓ channel, absolute (top) and normalised (bottom), unfolded to particle-level (left) and parton-level (right).

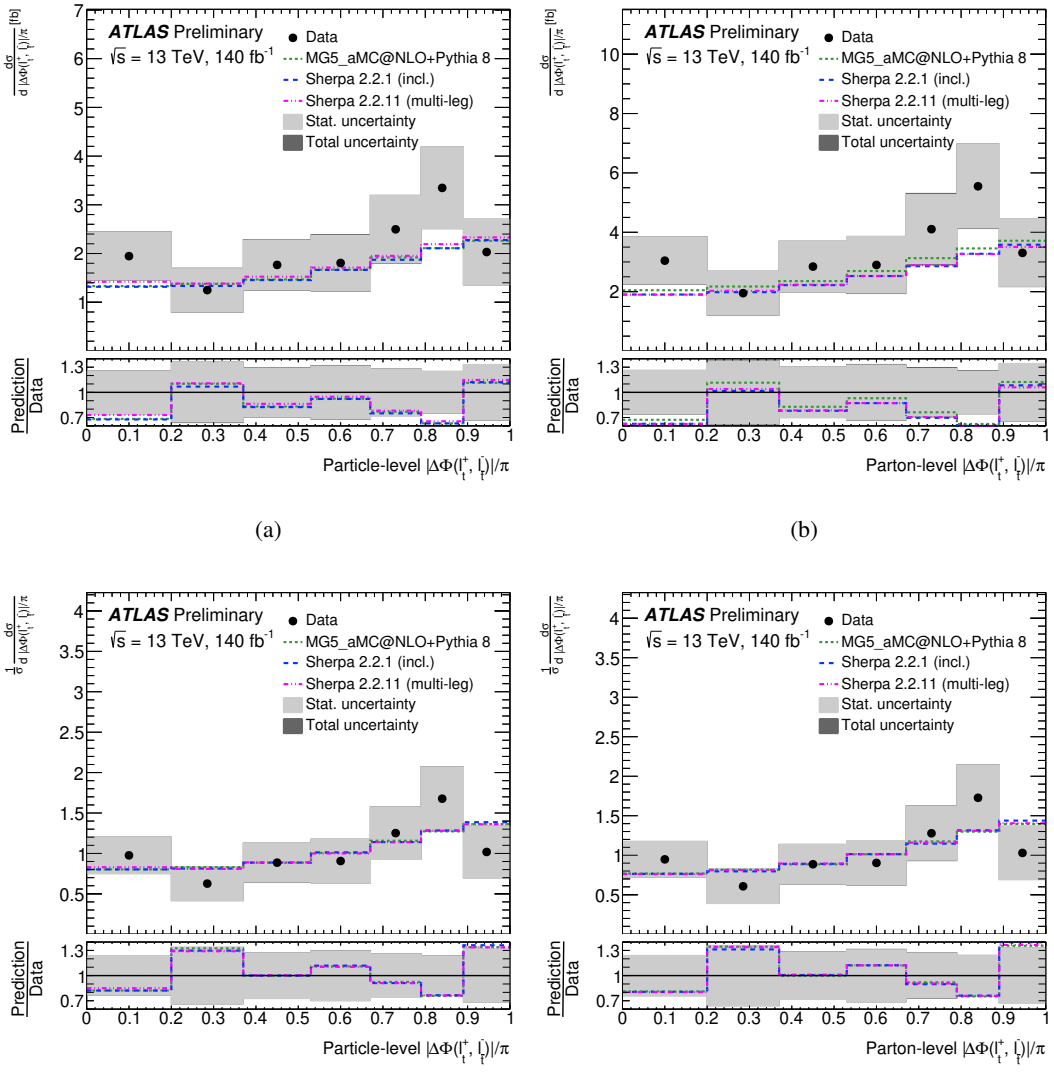

Figure 30: Cross section measurement of the $|\Delta\phi(\ell_t^+, \ell_{\bar{t}}^-)|$ observable in the 4ℓ channel, absolute (top) and normalised (bottom), unfolded to particle-level (left) and parton-level (right).

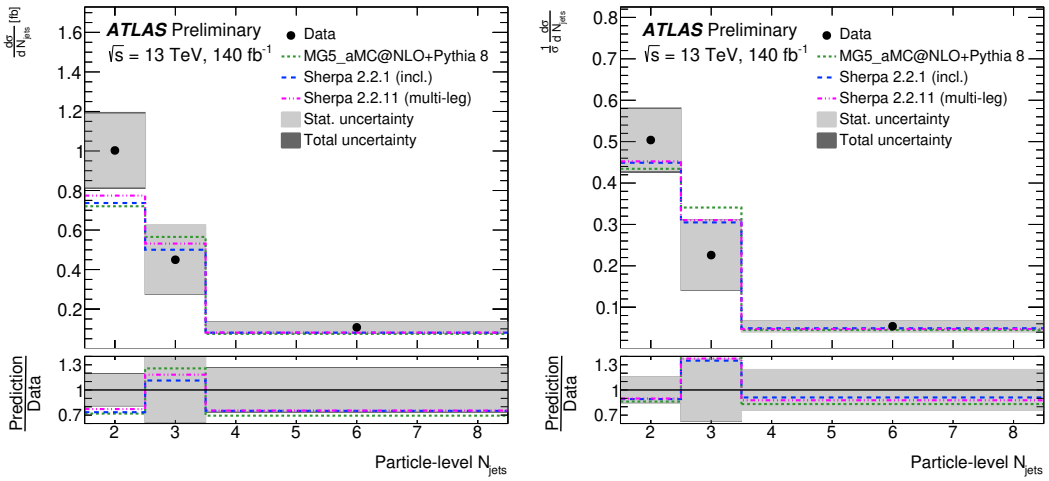

(a) (b)

Figure 31: Cross section measurement of the N_{jets} observable in the 4ℓ channel, unfolded to particle-level, absolute (left) and normalised (right).

Table 26: Summary of the compatibility tests, i.e. p-values, between the unfolded absolute differential spectra and the various predictions.

		aMC@NLO +Pythia 8		Sherpa 2.2.1 (incl.)		Sherpa 2.2.11 (multi-leg)	
	Variable	parton	particle	parton	particle	parton	particle
3ℓ	$\lvert\Delta\phi(Z,t^l)\rvert/\pi$	0.12	0.09	0.09	0.05	0.14	0.09
	$\lvert\Delta y(Z,t^l)\rvert$	0.08	0.05	0.09	0.05	0.08	0.04
	H_T^l	0.04	0.04	0.06	0.07	0.11	0.1
	$p_T^{l,non-Z}$	0.75	0.75	0.44	0.63	0.44	0.51
	N_{jets}	-	0.55	-	0.9	-	0.82
4ℓ	N_{jets}	-	0.36	-	0.43	-	0.55
	$\lvert\Delta\phi l,l\rvert/\pi$	0.68	0.67	0.52	0.65	0.52	0.77
	H_T^l	0.04	0.04	0.02	0.04	0.03	0.04
$3\ell+4\ell$	$\lvert y^Z\rvert$	0.77	0.78	0.70	0.77	0.64	0.77
	p_T^Z	0.09	0.08	0.13	0.13	0.22	0.23
	$\cos\theta*^Z$	0.20	0.17	0.21	0.19	0.24	0.22
	$\lvert\Delta\phi(t\bar{t},Z)\rvert/\pi$	0.84	0.82	0.08	0.53	0.07	0.56
	$m^{t\bar{t}}$	0.89	0.97	0.8	0.92	0.49	0.83
	$m^{t\bar{t}Z}$	0.86	0.93	0.64	0.91	0.58	0.91
	p_T^{top}	0.45	0.56	0.2	0.59	0.22	0.39
	$p_T^{t\bar{t}}$	0.09	0.07	0.05	0.05	0.07	0.1
	$\lvert y^{t\bar{t}Z}\rvert$	0.95	0.8	0.86	0.85	0.66	0.65

Table 27: Summary of the compatibility tests, i.e. p-values, between the unfolded normalised differential spectra and the various predictions.

		aMC@NLO +Pythia 8		Sherpa 2.2.1 (incl.)		Sherpa 2.2.11 (multi-leg)	
	Variable	parton	particle	parton	particle	parton	particle
3ℓ	$\lvert\Delta\phi(Z,t^l)\rvert/\pi$	0.07	0.05	0.04	0.02	0.07	0.06
	$\lvert\Delta y(Z,t^l)\rvert$	0.03	0.03	0.03	0.02	0.03	0.02
	H_T^l	0.02	0.02	0.02	0.04	0.05	0.07
	$p_T^{l,non-Z}$	0.63	0.63	0.29	0.5	0.29	0.41
	N_{jets}	-	0.42	-	0.81	-	0.75
4ℓ	N_{jets}	-	0.40	-	0.65	-	0.61
	$\lvert\Delta\phi l,l\rvert/\pi$	0.75	0.76	0.73	0.75	0.74	0.80
	H_T^l	0.03	0.02	0.03	0.02	0.03	0.02
$3\ell+4\ell$	$\lvert y^Z\rvert$	0.71	0.72	0.71	0.71	0.70	0.69
	p_T^Z	0.04	0.03	0.06	0.06	0.13	0.14
	$\cos\theta*^Z$	0.11	0.11	0.12	0.12	0.15	0.15
	$\lvert\Delta\phi(t\bar{t},Z)\rvert/\pi$	0.74	0.71	0.02	0.36	0.02	0.39
	$m^{t\bar{t}}$	0.79	0.88	0.87	0.73	0.27	0.43
	$m^{t\bar{t}Z}$	0.84	0.93	0.8	0.91	0.81	0.89
	p_T^{top}	0.03	0.23	0.01	0.29	0.01	0.1
	$p_T^{t\bar{t}}$	0.02	0.01	0.01	0.01	0.02	0.03
	$\lvert y^{t\bar{t}Z}\rvert$	0.87	0.52	0.85	0.64	0.59	0.28

References

[1] ATLAS Collaboration, *Measurement of the top quark mass in the $t\bar{t} \to$ lepton+jets channel from $\sqrt{s} = 8$ TeV ATLAS data and combination with previous results*, Eur. Phys. J. C **79** (2019) 290, arXiv: 1810.01772 [hep-ex] (cit. on p. 2).

[2] R. S. Chivukula, S. B. Selipsky and E. H. Simmons, *Nonoblique effects in the $Zb\bar{b}$ vertex from extended technicolor dynamics*, Phys. Rev. Lett. **69** (1992) 575, arXiv: hep-ph/9204214 (cit. on p. 2).

[3] R. S. Chivukula, E. H. Simmons and J. Terning, *A heavy top quark and the Zbb vertex in non-commuting extended technicolor*, Phys. Lett. B **331** (1994) 383, arXiv: hep-ph/9404209 (cit. on p. 2).

[4] K. Hagiwara and N. Kitazawa, *Extended technicolor contribution to the Zbb vertex*, Phys. Rev. D **52** (1995) 5374, arXiv: hep-ph/9504332 (cit. on p. 2).

[5] U. Mahanta, *Noncommuting ETC corrections to $Zt\bar{t}$ vertex*, Phys. Rev. D **55** (1997) 5848, arXiv: hep-ph/9611289 (cit. on p. 2).

[6] U. Mahanta,
Probing noncommuting extended technicolor effects by $e^+e^- \to t\bar{t}$ at the Next Linear Collider,
Phys. Rev. D **56** (1997) 402 (cit. on p. 2).

[7] M. Perelstein, *Little Higgs models and their phenomenology*,
Prog. Part. Nucl. Phys. **58** (2007) 247, arXiv: hep-ph/0512128 (cit. on p. 2).

[8] ATLAS Collaboration,
Observation of four-top-quark production in the multilepton final state with the ATLAS detector,
Eur. Phys. J. C **83** (2023), arXiv: 2303.15061 [hep-ex] (cit. on p. 2).

[9] CMS Collaboration,
Observation of four top quark production in proton-proton collisions at $\sqrt{s}$ =13 TeV,
arXiv: 2305.13439 [hep-ex] (cit. on p. 2).

[10] ATLAS Collaboration, *Search for direct top squark pair production in events with a Higgs or Z boson, and missing transverse momentum in $\sqrt{s}$ = 13 TeV pp collisions with the ATLAS detector*,
JHEP **08** (2017) 006, arXiv: 1706.03986 [hep-ex] (cit. on p. 2).

[11] ATLAS Collaboration, *Search for new phenomena in events with same-charge leptons and b-jets in pp collisions at $\sqrt{s}$ = 13 TeV with the ATLAS detector*, JHEP **12** (2018) 039,
arXiv: 1807.11883 [hep-ex] (cit. on p. 2).

[12] ATLAS Collaboration, *Search for squarks and gluinos in final states with same-sign leptons and jets using 139 fb^{-1} of data collected with the ATLAS detector*, JHEP **06** (2020) 046,
arXiv: 1909.08457 [hep-ex] (cit. on p. 2).

[13] CMS Collaboration, *Search for physics beyond the standard model in events with two leptons of same sign, missing transverse momentum, and jets in proton–proton collisions at $\sqrt{s}$ = 13 TeV*,
Eur. Phys. J. C **77** (2017) 578, arXiv: 1704.07323 [hep-ex] (cit. on p. 2).

[14] ATLAS Collaboration, *Evidence for the associated production of the Higgs boson and a top quark pair with the ATLAS detector*, Phys. Rev. D **97** (2018) 072003, arXiv: 1712.08891 [hep-ex]
(cit. on pp. 2, 8).

[15] ATLAS Collaboration, *Observation of Higgs boson production in association with a top quark pair at the LHC with the ATLAS detector*, Phys. Lett. B **784** (2018) 173,
arXiv: 1806.00425 [hep-ex] (cit. on p. 2).

[16] CMS Collaboration, *Measurement of the Higgs boson production rate in association with top quarks in final states with electrons, muons, and hadronically decaying tau leptons at $\sqrt{s}$ = 13 TeV*,
Eur. Phys. J. C **81** (2020) 378, arXiv: 2011.03652 [hep-ex] (cit. on p. 2).

[17] ATLAS Collaboration, *Observation of the associated production of a top quark and a Z boson in pp collisions at $\sqrt{s}$ = 13 TeV with the ATLAS detector*, JHEP **07** (2020) 124,
arXiv: 2002.07546 [hep-ex] (cit. on pp. 2, 22).

[18] CMS Collaboration, *Inclusive and differential cross section measurements of single top quark production in association with a Z boson in proton–proton collisions at $\sqrt{s}$ = 13 TeV*,
JHEP **02** (2021) 107, arXiv: 2111.02860 [hep-ex] (cit. on p. 2).

[19] D. de Florian et al.,
Handbook of LHC Higgs Cross Sections: 4. Deciphering the Nature of the Higgs Sector, (2016),
arXiv: 1610.07922 [hep-ph] (cit. on pp. 2, 7, 23, 51).

[20] A. Kulesza, L. Motyka, D. Schwartländer, T. Stebel and V. Theeuwes, *Associated production of a top quark pair with a heavy electroweak gauge boson at NLO+NNLL accuracy*, Eur. Phys. J. C **79** (2019) 249, arXiv: 1812.08622 [hep-ph] (cit. on pp. 2, 25, 51).

[21] A. Broggio et al., *Top-quark pair hadroproduction in association with a heavy boson at NLO+NNLL including EW corrections*, JHEP **08** (2019) 039, arXiv: 1907.04343 [hep-ph] (cit. on pp. 2, 51).

[22] CMS Collaboration, *Measurement of top quark pair production in association with a Z boson in proton-proton collisions at $\sqrt{s}$ = 13 TeV*, JHEP **03** (2020) 056, arXiv: 1907.11270 [hep-ex] (cit. on pp. 2, 23).

[23] ATLAS Collaboration, *Measurements of the inclusive and differential production cross sections of a top-quark-antiquark pair in association with a Z boson at $\sqrt{s}$ = 13 TeV with the ATLAS detector*, Eur. Phys. J. C **81** (2021) 737, arXiv: 2103.12603 [hep-ex] (cit. on pp. 2, 3, 9, 14, 23, 25, 51).

[24] I. Brivio and M. Trott, *The Standard Model as an Effective Field Theory*, Phys. Rept. **793** (2019) 1, arXiv: 1706.08945 [hep-ph] (cit. on pp. 3, 42).

[25] I. Brivio, *SMEFTsim 3.0 — a practical guide*, JHEP **04** (2021) 073, arXiv: 2012.11343 [hep-ph] (cit. on pp. 3, 7, 42, 43).

[26] B. Ravina, E. Simpson and J. Howarth, *Observing $t\bar{t}Z$ spin correlations at the LHC*, Eur. Phys. J. C **81** (2021) 809, arXiv: 2106.09690 [hep-ph] (cit. on pp. 3, 40, 41).

[27] ATLAS Collaboration, *The ATLAS Experiment at the CERN Large Hadron Collider*, JINST **3** (2008) S08003 (cit. on p. 3).

[28] ATLAS Collaboration, *ATLAS Insertable B-Layer: Technical Design Report*, ATLAS-TDR-19; CERN-LHCC-2010-013, 2010, URL: https://cds.cern.ch/record/1291633 (cit. on p. 3), Addendum: ATLAS-TDR-19-ADD-1; CERN-LHCC-2012-009, 2012, URL: https://cds.cern.ch/record/1451888.

[29] B. Abbott et al., *Production and integration of the ATLAS Insertable B-Layer*, JINST **13** (2018) T05008, arXiv: 1803.00844 [physics.ins-det] (cit. on p. 3).

[30] ATLAS Collaboration, *Performance of the ATLAS trigger system in 2015*, Eur. Phys. J. C **77** (2017) 317, arXiv: 1611.09661 [hep-ex] (cit. on p. 4).

[31] ATLAS Collaboration, *The ATLAS Collaboration Software and Firmware*, ATL-SOFT-PUB-2021-001, 2021, URL: https://cds.cern.ch/record/2767187 (cit. on p. 4).

[32] ATLAS Collaboration, *Luminosity determination in pp collisions at $\sqrt{s}$ = 13 TeV using the ATLAS detector at the LHC*, (2022), arXiv: 2212.09379 [hep-ex] (cit. on pp. 4, 21).

[33] G. Avoni et al., *The new LUCID-2 detector for luminosity measurement and monitoring in ATLAS*, JINST **13** (2018) P07017 (cit. on p. 4).

[34] ATLAS Collaboration, *Performance of electron and photon triggers in ATLAS during LHC Run 2*, Eur. Phys. J. C **80** (2020) 47, arXiv: 1909.00761 [hep-ex] (cit. on pp. 4, 8).

[35] ATLAS Collaboration, *Performance of the ATLAS muon triggers in Run 2*, JINST **15** (2020) P09015, arXiv: 2004.13447 [hep-ex] (cit. on pp. 4, 8).

[36] ATLAS Collaboration, *2015 start-up trigger menu and initial performance assessment of the ATLAS trigger using Run-2 data*, ATL-DAQ-PUB-2016-001, 2016, URL: https://cds.cern.ch/record/2136007 (cit. on p. 4).

[37] ATLAS Collaboration, *Trigger Menu in 2016*, ATL-DAQ-PUB-2017-001, 2017, URL: https://cds.cern.ch/record/2242069 (cit. on p. 4).

[38] ATLAS Collaboration, *Trigger Menu in 2017*, ATL-DAQ-PUB-2018-002, 2018, URL: https://cds.cern.ch/record/2625986 (cit. on p. 4).

[39] T. Sjöstrand, S. Mrenna and P. Skands, *A brief introduction to PYTHIA 8.1*, Comput. Phys. Commun. **178** (2008) 852, arXiv: 0710.3820 [hep-ph] (cit. on p. 4).

[40] NNPDF Collaboration, R. D. Ball et al., *Parton distributions with LHC data*, Nucl. Phys. B **867** (2013) 244, arXiv: 1207.1303 [hep-ph] (cit. on p. 4).

[41] ATLAS Collaboration, *The Pythia 8 A3 tune description of ATLAS minimum bias and inelastic measurements incorporating the Donnachie–Landshoff diffractive model*, ATL-PHYS-PUB-2016-017, 2016, URL: https://cds.cern.ch/record/2206965 (cit. on p. 4).

[42] ATLAS Collaboration, *The ATLAS Simulation Infrastructure*, Eur. Phys. J. C **70** (2010) 823, arXiv: 1005.4568 [physics.ins-det] (cit. on p. 4).

[43] S. Agostinelli et al., *GEANT4 — a simulation toolkit*, Nucl. Instr. Meth. **A 506** (2003) 250 (cit. on p. 4).

[44] ATLAS Collaboration, *The simulation principle and performance of the ATLAS fast calorimeter simulation FastCaloSim*, ATL-PHYS-PUB-2010-013, 2010, URL: https://cds.cern.ch/record/1300517 (cit. on p. 4).

[45] J. Alwall et al., *The automated computation of tree-level and next-to-leading order differential cross sections, and their matching to parton shower simulations*, JHEP **07** (2014) 079, arXiv: 1405.0301 [hep-ph] (cit. on p. 4).

[46] The NNPDF Collaboration, R. D. Ball et al., *Parton distributions for the LHC run II*, JHEP **04** (2015) 040, arXiv: 1410.8849 [hep-ph] (cit. on p. 4).

[47] S. Frixione, E. Laenen, P. Motylinski and B. R. Webber, *Angular correlations of lepton pairs from vector boson and top quark decays in Monte Carlo simulations*, JHEP **04** (2007) 081, arXiv: hep-ph/0702198 (cit. on p. 4).

[48] P. Artoisenet, R. Frederix, O. Mattelaer and R. Rietkerk, *Automatic spin-entangled decays of heavy resonances in Monte Carlo simulations*, JHEP **03** (2013) 015, arXiv: 1212.3460 [hep-ph] (cit. on p. 4).

[49] T. Sjöstrand et al., *An introduction to PYTHIA 8.2*, Comput. Phys. Commun. **191** (2015) 159, arXiv: 1410.3012 [hep-ph] (cit. on p. 5).

[50] ATLAS Collaboration, *ATLAS Pythia 8 tunes to 7 TeV data*, ATL-PHYS-PUB-2014-021, 2014, URL: https://cds.cern.ch/record/1966419 (cit. on p. 5).

[51] D. J. Lange, *The EvtGen particle decay simulation package*, Nucl. Instrum. Meth. A **462** (2001) 152 (cit. on p. 5).

[52] M. Bähr et al., *Herwig++ physics and manual*, Eur. Phys. J. C **58** (2008) 639, arXiv: 0803.0883 [hep-ph] (cit. on p. 5).

[53] J. Bellm et al., *Herwig 7.0/Herwig++ 3.0 release note*, Eur. Phys. J. C **76** (2016) 196, arXiv: 1512.01178 [hep-ph] (cit. on p. 5).

[54] ATLAS Collaboration, *Modelling of the $t\bar{t}H$ and $t\bar{t}V(V = W, Z)$ processes for $\sqrt{s} = 13$ TeV ATLAS analyses*, ATL-PHYS-PUB-2016-005, 2016, URL: https://cds.cern.ch/record/2120826 (cit. on pp. 5, 7).

[55] E. Bothmann et al., *Event generation with Sherpa 2.2*, SciPost Phys. **7** (2019) 034, arXiv: 1905.09127 [hep-ph] (cit. on p. 5).

[56] S. Catani, F. Krauss, B. R. Webber and R. Kuhn, *QCD Matrix Elements + Parton Showers*, JHEP **11** (2001) 063, arXiv: hep-ph/0109231 (cit. on pp. 5, 6).

[57] S. Höche, F. Krauss, S. Schumann and F. Siegert, *QCD matrix elements and truncated showers*, JHEP **05** (2009) 053, arXiv: 0903.1219 [hep-ph] (cit. on pp. 5, 6).

[58] S. Höche, F. Krauss, M. Schönherr and F. Siegert, *QCD matrix elements + parton showers. The NLO case*, JHEP **04** (2013) 027, arXiv: 1207.5030 [hep-ph] (cit. on pp. 5, 6).

[59] F. Demartin, B. Maier, F. Maltoni, K. Mawatari and M. Zaro, *tWH associated production at the LHC*, Eur. Phys. J. C **77** (2017) 34, arXiv: 1607.05862 [hep-ph] (cit. on pp. 5, 22).

[60] S. Alioli, P. Nason, C. Oleari and E. Re, *A general framework for implementing NLO calculations in shower Monte Carlo programs: the POWHEG BOX*, JHEP **06** (2010) 043, arXiv: 1002.2581 [hep-ph] (cit. on p. 6).

[61] T. Gleisberg and S. Höche, *Comix, a new matrix element generator*, JHEP **12** (2008) 039, arXiv: 0808.3674 [hep-ph] (cit. on p. 6).

[62] S. Schumann and F. Krauss, *A parton shower algorithm based on Catani–Seymour dipole factorisation*, JHEP **03** (2008) 038, arXiv: 0709.1027 [hep-ph] (cit. on p. 6).

[63] S. Höche, F. Krauss, M. Schönherr and F. Siegert, *A critical appraisal of NLO+PS matching methods*, JHEP **09** (2012) 049, arXiv: 1111.1220 [hep-ph] (cit. on p. 6).

[64] F. Cascioli, P. Maierhöfer and S. Pozzorini, *Scattering Amplitudes with Open Loops*, Phys. Rev. Lett. **108** (2012) 111601, arXiv: 1111.5206 [hep-ph] (cit. on p. 6).

[65] A. Denner, S. Dittmaier and L. Hofer, *COLLIER: A fortran-based complex one-loop library in extended regularizations*, Comput. Phys. Commun. **212** (2017) 220, arXiv: 1604.06792 [hep-ph] (cit. on p. 6).

[66] F. Buccioni et al., *OpenLoops 2*, Eur. Phys. J. C **79** (2019) 866, arXiv: 1907.13071 [hep-ph] (cit. on p. 6).

[67] C. Anastasiou, L. Dixon, K. Melnikov and F. Petriello, *High-precision QCD at hadron colliders: Electroweak gauge boson rapidity distributions at next-to-next-to leading order*, Phys. Rev. D **69** (2004) 094008, arXiv: hep-ph/0312266 (cit. on pp. 6, 7).

[68] R. Frederix and I. Tsinikos, *On improving NLO merging for $t\bar{t}W$ production*, JHEP **11** (2021) 029, arXiv: 2108.07826 [hep-ph] (cit. on p. 7).

[69] LHCTopWG, *NNLO+NNLL top-quark-pair cross sections*, 2015, URL: https://twiki.cern.ch/twiki/bin/view/LHCPhysics/TtbarNNLO (cit. on p. 7).

[70] R. Frederix, D. Pagani and M. Zaro, *Large NLO corrections in $t\bar{t}W^{\pm}$ and $t\bar{t}t\bar{t}$ hadroproduction from supposedly subleading EW contributions*, JHEP **02** (2018) 031, arXiv: 1711.02116 [hep-ph] (cit. on p. 7).

[71] M. L. Ciccolini, S. Dittmaier and M. Krämer, *Electroweak radiative corrections to associated WH and ZH production at hadron colliders*, Phys. Rev. D **68** (2003) 073003, arXiv: hep-ph/0306234 [hep-ph] (cit. on p. 7).

[72] O. Brein, A. Djouadi and R. Harlander, *NNLO QCD corrections to the Higgs-strahlung processes at hadron colliders*, Phys. Lett. B **579** (2004) 149, arXiv: hep-ph/0307206 (cit. on p. 7).

[73] O. Brein, R. V. Harlander, M. Wiesemann and T. Zirke, *Top-quark mediated effects in hadronic Higgs-Strahlung*, Eur. Phys. J. C **72** (2012) 1868, arXiv: 1111.0761 [hep-ph] (cit. on p. 7).

[74] L. Altenkamp, S. Dittmaier, R. V. Harlander, H. Rzehak and T. J. E. Zirke, *Gluon-induced Higgs-strahlung at next-to-leading order QCD*, JHEP **02** (2013) 078, arXiv: 1211.5015 [hep-ph] (cit. on p. 7).

[75] A. Denner, S. Dittmaier, S. Kallweit and A. Mück, *HAWK 2.0: A Monte Carlo program for Higgs production in vector-boson fusion and Higgs strahlung at hadron colliders*, Comput. Phys. Commun. **195** (2015) 161, arXiv: 1412.5390 [hep-ph] (cit. on p. 7).

[76] O. Brein, R. V. Harlander and T. J. E. Zirke, *vh@nnlo – Higgs Strahlung at hadron colliders*, Comput. Phys. Commun. **184** (2013) 998, arXiv: 1210.5347 [hep-ph] (cit. on p. 7).

[77] R. V. Harlander, A. Kulesza, V. Theeuwes and T. Zirke, *Soft gluon resummation for gluon-induced Higgs Strahlung*, JHEP **11** (2014) 082, arXiv: 1410.0217 [hep-ph] (cit. on p. 7).

[78] C. Degrande et al., *UFO - The Universal FeynRules Output*, Comput. Phys. Commun. **183** (2012) 1201, arXiv: 1108.2040 [hep-ph] (cit. on p. 7).

[79] A. Alloul, N. D. Christensen, C. Degrande, C. Duhr and B. Fuks, *FeynRules 2.0 - A complete toolbox for tree-level phenomenology*, Comput. Phys. Commun. **185** (2014) 2250, arXiv: 1310.1921 [hep-ph] (cit. on p. 7).

[80] I. Brivio et al., *Electroweak input parameters*, (2021), arXiv: 2111.12515 [hep-ph] (cit. on p. 7).

[81] ATLAS Collaboration, *Electron reconstruction and identification in the ATLAS experiment using the 2015 and 2016 LHC proton–proton collision data at $\sqrt{s} = 13$ TeV*, Eur. Phys. J. C **79** (2019) 639, arXiv: 1902.04655 [hep-ex] (cit. on pp. 7, 21).

[82] ATLAS Collaboration, *Electron and photon performance measurements with the ATLAS detector using the 2015–2017 LHC proton–proton collision data*, JINST **14** (2019) P12006, arXiv: 1908.00005 [hep-ex] (cit. on pp. 7, 8, 21).

[83] ATLAS Collaboration, *Muon reconstruction performance of the ATLAS detector in proton–proton collision data at $\sqrt{s} = 13$ TeV*, Eur. Phys. J. C **76** (2016) 292, arXiv: 1603.05598 [hep-ex] (cit. on pp. 8, 21).

[84] ATLAS Collaboration, *Muon reconstruction and identification efficiency in ATLAS using the full Run 2 pp collision data set at* $\sqrt{s}$ = 13 *TeV*, Eur. Phys. J. C **81** (2021) 578, arXiv: 2012.00578 [hep-ex] (cit. on pp. 8, 21).

[85] M. Cacciari, G. P. Salam and G. Soyez, *The anti-*k_t *jet clustering algorithm*, JHEP **04** (2008) 063, arXiv: 0802.1189 [hep-ph] (cit. on p. 8).

[86] M. Cacciari, G. P. Salam and G. Soyez, *FastJet user manual*, Eur. Phys. J. C **72** (2012) 1896, arXiv: 1111.6097 [hep-ph] (cit. on p. 8).

[87] ATLAS Collaboration, *Topological cell clustering in the ATLAS calorimeters and its performance in LHC Run 1*, Eur. Phys. J. C **77** (2017) 490, arXiv: 1603.02934 [hep-ex] (cit. on p. 8).

[88] ATLAS Collaboration, *Jet energy scale and resolution measured in proton–proton collisions at* $\sqrt{s}$ = 13 *TeV with the ATLAS detector*, Eur. Phys. J. C **81** (2020) 689, arXiv: 2007.02645 [hep-ex] (cit. on pp. 8, 21).

[89] ATLAS Collaboration, *Performance of pile-up mitigation techniques for jets in pp collisions at* $\sqrt{s}$ = 8 *TeV using the ATLAS detector*, Eur. Phys. J. C **76** (2016) 581, arXiv: 1510.03823 [hep-ex] (cit. on p. 8).

[90] ATLAS Collaboration, *ATLAS b-jet identification performance and efficiency measurement with* $t\bar{t}$ *events in pp collisions at* $\sqrt{s}$ = 13 *TeV*, Eur. Phys. J. C **79** (2019) 970, arXiv: 1907.05120 [hep-ex] (cit. on pp. 8, 9, 21).

[91] ATLAS Collaboration, *ATLAS flavour-tagging algorithms for the LHC Run 2 pp collision dataset*, (2022), arXiv: 2211.16345 [physics.data-an] (cit. on p. 8).

[92] ATLAS Collaboration, *Performance of missing transverse momentum reconstruction with the ATLAS detector using proton–proton collisions at* $\sqrt{s}$ = 13 *TeV*, Eur. Phys. J. C **78** (2018) 903, arXiv: 1802.08168 [hep-ex] (cit. on p. 8).

[93] M. Cacciari, G. P. Salam and G. Soyez, *The catchment area of jets*, JHEP **04** (2008) 005, arXiv: 0802.1188 [hep-ph] (cit. on p. 9).

[94] F. Chollet et al., *Keras*, 2015, URL: https://keras.io (cit. on p. 9).

[95] M. Abadi et al., *TensorFlow: Large-Scale Machine Learning on Heterogeneous Systems*, 2015, URL: https://www.tensorflow.org/ (cit. on p. 9).

[96] M. Stone, *Cross-Validatory Choice and Assessment of Statistical Predictions*, Journal of the Royal Statistical Society: Series B (Methodological) **36** (1974) 111 (cit. on p. 9).

[97] Particle Data Group, *Review of Particle Physics*, PTEP **8** (2020) 083C01 (cit. on p. 9).

[98] A. Shmakov et al., *SPANet: Generalized permutationless set assignment for particle physics using symmetry preserving attention*, SciPost Phys. **12** (2022) 178, URL: https://arxiv.org/abs/2106.03898 (cit. on p. 13).

[99] ATLAS Collaboration, *Measurement of b-tagging efficiency of c-jets in* $t\bar{t}$ *events using a likelihood approach with the ATLAS detector*, ATLAS-CONF-2018-001, 2018, URL: https://cds.cern.ch/record/2306649 (cit. on p. 21).

[100] ATLAS Collaboration, *Calibration of light-flavour b-jet mistagging rates using ATLAS proton–proton collision data at* $\sqrt{s}$ = 13 *TeV*, ATLAS-CONF-2018-006, 2018, URL: https://cds.cern.ch/record/2314418 (cit. on p. 21).

[101] ATLAS Collaboration,
E_T^{miss} performance in the ATLAS detector using 2015–2016 LHC pp collisions,
ATLAS-CONF-2018-023, 2018, URL: https://cds.cern.ch/record/2625233 (cit. on p. 21).

[102] J. Butterworth et al., *PDF4LHC recommendations for LHC Run II*, J. Phys. G **43** (2016) 023001, arXiv: 1510.03865 [hep-ph] (cit. on p. 22).

[103] ATLAS Collaboration, *Measurements of the production cross section of a Z boson in association with jets in pp collisions at $\sqrt{s}$ = 13 TeV with the ATLAS detector*, Eur. Phys. J. C **77** (2017) 361, arXiv: 1702.05725 [hep-ex] (cit. on p. 23).

[104] G. Cowan, K. Cranmer, E. Gross and O. Vitells,
Asymptotic formulae for likelihood-based tests of new physics, Eur. Phys. J. C **71** (2011) 1554, arXiv: 1007.1727 [physics.data-an] (cit. on p. 23), Erratum: Eur. Phys. J. C **73** (2013) 2501.

[105] D. L. Phillips,
A Technique for the Numerical Solution of Certain Integral Equations of the First Kind,
J. ACM **9** (1962) 84 (cit. on p. 29).

[106] A. N. Tikhonov, *On the solution of improperly posed problems and the method of regularization*, Sov. Math. **5** (1963) 1035 (cit. on p. 29).

[107] R. A. Willoughby, *Solutions of Ill-Posed Problems (A. N. Tikhonov and V. Y. Arsenin)*, SIAM Review **21** (1979) 266 (cit. on p. 29).

[108] G. Cowan, *Statistical data analysis*, 1998, ISBN: 978-0-19-850156-5 (cit. on p. 29).

[109] I. Brivio et al., *O new physics, where art thou? A global search in the top sector*, JHEP **02** (2020) 131, arXiv: 1910.03606 [hep-ph] (cit. on p. 40).

[110] D. Barducci et al.,
Interpreting top-quark LHC measurements in the standard-model effective field theory,
(2018), ed. by J. A. Aguilar-Saavedra et al., arXiv: 1802.07237 [hep-ph] (cit. on p. 43).

[111] J. Brehmer, K. Cranmer, F. Kling and T. Plehn,
Better Higgs boson measurements through information geometry, Phys. Rev. D **95** (2017) 073002, arXiv: 1612.05261 [hep-ph] (cit. on p. 45).

[112] N. Castro, J. Erdmann, C. Grunwald, K. Kröninger and N.-A. Rosien,
EFTfitter—A tool for interpreting measurements in the context of effective field theories,
Eur. Phys. J. C **76** (2016) 432, arXiv: 1605.05585 [hep-ex] (cit. on p. 45).

[113] O. Schulz et al., *BAT.jl: A Julia-Based Tool for Bayesian Inference*,
SN Computer Science **2** (2021) 210, ISSN: 2661-8907,
URL: https://doi.org/10.1007/s42979-021-00626-4 (cit. on p. 45).

[114] O. Bessidskaia Bylund, F. Maltoni, I. Tsinikos, E. Vryonidou and C. Zhang,
Probing top quark neutral couplings in the Standard Model Effective Field Theory at NLO in QCD,
JHEP **05** (2016) 052, arXiv: 1601.08193 [hep-ph] (cit. on p. 45).

[115] S. Frixione, V. Hirschi, D. Pagani, H. .-S. Shao and M. Zaro,
Electroweak and QCD corrections to top-pair hadroproduction in association with heavy bosons,
JHEP **06** (2015) 184, arXiv: 1504.03446 [hep-ph] (cit. on p. 51).

[116] CMS Collaboration, *Search for new physics in top quark production with additional leptons in the context of effective field theory using 138 fb^{-1} of proton-proton collisions at $\sqrt{s}$ = 13 TeV*, 2023,
URL: https://cds.cern.ch/record/2851651 (cit. on p. 51).